## ATOMIC STRUCTURE AND NON-ELECTRONIC PROPERTIES OF SEMICONDUCTORS

# Distribution of hydrogen in silicon and silicon carbide following high-temperature proton irradiation

V. V. Kozlovskiĭ*)

*St. Petersburg State Technical University, 195251 St. Petersburg, Russia*

V. A. Kozlov

*A. F. Ioffe Physicotechnical Institute, Russian Academy of Sciences, 194021 St. Petersburg, Russia*
(Submitted June 10, 1999; accepted for publication June 11, 1999)
Fiz. Tekh. Poluprovodn. **33**, 1409–1410 (December 1999)

The distribution of hydrogen in Si and SiC following high-temperature proton irradiation ($T_{irr}=20-700\,^{\circ}C$) is studied by secondary-ion mass spectrometry. It is shown that the hydrogen concentration profile in SiC depends weakly on irradiation temperature. In Si appreciable alteration of the concentration profile is observed already at $T_{irr}\simeq 300\,^{\circ}C$, and the profile completely loses its concentration gradient at $T_{irr}\simeq 700\,^{\circ}C$. © *1999 American Institute of Physics.* [S1063-7826(99)00112-X]

The methods for the radiation-induced modification of semiconductor materials using proton beams have undergone extensive development in the last decade.[1–4] Semiconductors are irradiated over a broad temperature range in such methods as proton-stimulated diffusion and doping with radiation defects,[1] precision separation of layers in semiconductor wafers (the smart-cut technology),[2] transmutation doping,[3] and ion-beam mixing.[4] One very important factor in these material modification methods is the variation of the depth profile of hydrogen in the semiconductor as a function of irradiation temperature. Special investigations of this problem have not been carried out until now.

This paper describes a study of the hydrogen concentration depth profiles in the basic material and one of the most promising materials in modern semiconductor electronics, viz., silicon and silicon carbide, following irradiation (implantation) by $H^+$ ions in the broad temperature range from 20 to 700 °C. Samples of KDB-40 silicon and silicon carbide of the 6*H* polytype were irradiated in the accelerator of an NG-200U neutron generator. The proton energy was 100 keV, the beam current density was 5 $\mu$A/cm$^2$, the irradiation time was 1200 s, and the implanted dose was $4\times10^{16}$ cm$^{-2}$. The irradiation was carried out in special devices, which permitted establishment and monitoring of the target temperature during irradiation to within $\pm 5\,^{\circ}C$. The hydrogen concentration depth profiles were measured using secondary-ion mass spectrometry (SIMS).

Figure 1 shows some of the results obtained by us. As is seen from the figure, the position of the maximum on the hydrogen concentration depth profile in the irradiated crystals is virtually independent of the irradiation temperature and is located at a depth $x\simeq 0.9$ $\mu$m in Si and $x\simeq 0.65$ $\mu$m in SiC for 100-keV protons. The position of the maxima is determined by the projected free path of the hydrogen ions in the semiconductor and is in good agreement with the proton deceleration losses stipulated by the charge and mass of silicon and carbon, as well as by the density of the semiconductor.[5] It is noteworthy that variation of the irradia-

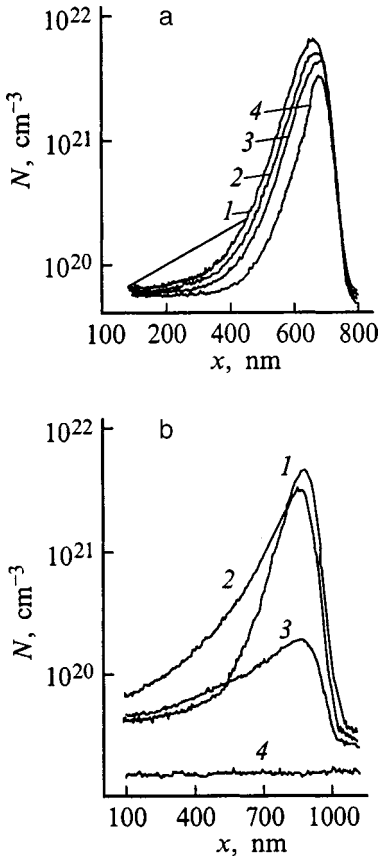


FIG. 1. Distribution of the concentration ($N$) in SiC (a) and Si (b) following irradiation with 100-keV protons to a dose of $4\times10^{16}$ cm$^{-2}$ at various irradiation temperatures $T_{irr}$, °C: *1* — 20, *2* — 300, *3* — 500, *4* — 700.

 

tion temperature $T_{irr}$ in the range from 20 to 700 °C has virtually no effect on the form of the hydrogen concentration depth profiles in SiC (Fig. 1a), which maintain a ''sharp'' maximum even in the case of proton implantation at $T_{irr} = 700$ °C. In contrast with SiC, the irradiation of Si leads to appreciable alteration of the hydrogen concentration depth profile already at $T = 300$ °C (Fig. 1b), and collapse and broadening of the maximum on the hydrogen concentration depth profile toward the irradiated surface are observed. These changes intensify with increasing irradiation temperature, and the hydrogen concentration depth profile completely loses its gradient at $T_{irr} = 700$ °C (Fig. 1b, curve *4*).

Assuming that the redistribution of hydrogen during high-temperature implantation is caused by a diffusion process and is described by Fick's law, we estimated the diffusion coefficient $D$ of hydrogen using the solution of the Fick equation for a semi-infinite body with an impermeable boundary.[6] A comparison of the calculated and experimental data showed that the value of $D$ in Si under the conditions of high-temperature proton irradiation is several times smaller than the values obtained by studying ordinary thermal diffusion.[7] For example, the value of $D$ in our case for $T_{irr} = 300$ °C was only $D = 5 \times 10^{-12}$ cm$^2$/s, while in the case of pure thermal diffusion $D > 10^{-11}$ cm$^2$/s. Such a difference in the values of the diffusion coefficient of H in Si is probably due to the sensitivity of the migration of hydrogen to the presence of defects in the crystal structure of the semiconductor caused by the radiation damage appearing as a result of proton implantation.

In conclusion, we should note the considerable practical interest in the results which we have obtained. Our studies demonstrate that the buried layers saturated with hydrogen in Si and SiC crystals can be formed at elevated irradiation temperatures. These temperatures can be as high as $T_{irr} \simeq 300$ °C for silicon, while they can exceed 700 °C for silicon carbide. The use of such high-temperature proton-implantation regimes is promising for the fabrication of silicon-on-insulator and silicon-carbide-on-insulator structures using the smart-cut technology. Since raising the irradiation temperature sharply reduces the number of radiation defects introduced into the semiconductor during proton irradiation,[8] the use of high-temperature proton implantation can sharply lower the defect density in the active layers in semiconductor-on-insulator structures, allowing moderation of the conditions for the postimplantation annealing of the radiation defects in such structures, and improving their quality. These merits of high-temperature proton implantation should be displayed especially clearly in the case of silicon carbide, in which the postimplantation annealing of the radiation defects following proton irradiation is one of the key problems in creating silicon-carbide-on-insulator structures suitable for device applications.

We wish to thank R. Sh. Malkovich for assistance in solving the diffusion problems and Yu. A. Kudryavtsev for performing the SIMS measurements of the hydrogen concentration depth profiles.

This work was carried out with partial support from the ''Promising Technologies and Micro- and Nanoelectronics Devices'' Program of the Ministry of Science and Technology of the Russian Federation (Grant 02.04.330.89.1.2).

*)E-mail: kozlovski@tuexph.stu.neva.ru

[1] I. V. Vasil'eva, G. A. Efremov, V. V. Kozlovskiĭ, V. N. Lomasov, and V. S. Ivanov, *Radiation Processes in the Technology of Materials and Structures for Electronics* [in Russian], Énergoatomizdat, Moscow, 1997.
[2] M. Bruel, Electron. Lett. **31**, 1201 (1995).
[3] L. F. Zakharenkov, V. V. Kozlovskiĭ, and B. A. Shustrov, Fiz. Tekh. Poluprovodn. **26**, 3 (1992) [Sov. Phys. Semicond. **26**, 1 (1992)].
[4] *Surface Modification and Alloying by Laser, Ion, and Electron Beams*, edited by J. M. Poate, G. Foti, and D. C. Jacobson [Plenum Press, New York, 1983; Mashinostroenie, Moscow, 1987].
[5] *Interaction of Charged Particles with Solids and Surfaces*, edited by A. Gras-Martí, H. M. Urbassek, N. R. Arista, and F. Flores [Plenum Press, New York, 1991; Vysshaya Shkola, Moscow, 1994].
[6] E. D. Gornushkina, V. A. Didik, V. V. Kozlovskiĭ, and R. Sh. Malkovich, Fiz. Tekh. Poluprovodn. **25**, 2044 (1991) [Sov. Phys. Semicond. **25**, 1232 (1991)].
[7] S. J. Pearton, J. W. Corbett, and M. Stavola, *Hydrogen in Crystalline Semiconductors* (Springer-Verlag, Heidelberg, 1992), p. 225.
[8] V. S. Vavilov, B. M. Gorin, N. S. Danilin, A. E. Kiv, Yu. L. Nurov, and V. I. Shakhovtsov, *Radiation Methods in Solid-State Electronics* [in Russian], Nauka, Moscow, 1990.

Translated by P. Shelnitz

## ELECTRONIC AND OPTICAL PROPERTIES OF SEMICONDUCTORS

# Electronic properties of $ZnGeP_2$ crystals obtained by a solid-phase reaction

A. A. Vaĭpolin, Yu. V. Rud', and T. N. Ushakova

*A. F. Ioffe Physicotechnical Institute, Russian Academy of Sciences, 194021 St. Petersburg, Russia*

V. Yu. Rud'*)

*St. Petersburg State Technical University, 195251 St. Petersburg, Russia*
(Submitted April 12, 1999; accepted for publication April 20, 1999)
Fiz. Tekh. Poluprovodn. **33**, 1411–1415 (December 1999)

The low-temperature synthesis of $ZnGeP_2$ by a solid-phase reaction is carried out for the first time, and photosensitive heterostructures based on it are obtained. The spectral dependences of the photoluminescence of the crystals and the photoconversion quantum efficiency of the heterostructures are investigated. Conclusions regarding the prospects of the new technology for improving the optical quality of $ZnGeP_2$ are drawn. © *1999 American Institute of Physics.* [S1063-7826(99)00212-4]

Expansion of the list of diamond-like substances in accordance with the rules proposed by Goryunova for their formation[1,2] has led not only to the formation of a large arsenal of new semiconductors with fundamental parameters having a broad range of variation, but also to the disclosure of areas of application, where ternary and more complicated compounds no longer experience competition on the part of their simpler analogs (Ge, Si, III–V, etc.). One of the most important results of the investigations of multielement materials was the discovery of record-high values of the nonlinear polarizability in some ternary compounds with a chalcopyrite lattice, which immediately placed them among the elite nonlinear-optical materials.[3,4] There has recently been a surge of interest in such crystals, high laser-radiation frequency conversion efficiencies have been demonstrated experimentally, and a further search for methods to improve their optical quality has simultaneously been conducted.[5,6] This paper focuses on this area of research and reports the first results of experimental measurements of the electronic properties of crystals of one such material, viz., $ZnGeP_2$, and photosensitive structures based on it, which were obtained by a new synthesis method at temperatures significantly below the congruent melting point of the compound.

1. The new method for synthesizing $ZnGeP_2$ is based on the solid-phase reaction of germanium with a vapor phase of controlled composition. Germanium wafers with the (111) crystallographic orientation served as the starting material for synthesizing the ternary phosphide. The reaction takes place as a result of the thermal treatment of the germanium wafers in vapors of zinc and phosphorus in the stability region of the solid phases of Ge and $ZnGeP_2$. Either a continuous layer of the compound or individual faceted crystals are created on the surface of the Ge wafers by varying the parameters of the solid-phase reaction. Under illumination by white light, they differ in color from germanium and are similar to $ZnGeP_2$. The outer surface of such layers is generally rough, and individual crystallites measuring about 0.2 $\times$0.2 mm in the form of elongated prisms can be discerned on it. Both the layers and individual crystallites comprise a single entity with the substrate. When the wafer surface is illuminated after completion of the solid-phase reaction, the crystals formed reflect light as microfragments of a single crystal. This means that the spatially separated crystals formed during the solid-phase reaction of germanium with the vapor phase comprise a system that is oriented identically to the substrate.

2. X-ray diffractometric measurements reveal weak reflections from tiny crystals grown in a definite technological regime along with the strong reflections of the Ge substrate. The intensity of the reflections is determined to a considerable extent by the accommodation density of the crystallites and depends on the conditions under which the solid-phase reaction is carried out. Estimates of the Bragg angles and the orientation of the reflecting planes of the crystals grown on germanium provide some basis to claim that $ZnGeP_2$ forms in the processes that we carried out. The majority, if not all, of the $ZnGeP_2$ crystals are oriented so that their (112) crystallographic plane coincides with the substrate (111) plane, and the [111] direction in it coincides with one of the equivalent directions in the $\langle 112\rangle$Ge substrate: $[\bar{1}12]$, $[1\bar{2}2]$, or $[\bar{2}11]$.

It was also established as a result of the experiments performed that under certain conditions the solid-phase reaction also permits the synthesis of continuous layers of $ZnGeP_2$ with thicknesses up to 2 $\mu$m. According to the x-ray measurements, such layers have a polycrystalline structure.

3. Substrate/$ZnGeP_2$ heterojunction structures were created to study the photoelectric properties of the crystals and layers which we obtained. The substrates used were *p*-type germanium with a resistivity $\rho \approx 1\,\Omega\cdot$cm at $T = 300$ K. According to the data from thermopower measurements, the

 

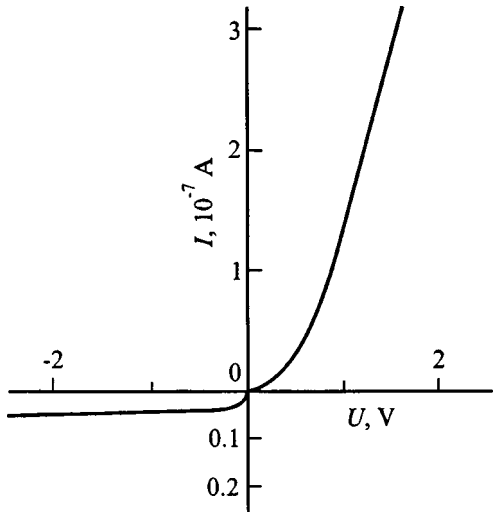


FIG. 1. Stationary current-voltage characteristic of a $ZnGeP_2$/Ge structure at $T=300$ K. The direction of current flow corresponds to negative polarity of the external bias on $ZnGeP_2$.

$ZnGeP_2$ layers exhibit hole conductivity, which is typical of bulk $ZnGeP_2$ crystals grown from a melt by the traditional method of directional solidification.[4,7]

The Ge/$ZnGeP_2$ heterostructures which we obtained display clear-cut rectification (Fig. 1). The direction for current flow in such structures corresponds to negative polarity of the external bias on $ZnGeP_2$, and the forward branch of their stationary current-voltage characteristics in the voltage range $U>0.7$ V obeys the relation

$$I=(U-U_0)/R_r, \tag{1}$$

where the cutoff voltages $U_0\approx 0.5-0.6$ V, and the residual resistance $R_r\approx(1-5)\times 10^7\,\Omega$ at $T=300$ K. Estimates of the resistivity on the basis of the values of $R_r$ obtained for such heterostructures, with consideration of the fact that the residual resistance is determined mainly by the resistance of the new phase that is formed, give $\rho\approx 10^8-10^9\,\Omega\cdot$cm for different samples. According to the value of $\rho$, the compound synthesized also corresponds to the known data for bulk $ZnGeP_2$ crystals grown by the traditional method from a melt. It is also noteworthy that at reverse biases $U\lesssim 2$ V the reverse currents in the heterostructures do not exceed $5\times 10^{-9}$ A at $T=300$ K.

When the $ZnGeP_2$/Ge heterostructures are illuminated from the $ZnGeP_2$ side, they usually exhibit a broad-band photovoltaic effect. The $ZnGeP_2$ layer is then negatively charged, in accordance with the rectification direction in such heterostructures. Photosensitivity dominates when the heterostructures are illuminated from the side of their broad-band component, and it reaches 200 V/W at $T=300$ K in the best of the heterostructures.

Figure 2 presents typical plots of the spectral dependence of the relative photoconversion quantum efficiency $\eta$ for heterostructures consisting of an individual $ZnGeP_2$ crystallite on Ge (curve *1*) and a layer of $ZnGeP_2$ on Ge in comparison with the spectrum of $\eta$ for an In/$ZnGeP_2$ structure fabricated on the basis of a $ZnGeP_2$ single crystal grown from a melt of stoichiometric composition, which has already found application in the creation of nonlinear-optical converters of laser radiation.[9] It is seen that the spectral dependences of $\eta$ for the structures compared are close to one another in the spectral region corresponding to the fundamental absorption of $ZnGeP_2$. This provides additional evidence that the use of the solid-phase reaction permits synthesis as a result of the interaction of one of the components of the ternary phosphide (Ge) with the other two components supplied from the vapor phase. It also follows from the spectra of $\eta$ (Fig. 2) that the heterostructures obtained can be employed as broad-band photodetectors in the range from 2.5 to 3.3 eV, which, in addition, are essentially ''blind'' to radiation at photon energies $\hbar\omega<2.2$ eV.

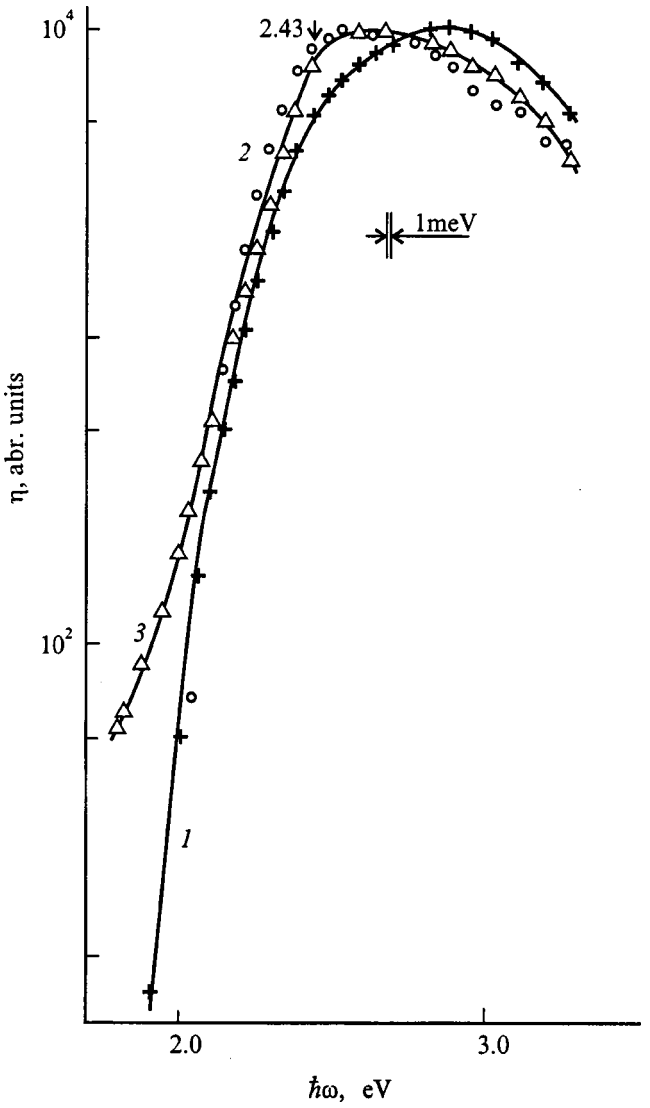


FIG. 2. Spectral dependence of the relative photoconversion quantum efficiency of $ZnGeP_2$/Ge structures (*1* — sample 1–1, *2* — sample 2–1) and In/$ZnGeP_2$ structures (*3* — sample supplied by Lockheed Sanders) at $T=300$ K.

It also follows from Fig. 2 that the drop in $\eta$ at $\hbar\omega<2.2$ eV is sharper for the heterostructures obtained by the solid-phase reaction than for the structures based on $ZnGeP_2$ single crystals grown from a melt. With consideration of Refs. 10–12, this drop in $\eta$ may be evidence that the signifi-

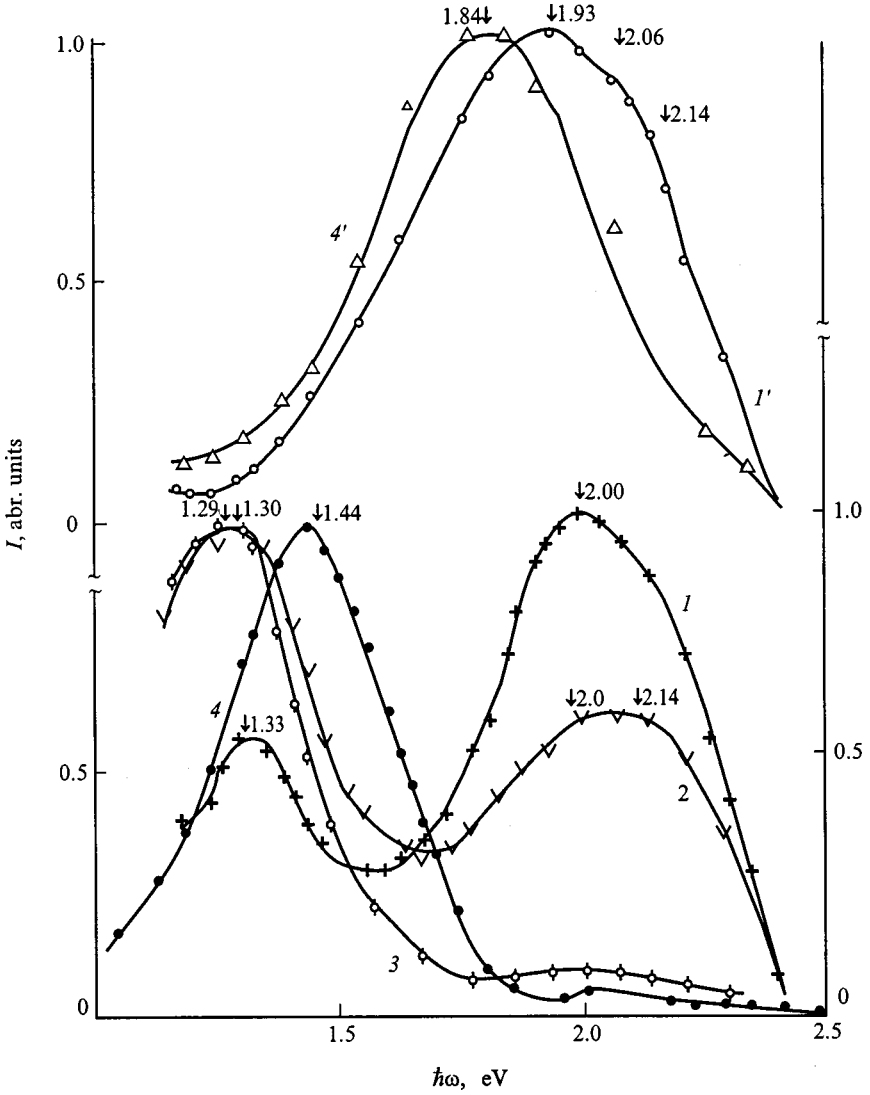


FIG. 3. Spectral dependence of the intensity of the stationary photoluminescence of $ZnGeP_2$ crystals grown by the solid-phase reaction (*1–3* and *1′*) and by directional solidification of a melt of stoichiometric composition (*4* and *4′*) (*1* and *1′* — sample 1–1, *2* — sample 1–3, *3* — sample 1–4, *4* and *4′* — sample supplied by Lockheed Sanders, $\hbar\omega_{exc}=3.7$ eV. *T*, K: *1–4* — 77, *1′* and *4′* — 300. The spectral resolution is no poorer than 1 meV).

cant lowering of the synthesis temperature of $ZnGeP_2$ is accompanied by a drop in the concentration of the lattice defects responsible for photosensitivity in the near-edge spectral region at $\hbar\omega<2.2$ eV.

4. The spectral dependence of the stationary photoluminescence (PL) was also investigated in the $ZnGeP_2$ samples synthesized for the first time by a solid-phase reaction. The recombination luminescence was excited by the output of an argon laser ($\lambda_{exc}=448$ nm), which is strongly absorbed in $ZnGeP_2$, at $T=77$ and 300 K. The spectral resolution was no poorer than 1 meV. Typical plots of the spectral dependence of the PL for $ZnGeP_2$ crystals obtained by the solid-phase reaction and grown from a melt are presented in Fig. 3. The principal results of these investigations are described below.

The plots of the spectral dependence of the PL of all the $ZnGeP_2$ samples obtained by the solid-phase reaction are similar to one another (Fig. 3, curves *1–3*) and usually consist of two broad bands at 77 K: a long-wavelength band with a maximum at $\hbar\omega_1$ and a short-wavelength band at $\hbar\omega_2$. The energetic position of $\hbar\omega_1$ for the reaction conditions employed ranges from 1.29 to 1.33 eV, while the value of $\hbar\omega_2$ for all the samples essentially coincides and is roughly equal to 2.0 eV. The widths of the PL bands at half-maximum are fairly high: $\delta_1\approx0.30-0.35$ eV and $\delta_2\approx0.47$ eV. This finding indicates that they are not elementary bands.

Scanning a $ZnGeP_2$ surface by a focused PL-exciting probe (with a diameter of about 0.2 mm) revealed that the PL spectra are faithfully reproduced from point to point along the surface of the microcrystalline layers. This finding points out the high uniformity of the layers with respect to their luminescence properties. In the case of the samples in which a system of tiny, spatially separated $ZnGeP_2$ crystals is dispersed in a thin, finely crystalline layer, the PL intensity of this layer in the vicinity of $\hbar\omega_2$ is $1-1.5$ orders of magnitude smaller than the PL intensity of single crystals. Figure 3 (curve *1–3*) shows examples of the variation achieved in the ratio between the intensities of the short- and long-wavelength PL components. The brightest short-wavelength PL was obtained specifically when single-crystal formations were excited (Fig. 3, curve *1*). The PL spectrum of $ZnGeP_2$ single crystals grown from a melt of stoichiometric composition (Fig. 3, curve *4*) also includes two components.[11,13] However, in this case the long-wavelength band is blue-shifted relative to the band for the material obtained by the solid-phase reaction, while the short-wavelength component

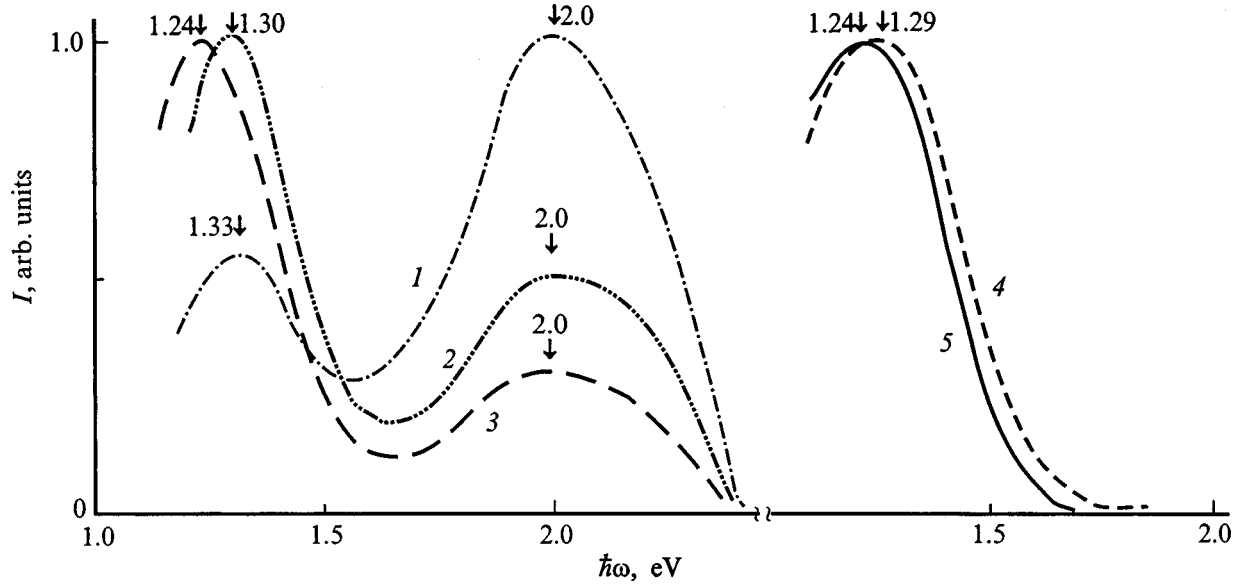


FIG. 4. Spectral dependence of the intensity of the stationary PL of $ZnGeP_2$ crystals on pump power at 77 K ($\hbar\omega_{exc}=3.7$ eV. *1–3* — sample 1–1, *4* and *5* — sample 1–5. $P/P_0$: *1* and *4* — 1, *2* — 0.7, *3* and *5* — 0.1.

at $\hbar\omega_2$ is significantly weaker. For this reason, the photoluminescence of the material obtained by the solid-phase reaction is visually displayed in the form of a bright orange luminescence band, while the luminescence intensity of the crystals obtained from a melt at the same excitation level is so weak that it is not manifested visually.

As the temperature is raised to 300 K, the short-wavelength component becomes dominant in the PL spectra of the samples compared (Fig. 3, curves *1′* and *4′*) due to the faster quenching of the long-wavelength band with temperature. In both types of samples the PL bands at $T=300$ K are broadened relative to the bands at 77 K, and their width reaches $\delta_2\approx 0.54$ eV in the crystals obtained by low-temperature synthesis and $\delta_2\approx 0.64$ eV in the crystals grown from a melt. These data once again reflect the nonelementary character of the short-wavelength PL component. The features indicated in Fig. 3 (curve *1′*) coincide with the values of the energies of the pseudodirect interband transitions of electrons from the lower conduction band to subbands of the valence band split by the anisotropic crystal field and spin-orbit coupling.[8] This is the primary manifestation of the nonelementary character of the short-wavelength PL band at $T=300$ K. It is significant that in the case of the crystals grown from a melt (Fig. 3, curve *4′*) the maximum at $\hbar\omega_2$ undergoes a red shift amounting to $\approx$10 meV, which may indicate the decisive role of centers with shallow levels in the photoluminescence of such crystals, as is confirmed in the spectra of $\eta$ (Fig. 2, curve *3*).

The PL intensity at the temperatures investigated drops rapidly in the region of the direct transitions in the spectra (Fig. 3) of both the crystals obtained by the new method and the crystals grown by the traditional high-temperature method of directional solidification,[8,9] precluding the observation of luminescence in the region of direct interband transitions.

Figure 4 presents plots of the spectral dependence of the PL as a function of the pump power for a single crystal and a microcrystalline layer of $ZnGeP_2$ obtained by the solid-phase reaction. As the pump power $P$ is increased, the contribution of the short-wavelength PL component intensifies (Fig. 4, curve *1–3*), and the maximum of the long-wavelength band at $\hbar\omega_2$ undergoes a red shift. The pump power also has a similar influence on the long-wavelength PL band in samples where the latter is decisive (Fig. 4, curves *4* and *5*). In fact, in such samples the maximum at $\hbar\omega_1$ and the wing of the band itself undergo red shifts as $P$ is increased. These laws allow us to assign the long-wavelength PL component to donor-acceptor transitions, while the short-wavelength component can be assigned to quasi-interband photoluminescent transitions of electrons from the lower minimum of the conduction band to the split subbands of the valence band.[8]

Thus, the results presented from the first investigations of the electronic properties of crystals and structures obtained by a solid-phase reaction point out the improved perfection of the $ZnGeP_2$ crystals in comparison to the crystals which are still grown from a melt by the conventional method of directional solidification.[8,9]

*)E-mail: rudvas@uniys.hop.stu.neva.ru

[1] N. A. Goryunova, Izv. Akad. Nauk SSSR, Ser. Fiz. **21**, 120 (1957).
[2] F. P. Kesamanly and Yu. V. Rud', Fiz. Tekh. Poluprovodn. **27**, 1761 (1993) [Semiconductors **27**, 969 (1993)].
[3] N. A. Goryunova, S. M. Ryvkin, I. M. Fishman, G. P. Shpen'kov, and I. D. Yaroshetskiĭ, Fiz. Tekh. Poluprovodn. **2**, 1525 (1968) [Sov. Phys. Semicond. **2**, 1272 (1968)].
[4] V. D. Prochukhan and Yu. V. Rud', Fiz. Tekh. Poluprovodn. **12**, 209 (1978) [Sov. Phys. Semicond. **12**, 121 (1978)].
[5] M. C. Ohmer and R. Pandey, MRS Bull. **23**, 16 (1998).

[6] P. G. Shunemann, R. L. Schepler, and P. A. Budni, MRS Bull. **23**, 45 (1998).
[7] B. H. Bairamov, V. Yu. Rud', and Yu. V. Rud', MRS Bull. **23**, 41 (1998).
[8] Yu. V. Rud', Fiz. Tekh. Poluprovodn. **28**, 1105 (1994) [Semiconductors **28**, 633 (1994)].
[9] P. G. Schunemann and T. M. Pollak, MRS Bull. **23**, 23 (1998).
[10] V. Yu. Rud', Yu. V. Rud', M. C. Ohmer, and P. G. Schunemann, Mater. Res. Soc. Symp. Proc. **450**, 339 (1996).
[11] V. Yu. Rud', Yu. V. Rud', and P. G. Shunemann, Fiz. Tekh. Poluprovodn. **30**, 1412 (1996) [Semiconductors **30**, 743 (1996)].
[12] V. Yu. Rud', Yu. V. Rud', M. C. Ohmer, and P. G. Schunemann, Inst. Phys. Conf. Ser. **152**, 127 (1998).
[13] V. Yu. Rud' and Yu. V. Rud', Pis'ma Zh. Tekh. Fiz. **22**(3), 37 (1996) [Tech. Phys. Lett. **22**(2), 107 (1996)].

Translated by P. Shelnitz

# Behavior of manganese impurities in $Hg_3In_2Te_6$

O. G. Grushka, Z. M. Grushka, V. M. Frasunyak, and V. S. Gerasimenko

*Chernovtsy State University, 274012 Chernovtsy, Ukraine*

(Submitted March 10, 1999; accepted for publication April 26, 1999)
Fiz. Tekh. Poluprovodn. **33**, 1416–1419 (December 1999)

The behavior of manganese impurities in $Hg_3In_2Te_6$ is investigated. The carrier concentration remains considerably smaller than the impurity concentration in the doped crystals. The introduction of manganese into $Hg_3In_2Te_6$ does not alter the position of the Fermi level, which is located near the middle of the band gap of the material. The electrical conductivity remains intrinsic down to 150 K. It is shown that manganese exists in the $Mn^{2+}(3d^5)$ charge state in the $Hg_3In_2Te_6$ lattice and does not lead to the appearance of new chemical bonds in the host, but does influence the short-range structure. When $N_{Mn}<9.2\times10^{19}\,cm^{-3}$, $Hg_3In_2Te_6$ has higher values of the carrier mobility than does the undoped material. © *1999 American Institute of Physics.* [S1063-7826(99)00312-9]

The interest in the study of $Hg_3In_2Te_6$ is due to its properties, which are advantageous for practical use: its good photoelectric characteristics, the heightened stability of its parameters toward the effects of ionizing radiation, the electrical inactivity of impurities added to it, etc.[1] The unusual properties of $Hg_3In_2Te_6$ are associated with the presence of a large number ($\sim2.7\times10^{21}\,cm^{-3}$) of vacant cation sites, or so-called stoichiometric vacancies, in its sphalerite structure. The presence of stoichiometric vacancies in semiconductors classified as defect-containing structures of the $In_2Te_3$ type is due to the satisfaction of crystal-chemical conditions which result in the number of cations in the stoichiometric composition being less than the number of anions. The specific features of the crystal structure which distinguish semiconductors with stoichiometric vacancies from II–VI, III–V, and IV–VI compounds include not only their radiation stability, but also the considerable solubility of the impurities and their intrinsic conductivity over a broad temperature range. Various models have been used to account for the absence of impurity conduction in doped $In_2Te_3$. Koshkin *et al.*[2] proposed a thermodynamic model of the dissolution of impurities, according to which the impurity atoms are localized in stoichiometric vacancies in the unionized state and therefore do not make a contribution to the electrical conductivity. The opponents of this model[3,4] claim that the impurities introduced into the crystal dissolve in stoichiometric vacancies and that they do not exist in the neutral state, but exhibit their own characteristic valence. The electrical inactivity of metal impurities is then attributed to stabilization of the Fermi level resulting from the fact that the impurity shifts trivalent indium (in $In_2Te_3$) into another stable state. However, the intrinsic character of the conductivity in $In_2Te_3$ does not rule out the possibility for the existence of local levels in the band gap. As was shown in Ref. 5, band-gap states entirely determine the photoelectric properties of doped $In_2Te_3$.

In the present paper we report the results of an ongoing investigation of the state and behavior of impurities in a semiconductor with stoichiometric vacancies that differs from $In_2Te_3$ in that some of the indium atoms are replaced by mercury atoms, viz., the compound $Hg_3In_2Te_6$, in which the structure of the energy bands is direct and the gap width $E_g$ at $T=300$ K is 0.74 eV. The purpose of this work is to obtain results which would supplement the available information and help to elucidate the features of the properties of impurity centers in $Hg_3In_2Te_3$.

Manganese was selected as the impurity, since its presence in a crystal can be detected by studying the impurity magnetism. Crystals of $Hg_3In_2Te_6$, which were doped with manganese during growth by the Bridgman–Stockbarger method, were used in the experiments. The concentration $N_{Mn}$ of the impurity introduced into the mixture varied in the range $5\times10^{18}-10^{21}\,cm^{-3}$. X-ray powder diffraction analysis showed that all the bars grown were homogeneous. The series of distinct diffraction lines on the x-ray diffraction patterns correspond to a sphalerite structure with a lattice parameter for $N_{Mn}<10^{19}\,cm^{-3}$ equal to $a=6.289\pm0.001$ Å, which scarcely differs from the corresponding parameter for undoped samples. However, when the amount of manganese introduced was increased, the lattice parameter increased to $a=6.294\pm0.001$ Å at $N_{Mn}=5\times10^{20}\,cm^{-3}$.

The experimental data on the magnetic susceptibility (Fig. 1) provide evidence that the temperature dependence of the paramagnetic contribution of the manganese impurity to the magnetic susceptibility is described by the Curie law[6]

$$\chi_{Mn}=N_{Mn}\mu_B^2 g^2 S(S+1)(3kT)^{-1}, \tag{1}$$

where $\mu_B$ is the Bohr magneton, $S$ is the spin, and $g$ is the Landé factor. The observed course of the function $\chi_{Mn}^{-1}=f(T)$ indicates that exchange interactions between the magnetic impurities in $Hg_3In_2Te_6$ are not manifested within the range of values of $N_{Mn}$ investigated. The mean concentration of manganese ions determined using formula (1) with $S=5/2$ and $g=2$ for samples from different parts of a bar coincides satisfactorily with the concentration of manganese introduced into the mixture. Therefore, the manganese in the $Hg_3In_2Te_6$ lattice exists in the $Mn^{2+}$ $(3d^5)$ charge state and

 

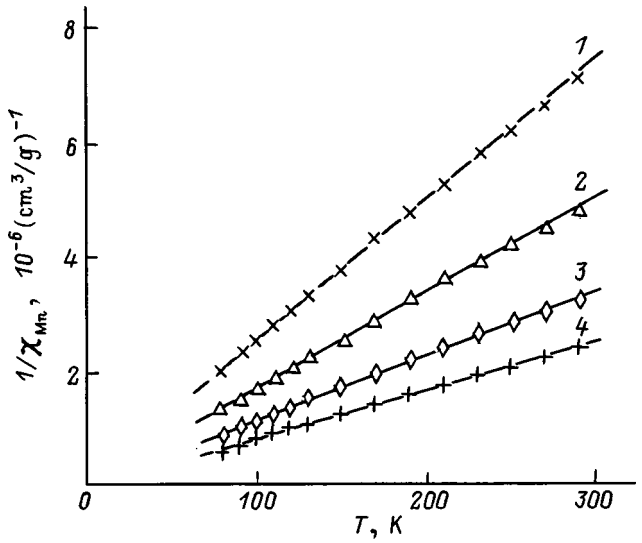


FIG. 1. Temperature dependence of the impurity magnetic susceptibility $\chi_{Mn}$ for various values of $N_{Mn}$, $10^{19}$ cm$^{-3}$: *1* — 4.1, *2* —6.2, *3* — 9.2, *4* — 12.

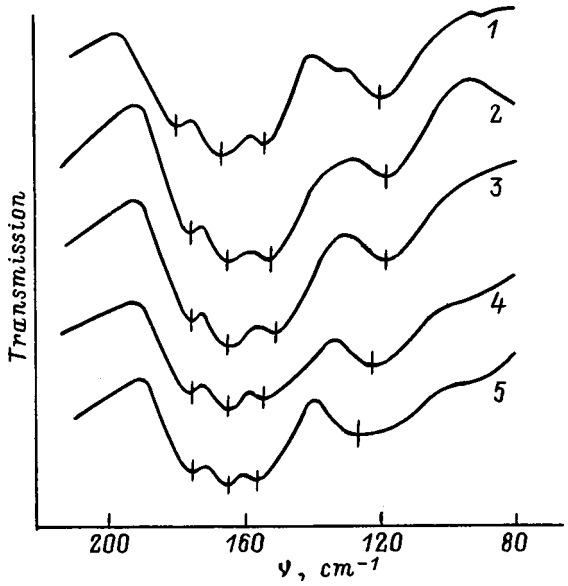


FIG. 3. Far-infrared transmission spectra of undoped (*1*) and manganese-doped $Hg_3In_2Te_6$ with various values of $N_{Mn}$, $10^{19}$ cm$^{-3}$: *2* — 1, *3* — 5.7, *4* — 12, *5* — 50. The maxima of the absorption bands in the vibrational spectra are marked (see Table I).

is thus an isovalent impurity. This can occur in the case of replacement of the highly volatile component Hg by Mn in the host lattice.

Figure 2 presents the distribution of the manganese concentration along bars with various values of the initial impurity concentration in the melt $N^0_{Mn}$. The concentration profiles obtained can be described by the following equation[6] with the effective distribution coefficient $k_{eff}=1.4$:

$$N_{Mn}=k_{eff}N^0_{Mn}(1-f)^{k_{eff}-1}, \tag{2}$$

where $f$ is the fraction of the melt crystallized. A value of the effective distribution coefficient $k_{eff}>1$ means that the impurity does not experience any ''resistance'' on the part of the host during crystallization and is drawn from the melt into the solid phase. In this case the form of the concentration profiles (Fig. 2) is determined by the chemical interaction between the host and impurity atoms.

The influence of the impurity on the short-range structure was investigated by far-infrared spectroscopy. The infrared (IR) transmission spectra obtained at 300 K are shown in Fig. 3. Four IR absorption bands corresponding to vibrational modes of interatomic bonds are observed in the frequency range investigated. Doping does not lead to the establishment of chemical bonds in addition to those already present. However, as can be seen from Table I, the material ''senses'' the presence of manganese already at a doping level of $10^{19}$ cm$^{-3}$, as is evidenced by the transformation of the vibrational characteristics of the spectrum. The first and second high-frequency absorption bands at 176 and 164 cm$^{-1}$, which correspond to the shortest and strongest bonds, do not react to the specific impurity concentration and remain unchanged up to $N_{Mn}=5\times10^{20}$ cm$^{-3}$. The third and fourth bands, which are assigned to somewhat weaker bonds, at first shift from their original frequency values of 154 and 120 cm$^{-1}$ to lower energy values, and then at $N_{Mn}\gtrsim1.2\times10^{20}$ cm$^{-3}$ they undergo shifts to higher values of the bond energy. The latter are accompanied by broadening of the absorption bands. The direction of the frequency transformation of the absorption bands reveals that the initial slight weakening of the least strongest interatomic bonds gives way to strengthening as the impurity concentration rises. The observed systematic displacement of the band with the lowest frequency as a function of the doping level attests to alteration of the short-range structure in $Hg_3In_2Te_6\langle Mn\rangle$ crystals.

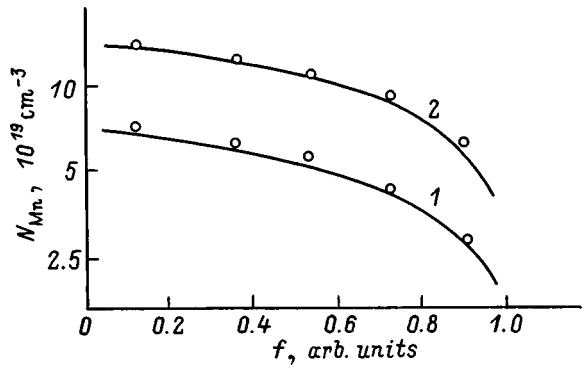


FIG. 2. Distribution of Mn impurity atoms along $Hg_3In_2Te_6$ bars (points) and calculated concentration profiles (solid lines) for $k_{eff}=1.4$ and two values of the initial concentration $N^0_{Mn}$, $10^{19}$, cm$^{-3}$: *1* — 5, *2* — 10.

TABLE I. Frequencies (in cm$^{-1}$) corresponding to the maxima of the absorption bands in the vibrational spectra of $Hg_3In_2Te_6$ as a function of the manganese doping level.

| $N_{Mn}$, cm$^{-3}$ | Band 1 | Band 2 | Band 3 | Band 4 |
|---|---|---|---|---|
| 0 | 180 | 166 | 154 | 120 |
| $10^{19}$ | 176 | 164 | 152 | 119 |
| $5.7\times10^{19}$ | 176 | 164 | 151 | 119 |
| $1.2\times10^{20}$ | 176 | 164 | 153 | 122 |
| $5\times10^{20}$ | 176 | 164 | 156 | 125 |

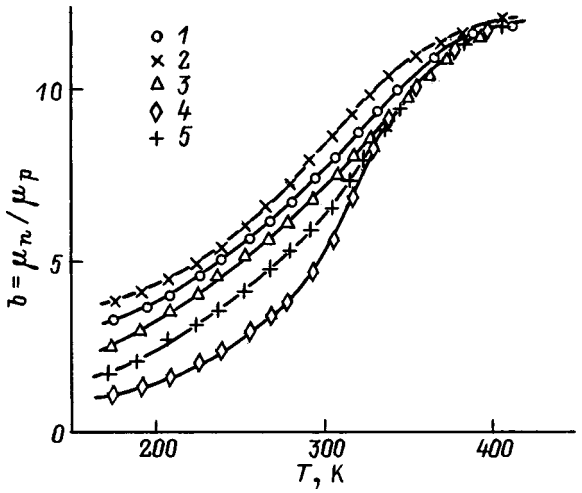


FIG. 4. Temperature dependence of the mobility ratio $b=\mu_n/\mu_p$ for undoped (*1*) and manganese-doped samples of $Hg_3In_2Te_6$ with various values of $N_{Mn}$, $10^{19}\,cm^{-3}$: *2* — 4.1, *3* — 6.2, *4* — 9.2, *5* — 12.

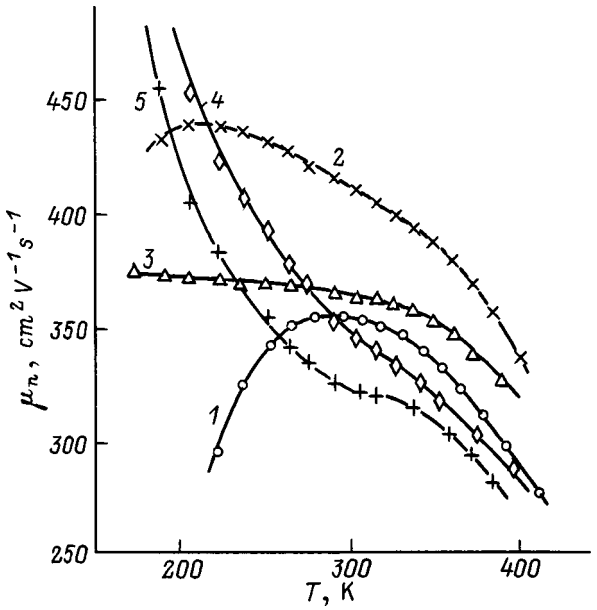


FIG. 5. Temperature dependence of the electron mobility $\mu_n$ for the same samples as in Fig. 4.

The investigations of the electrical properties showed that the presence of manganese in $Hg_3In_2Te_6$ crystals does not alter either the *n*-type conduction or the Hall concentration ($n_H \simeq 10^{13}\,cm^{-3}$ at 300 K), which remains 6–8 orders of magnitude below the concentration of the impurity introduced. As the temperature is lowered, the resistance of all the samples increases rapidly, making it difficult to perform low-temperature ($T<150$ K) measurements. Appreciable decreases in the slopes of the plots of the electrical conductivity $\log\sigma(T)$ and the Hall coefficient $\log R_H(T)$ were observed as the temperature was lowered for both undoped and doped samples. It would be tempting to attribute the low-temperature portions of the $\sigma(T)$ and $R_H(T)$ curves to impurity conduction. However, an analysis of the experimental plots of $\sigma(T)$, $R_H(T)$, and the thermoelectric power $\alpha(T)$ using the model of a semiconductor with mixed conduction showed that these kinetic coefficients can be described within the intrinsic conduction using the standard formulas[7]

$$n_i=(N_cN_v)^{1/2}\exp(-E_g/2kT), \tag{3}$$

$$\sigma=en_i\mu_n b^{-1}(1+b), \quad R_H=e^{-1}n_i^{-1}(1-b)(1+b)^{-1},$$

$$\alpha=(\alpha_p-\alpha_n b)(1+b)^{-1}, \tag{4}$$

where $n_i=n=p$ is the concentration of intrinsic charge carriers, $N_c$ and $N_v$ are the effective densities of state in the conduction and valence bands, $\alpha_n(\alpha_p)$ is the electron (hole) thermopower, and $b=\mu_n/\mu_p$ is the ratio between the electron and hole mobilities. In the relations (4) the Hall factor was assumed to be equal to unity, which is justified in our case, since the mechanism of scattering on neutral stoichiometric vacancies is significant due to the high concentration of stoichiometric vacancies. It was found that the mobility ratio $b=\mu_n/\mu_p$ depends on temperature for all the samples (Fig. 4). The temperature dependences of $\mu_n$ and $\mu_p$ (Figs. 5 and 6) obtained on the samples with different impurity concentrations showed that up to certain concentrations the impurity not only does not diminish the mobility of the carriers, but, instead, leads to its increase, especially at low temperatures. Only at large manganese concentrations ($N_{Mn}\gtrsim 9.2\times10^{19}\,cm^{-3}$) does the electron mobility decrease at high temperatures because of the increase in scattering on the lattice defects. The variety of temperature dependences of carrier mobility in $Hg_3In_2Te_6$ is specified by the values of the mobility ratio $b(T)$.

In fact, at low temperatures larger values of $\mu_n$ and $\mu_p$ correspond to smaller values of the Hall mobility $\mu_H$. The decrease in $b=\mu_n/\mu_p$ accounts for the low values of $\mu_H$ at low temperatures and its stronger temperature dependence,

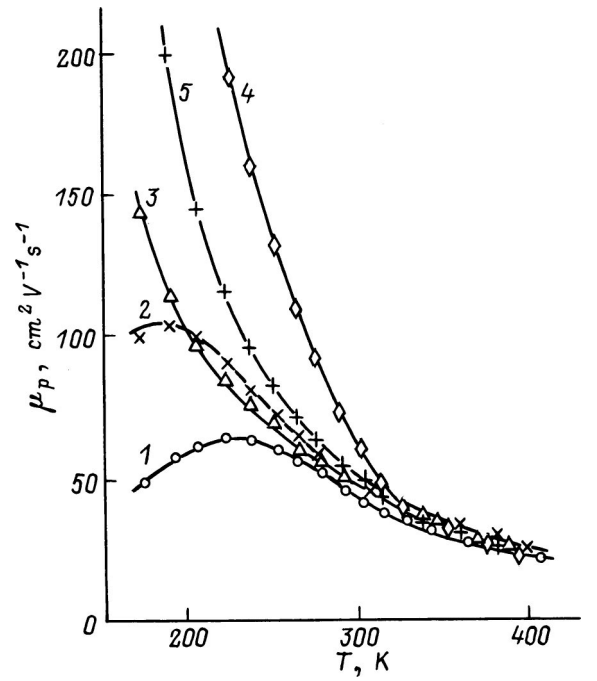


FIG. 6. Temperature dependence of the hole mobility $\mu_p$ for the same samples as in Fig. 4.

since $\mu_H = \mu_n - \mu_p$ in an intrinsic semiconductor. The general increase in carrier mobility is evidence that the material becomes more perfect when manganese is introduced up to certain concentrations. The Fermi level $F(T)$ was calculated using the relation[7] $F = -kT/\ln(n/N_c)$. The observed temperature-dependent behavior of the Fermi energy $F(T)$ is characterized by a dependence that is consistent with the formula $F = -E_g/2 + (kT/2)\ln(N_v/N_c)$, which is valid for an intrinsic semiconductor. Since $N_c < N_v$, the Fermi level is slightly above the middle of the band gap.

As follows from the data obtained, the kinetic coefficients of both the samples with the impurity and the samples without it behave in a manner characteristic of heavily compensated semiconductors. The special features observed are attributed to the nature of the material itself. The number of stoichiometric vacancies is so great that variation of the form of the principal bands of the crystal with the resultant appearance of density-of-states tails on these energy bands occurs with preservation of the band structure in the energy spectrum even in the absence of special doping. The presence of such tails, which are associated with a large number of stoichiometric vacancies, is indicated by the exponential spectral dependence of the absorption coefficient, which is specified by optical transitions involving the density-of-states tails in the Urbach region of the fundamental absorption edge.[8] Introduction of the impurity in amounts which are sure to be smaller than the number of intrinsic structural defects cannot significantly alter the spectrum of allowed states near the edges of the energy bands at $E < E_c$ and $E > E_v$ and lead to the appearance of impurity conduction. This feature is a manifestation of the screening of the impurity potential. The leading role in the screening can be played by the stoichiometric vacancies themselves, whose lone pairs can create an additional electric field.

The transmission spectra of undoped samples in the transparency region are characterized by structureless transmission ($T = 50-55\%$) in the wavelength range $\lambda = 2-25$ $\mu$m. Manganese doping does not alter the character of the $T(\lambda)$ curve, but it decreases the value of the transmission at $N_{Mn} \simeq 10^{20}\,\mathrm{cm}^{-3}$. The impurity light absorption observed beyond the edge of the fundamental band, which does not have any structure, is evidence that the scattering intensity does not depend on wavelength and is proportional to the impurity concentration.

Thus, the mechanism underlying the doping of $Hg_3In_2Te_6$, in which Mn atoms enter into the host lattice in the form of $Mn^{2+}$ ions by displacing mercury atoms into stoichiometric vacancies, is accompanied by a self-compensation effect. As the temperature is lowered, the conductivity displays an intrinsic character down to 150 K. The electrical inactivity of the manganese impurity ions is attributed to stabilization of the Fermi level near the middle of the band gap, rather than their chemical inactivity.

[1] G. G. Grushka, A. P. Bakhtinov, and Z. M. Grushka, J. Adv. Mater. **4**(1), 36 (1997).
[2] V. M. Koshkin, Yu. A. Freima, and L. V. Atroshchenko, Fiz. Tverd. Tela (Leningrad) **9**, 3120 (1967) [Sov. Phys. Solid State **9**, 2460 (1968)].
[3] I. A. Drabkin and B. Ya. Moĭzhes, Fiz. Tekh. Poluprovodn. **15**, 625 (1981) [Sov. Phys. Semicond. **15**, 357 (1981)].
[4] F. S. Nasredinov, V. P. Podkhalyuzin, P. P. Seregin, H. U. Tschirner, R. Rentsch, and T. Born, Fiz. Tekh. Poluprovodn. **20**, 1166 (1986) [Sov. Phys. Semicond. **20**, 737 (1986)].
[5] D. B. Anan'ina, V. L. Bakumenko, A. K. Bonakov, G. G. Grushka, and L. N. Kurbatov, Fiz. Tekh. Poluprovodn. **13**, 961 (1979) [Sov. Phys. Semicond. **13**, 561 (1979)].
[6] *Physics and Materials Science of Semiconductors with Deep Levels*, edited by V. I. Fistul' [in Russian], Metallurgiya, Moscow, 1987.
[7] E. V. Kuchis, *Galvanomagnetic Effects and Methods for Studying Them* [in Russian], Radio i Svyaz', Moscow, 1990.
[8] D. B. Anan'ina, V. L. Bakumenok, A. K. Bonakov, G. G. Grushka, and V. L. Kheĭfets, Izv. Akad. Nauk SSSR, Neorg. Mater. **16**, 1534 (1980).

Translated by P. Shelnitz

# Photoelectric properties of $Hg_{1-x}Cd_xTe$ single crystals grown from the vapor phase

S. S. Varshava and I. V. Kurilo

*''L'vov Polytechnic'' State University, 290013 L'vov, Ukraine*

I. S. Virt and D. I. Tsyutsyura

*Drogobych State Pedagogic Institute, 293720 Drogobych, Ukraine*

(Submitted April 5, 1999; accepted for publication April 26, 1999)
Fiz. Tekh. Poluprovodn. **33**, 1420–1422 (December 1999)

The electrical and photoelectric properties of $Hg_{0.1}Cd_{0.9}Te$ crystals grown by chemical vapor transport are investigated experimentally. The temperature dependences of the carrier concentration and mobility are determined. The photoelectric properties of these crystals fit a model based on the existence of fast and slow recombination centers. © *1999 American Institute of Physics.* [S1063-7826(99)00412-3]

The number of publications on the properties of $Hg_{1-x}Cd_xTe$ crystals with a large CdTe content ($x>0.5$) is fairly small. There have been reports on the technology for growing such crystals[1,2] and on the contact phenomena appearing at the boundary between a metal and the broad-band semiconductor $Hg_{1-x}Cd_xTe$ ($x>0.5$). The electrical and especially the photoelectric properties of crystals having the compositions indicated above have been studied extremely inadequately, principally because of the difficulty in obtaining homogeneous crystals with $x>0.5$ by the classical Bridgman or liquid-phase epitaxial methods.

In this paper we present the results of an investigation of the electrical and photoelectric properties of $Hg_{1-x}Cd_xTe$ ($x=0.9$) single crystals grown from the vapor phase. We have synthesized the compounds in advance from elemental Cd, Hg, and Te. We have then synthesized platelike single crystals measuring $10\times10\times10$ mm by chemical vapor transport in a closed $Hg_{1-x}Cd_xTe$–$NH_4Br$ system with temperatures in the source and crystallization zones equal to 953 and 833 K, respectively. Such crystallization regimes permit the synthesis of structurally perfect single crystals. The elemental composition of the solid solution was determined by a Comebax x-ray analyzer at 20 points along the sample. The CdTe content $x$ varied within 0.01, and no inclusions of other phases were found.

The Hall coefficient (in a magnetic field $H=1$ kOe) and the electrical conductivity were measured in the temperature range 300−77 K. The surface of each sample was chemically polished in a Br–$CH_3OH$ solution. Contacts were applied by sputter-depositing Au with patching by indium solder. The stationary photoelectric properties were investigated using an ISK-21 spectrometer with an F1 prism, and the nonstationary properties were studied using a pulsed $N_2$ laser (with a wavelength of 0.33 $\mu$m) and a pulsed GaAs-based light-emitting diode (with a wavelength of 0.9 $\mu$m).

The samples with the compositions indicated exhibited $p$-type conductivity over the entire range of temperatures $T$ investigated. The hole concentration was determined as $p(T)=1/eR(T)$, where $e$ is the charge of an electron, and

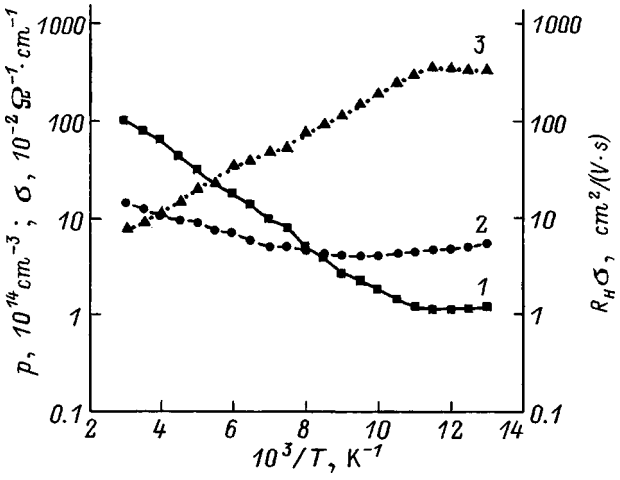


FIG. 1. Temperature dependence of the concentration $p$ (*1*), the electrical conductivity $\sigma$ (*2*), and the Hall mobility $R_H\sigma$ (*3*) for a sample of $2Hg_{0.1}Cd_{0.9}Te$.

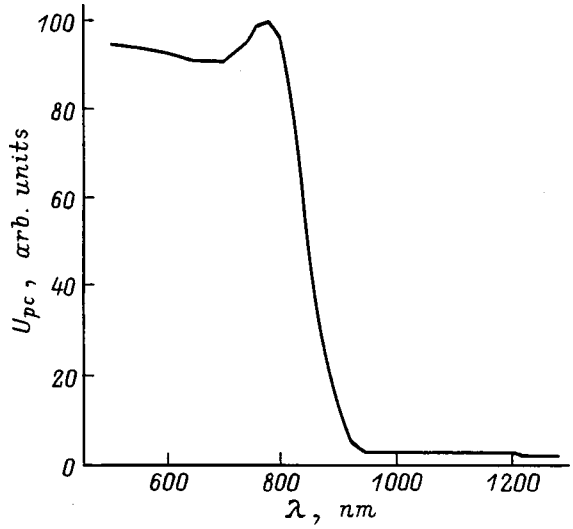


FIG. 2. Spectral dependence of the photoresponse $U_{pc}$ of a sample of $Hg_{0.1}Cd_{0.9}Te$ at 77 K.

 

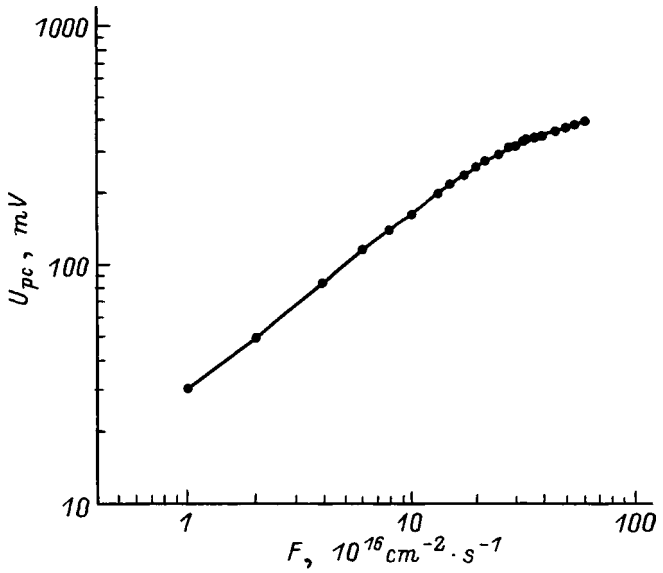


FIG. 3. Dependence of the photoresponse $U_{pc}$ at a wavelength of 0.9 $\mu$m on the excitation intensity $F$ for a sample of $Hg_{0.1}Cd_{0.9}Te$.

$R(T)$ is the Hall coefficient. The carrier mobility $\mu_p=\sigma R$ at $T=77$ K was 400 cm$^2$/(V·s), and the carrier concentration varied in the range $p=10^{16}-10^{14}$ cm$^{-3}$ from room temperature to liquid-nitrogen temperature. The growth of the $p$-type concentration with temperature (Fig. 1) is specified by a thermally activated process with an energy $E_{i1}=54$ meV in the temperature range 30−90 K, and the $p(T)$ curve reaches saturation at $T<90$ K. In this temperature range the carrier mobility varies according to a power law, $\mu\sim\mu_0 T^{-2}$, which points out the decisive role of the phonon scattering mechanism.

The spectral dependence of the photoresponse $U_{pc}(\lambda)$ at 77 K (Fig. 2) has a maximum at the wavelength $\lambda=780$ nm, and the gap width determined from half of the decline of the long-wavelength edge is $E_g=1.45$ eV. In the surface excitation region (at $\lambda d>1$) the photocurrent depends weakly on $\lambda$, and its substantial value (compared with the peak value) attests to the small density of surface states. The impurity photocurrent exists up to a wavelength of 1250 nm; i.e., the impurity level is located at a distance $E_{i2}=0.45$ eV from the edge of one of the allowed bands. The brightness-voltage characteristic for excitation at the maximum of the spectral characteristic has a sublinear character at high excitation levels: $U_{pc}\sim F^{2/3}$, where $F$ is the radiated power (Fig. 3). The analysis of this dependence was described in detail in Ref. 3, based on a model of the variation of the ratio between the concentrations of recombination and attachment centers for the nonequilibrium carriers as a function of the level of illumination.

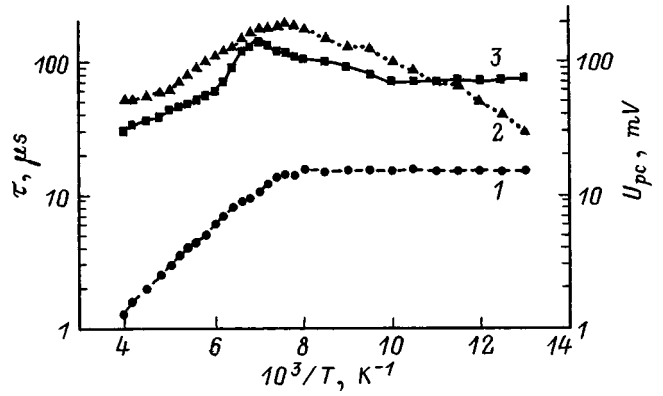


FIG. 4. Temperature dependence of the characteristic photoresponse relaxation times $\tau$ of a $Hg_{0.1}Cd_{0.9}Te$ sample for the slow (*2*) and fast (*1*) components ($\tau_2$ and $\tau_1$), as well as of the amplitude of the photoresponse $U_{pc}$ (*3*).

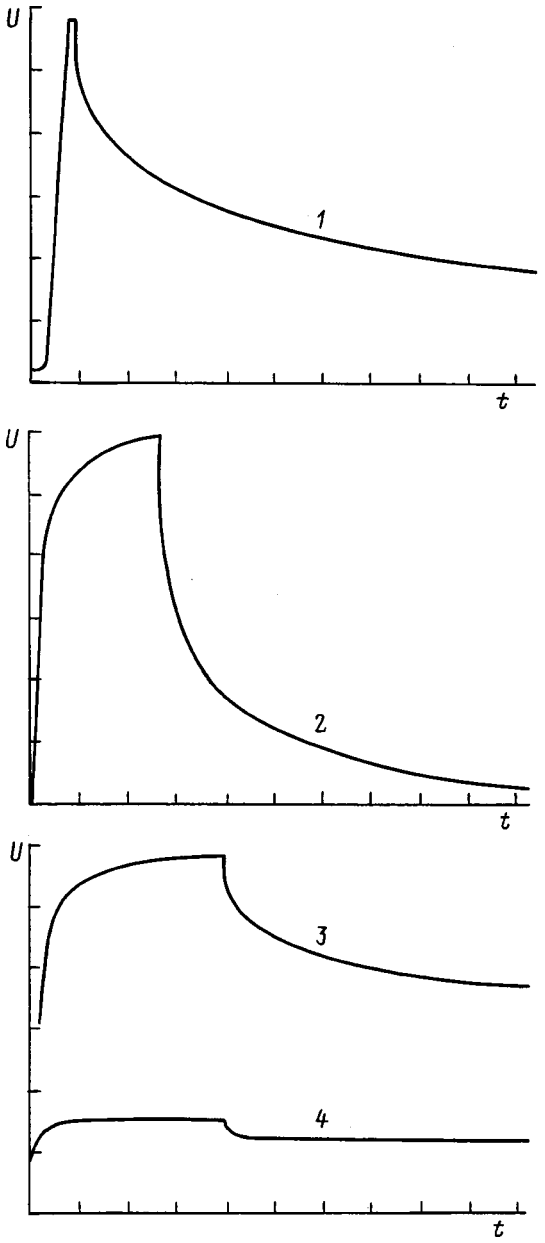


FIG. 5. Oscillograms of the variation of the photoresponse $U$ with the time $t$ for a $Hg_{0.1}Cd_{0.9}Te$ sample at 77 K (*1*, *2*) and of the infrared photoconductivity quenching process (*3*, *4*). *1* — exciting pulse duration equal to 10 ns, $\lambda=0.33$ $\mu$m; scales: $U=2$ mV/division, $t=20$ $\mu$s/division. *2* — exciting pulse duration equal to 1 ms, $\lambda=0.9$ $\mu$m; scales: $U=1$ mV/division, $t=1$ $\mu$s/division. *3* — without infrared illumination. *4* — with infrared illumination at $\lambda=1.1$ $\mu$m; scales: $U=5$ mV/division, $t=20$ $\mu$s/division.

In most cases with excitation of the samples by short light pulses (10 ns) the photocurrent relaxation curves have two components, viz., a fast component ($\tau_1=10^{-5}$ s) and a

slow component ($\tau_2 = 10^{-4}$ s) (Fig. 4). The temperature dependences of the slow components pass through a maximum in the temperature range 200−150 K with an activation energy $E_{i3} = 70-110$ meV in different samples. The course of the stationary lifetime of the nonequilibrium carriers ($t_{ss} \sim U_{pc}/\mu_p$) exhibits a sharp drop at low temperatures, attesting to the asymmetry of the electron and hole capture rates. This provides some basis to assume that in the case of excitation by short pulses, recombination of the nonequilibrium carriers, like the recombination observed in CdTe crystals, is controlled by fast (*s*) and slow (*r*) centers[4] (Fig. 5, curve *1*). When the sample is illuminated by long pulses ($\Delta\tau \sim 1$ $\mu$s), only the slow component associated with *r* centers is observed on the photoresponse relaxation curve (Fig. 5, curve *2*).

During infrared quenching of the photoresponse ($\lambda \simeq 1.1$ $\mu$m) (Fig. 5, curves *3* and *4*), both components persist, providing evidence that the concentration of *r* and *s* centers are roughly equal ($r/s \sim 1$), but the slow *r* energy levels are attachment centers, which strongly influence the relaxation processes in crystals of the compositions under consideration.[5]

The proposed scheme of recombination phenomena qualitatively explains the temperature dependences of the photoconductivity relaxation processes in $Hg_{1-x}Cd_xTe$ crystals with high values of *x*.

[1] S. S. Varshava, A. S. Ostrovs'ka, and G. M. Potapchuk, Ukr. Fiz. Zh. **38**, 398 (1993).
[2] I. V. Kurilo, S. P. Pavlishin, S. N. Bekesha, G. A. Il'chuk, and Yu. G. Akhromenko, Izv. Akad. Nauk SSSR, Neorg. Mater. **23**, 228 (1987).
[3] A. Rose, *Concepts in Photoconductivity and Allied Problems* [Interscience, New York, 1963; Mir, Moscow, 1966].
[4] V. E. Lashkarev, A. V. Lyubchenko, and A. V. Sheĭnkman, *Nonequilibrium Processes in Photoconductors* [in Russian], Naukova Dumka, Kiev, 1981.
[5] V. E. Lashkarev, A. V. Lyubchenko, and M. K. Sheĭnkman, Fiz. Tverd. Tela (Leningrad) **7**, 1727 (1965) [Sov. Phys. Solid State **7**, 1388 (1965)].

Translated by P. Shelnitz

# Nature of the nuclei for thermal donor formation in silicon (or another variant of accelerated oxygen diffusion)

V. B. Neĭmash,*) E. A. Puzenko, A. N. Kabaldin, A. N. Kraĭchinskiĭ, and N. N. Kras'ko

*Institute of Physics, Ukrainian National Academy of Sciences, 252650 Kiev, Ukraine*
(Submitted July 21, 1998; accepted for publication May 19, 1999)
Fiz. Tekh. Poluprovodn. **33**, 1423–1427 (December 1999)

The influence of preliminary heat treatment at 800 °C on the accumulation and annealing kinetics of thermal donors formed at 450 °C in silicon single crystals is investigated by performing four-point measurements of the electrical resistivity. The activation energies for the generation and annealing of thermal donors were found to increase appreciably after preliminary heat treatment at 800 °C. The experimental results are discussed with consideration of the role of the various phase states of oxygen in as-grown Si. An interpretation is proposed with allowance for the effect of the internal elastic stresses created by microfluctuations of the oxygen and thermal donor concentrations in the Si lattice on the diffusion coefficient of oxygen atoms. A quantitative estimation of the dimensions of the microfluctuations gives a value on the order of hundreds of angstroms. The generation and annealing kinetics of thermal donors are described within the Kaizer–Frisch–Reiss model with allowance for the locally accelerated (within the microfluctuations) diffusion of oxygen. The microfluctuations contain roughly 1−3% of the total number of oxygen atoms in the crystal. This low percentage complicates the observation of the accelerated diffusion of oxygen by direct methods, but is sufficient for thermal donor generation. © *1999 American Institute of Physics.* [S1063-7826(99)00512-8]

The efficiency of the formation of oxygen-related thermal donors (oxygen thermal donors) at 450 °C exhibits a significant dependence on the preliminary heat treatment of silicon crystals.[1,2] One of the reasons for it may be the dissolution of any thermal-donor nuclei, which are always present in an as-grown crystal, during preliminary heat treatment.[3] In the Kaizer–Frisch–Reiss (KFR) model[4] the nuclei for the thermal donor complexes $SiO_m$ are $SiO_{m-1}$ complexes, which are their direct precursors. However, at 450 °C a diffusion constant ($D_0$) of oxygen in Si several orders of magnitude higher than the real value is required for the formation of even the complex with $m=2$. Moreover, it is difficult to account for the existence of the microclusters of oxygen thermal donors observed in Refs. 5–8. One possible explanation may be based on the assumption that there are microfluctuations of the oxygen impurity concentration, where the local concentration of oxygen atoms ($O_i$) significantly exceeds the mean value, in as-grown Si.[9] In this case the $O_i$ atoms can initially be close enough to one another that complexes can form. In addition, the diffusion coefficient $D_0$ in the strongly stressed regions of the crystals affected by these microfluctuations can differ greatly from the value of $D_0$ in the remaining volume. Thus, the microfluctuations can also be associated with the concept of nuclei for thermal donors. However, their influence on the accumulation and annealing kinetics of oxygen thermal donors following preliminary high-temperature treatment can differ significantly from the influence of nuclei in the form of $SiO_{m-1}$ precipitates.

In this paper we describe the results of an experimental study of the generation and annealing of oxygen-related thermal donors at 450 °C (450 °C oxygen thermal donors) in Si preliminarily heat-treated at 800 °C for the purpose of ascertaining which of the two models of the nuclei just described corresponds to experiment.

Samples of dislocation-free Si with an as-grown resistivity $\rho=25-40\ \Omega\cdot$cm prepared without any heat treatment after growth were used. The spread of initial values of $\rho$ is due to the different local concentrations of oxygen thermal donors in different parts of the crystal

$$n_0=n_P+n_{GTD},$$

where $n_0$ is the free-electron concentration in the as-grown samples, $n_P$ is the phosphorus impurity concentration, $n_{GTD}$ is the concentration of growth thermal donors, and $n_P/n_{GTD}=1-2$. The concentrations of oxygen and carbon impurities determined from the infrared absorption at wavelengths of 9.1 and 16.5 $\mu$m in a light beam measuring 10×3 mm were equal to $(8-10)\times10^{17}\,cm^{-3}$ and less than $5\times10^{16}\,cm^{-3}$, respectively. The measurements of $\rho$ were performed by the four-point probe technique at room temperature. The free-electron concentration ($n_e$) was determined from the values of $\rho$ under the assumption that $\mu=1350$ $cm^2/(s\cdot V)$. The total concentration of all the types of thermal donors ($N_{TD}$) was determined from the difference $n_i-n_0$ ($n_0$ and $n_i$ are the free-electron concentrations in the as-grown and heat-treated samples, respectively) without allowance for the thermal acceptors, which form at 800 °C after 30 min, since their concentration $n_a<3\times10^{13}\,cm^{-3}$. The distance between the probes was 1 mm. Samples of identical asymmetric shape were fixed during the measurements in a special socket, which ensured repeated placement

 

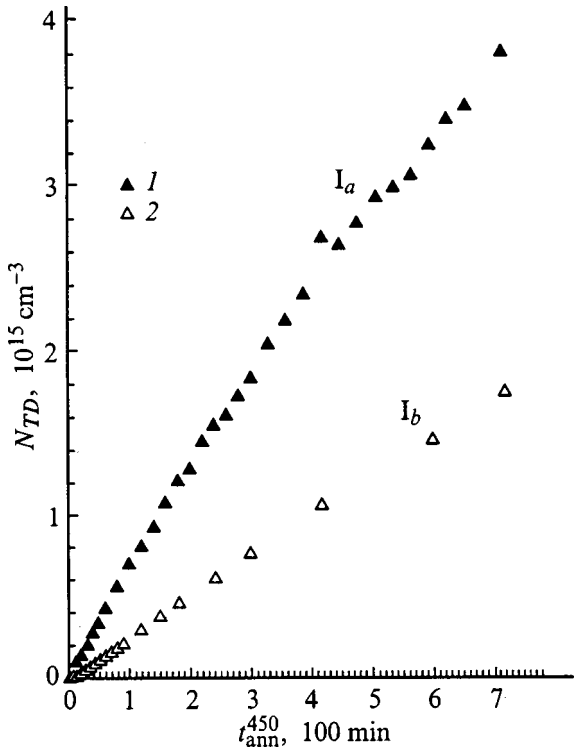


FIG. 1. Dependence of the thermal donor density $N_{TD}$ on the heat-treatment time at 450 °C ($t_{ann}^{450}$) for different samples: *1* — $I_a$, as-grown sample; *2* — $I_b$, sample preliminarily treated at 800 °C for 30 min.

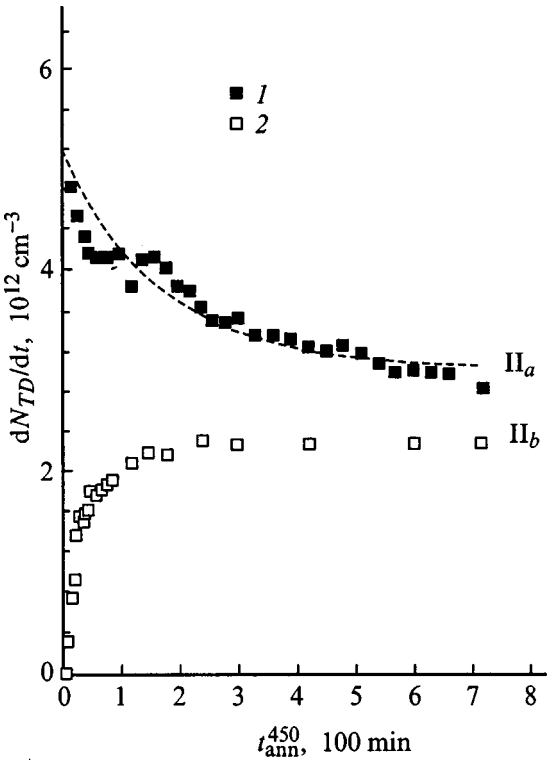


FIG. 2. Dependence of the rate of thermal donor generation $dN_{TD}/dt$ on the heat-treatment time at 450 °C ($t_{ann}^{450}$) for different samples: *1* — $II_a$, as-grown sample, *2* — $II_b$, sample preliminarily annealed at 800 °C for 30 min.

of the probes on a sample to within 0.3 mm. The nonuniformity of the distribution of $\rho$ on the scale of the distance between the probes in the radial direction in an ingot was 37–40%. Heat treatment at 800 °C for 30 min reduced this nonuniformity to 16–22%. This means that the nonuniformity of $\rho$ is largely due to the nonuniform distribution of the growth thermal donors. The nonuniformity of the distribution of the growth thermal donors, in turn, is naturally associated with the nonuniform distribution of $O_i$ during crystal growth.

The samples were sorted into three groups on the basis of the as-grown values of $\rho$: I — 25 Ω·cm, II — 30 Ω·cm, III — 40 Ω·cm. All the heat treatments and measurements were carried out on sets of samples containing one sample from each group. Isothermal heat treatment at 450±1 °C in air was employed to generate thermal donors. The duration of each heat-treatment step was 5–20 min. After each heat-treatment step, $\rho$ was measured at the same place on the sample.

Figure 1 shows typical plots of $N_{TD}$, and Fig. 2 shows plots of $dN_{TD}/dt$ versus the heat-treatment time at 450 °C ($t_{ann}^{450}$) for as-grown samples (*1*) and samples preliminarily treated at 800 °C for 30 min (*2*). It is seen that thermal donor generation is slowed significantly after preliminary heat treatment at 800 °C, while the IR absorption band of $O_i$ remains almost unchanged after such heat treatment. This is evidence that only slight changes occur in the phase state of the bulk of the oxygen atoms in the crystals investigated. The rate of thermal donor generation ($dN_{TD}/dt$) in all cases varies with the heat-treatment time at 450 °C. This variation is more rapid in the earliest stages of the heat treatment, in contradiction to the kinetics of homogeneous precipitation according to the KFR model. The fundamental change in the course of the dependence of $dN_{TD}/dt$ on the heat-treatment time at 450 °C is significant. While the rate of thermal donor generation decreases relative to the initial rate in the as-grown samples, it increases after preliminary heat treatment at 800 °C.

This finding is similar to the behavior observed in Refs. 2 and 10 and can be attributed to the equally successful influence of preliminary heat treatment at 800 °C on the nuclei for the complexes of both types discussed above. In one case this influence reduces to the dissolution of $SiO_{m-1}$ precipitates. In the other case it reduces to ''resorption'' of the microfluctuations as a result of the diffusion and precipitation of $O_i$ atoms in the densest central parts of the microfluctuations.

Preference for a particular type of nuclei for the complexes can be indicated by an experiment on the influence of preliminary heat treatment at 800 °C on the annealing of oxygen thermal donors. In fact, if the nuclei are uniformly distributed $SiO_{m-1}$ precipitates, preliminary heat treatment at 800 °C can only reduce their number (and, accordingly, the rate of thermal donor generation), but is incapable of influencing the annealing of the oxygen thermal donors. If the nuclei are microfluctuations, an influence of preliminary heat treatment at 800 °C on the annealing kinetics of oxygen thermal donors can be expected on the basis of their mutual influence. In fact, according to this model oxygen thermal

donors are found in microclusters with a large local concentration at the sites of microfluctuations in an as-grown crystal.[5] Point defects located in the deformation field of other defects (for example, *A* centers in regions of disorder following neutron irradiation or near dislocations) can significantly alter the parameters of their annealing.[12] Preliminary heat treatment at 800 °C is capable of lowering the local concentration of $O_i$ in microfluctuations and, thus, the local concentration of oxygen thermal donors in the microclusters. Therefore, alteration of the annealing kinetics of oxygen thermal donors can be expected after preliminary heat treatment at 800 °C, since the mutual influence of the oxygen thermal donors weakens.

The annealing of oxygen thermal donors formed at 450 °C was studied in our work at two temperatures: $T=510$ and 515 °C. At these temperatures the annealing of 450 °C oxygen thermal donors is accompanied by the formation of other species of thermal donors (although it is significantly slower than at 450 °C). However, the effective rate of their generation is at least 5 times smaller than the annealing rate of 450 °C oxygen thermal donors. Therefore, their contribution to the kinetics of the electron density during the annealing of 450 °C oxygen thermal donors can be disregarded.

As an example, Fig. 3 shows plots of the dependence of the thermal donor concentration $N_{TD}$ on the annealing time at 515 °C ($t_{ann}^{515}$) for samples with thermal donors generated at 450 °C without preliminary heat treatment (*1*) and for samples after preliminary heat treatment at 800 °C (*2*). Similar plots were constructed for annealing at 510 °C, for annealing of the thermal donors generated at 450 °C without preliminary heat treatment and thermal donors generated at 450 °C after preliminary heat treatment at 800 °C. The plots thus obtained of the dependence of the concentration of 450 °C oxygen thermal donors on the annealing time at 510 °C have a form qualitatively similar to the plots shown in Fig. 3.

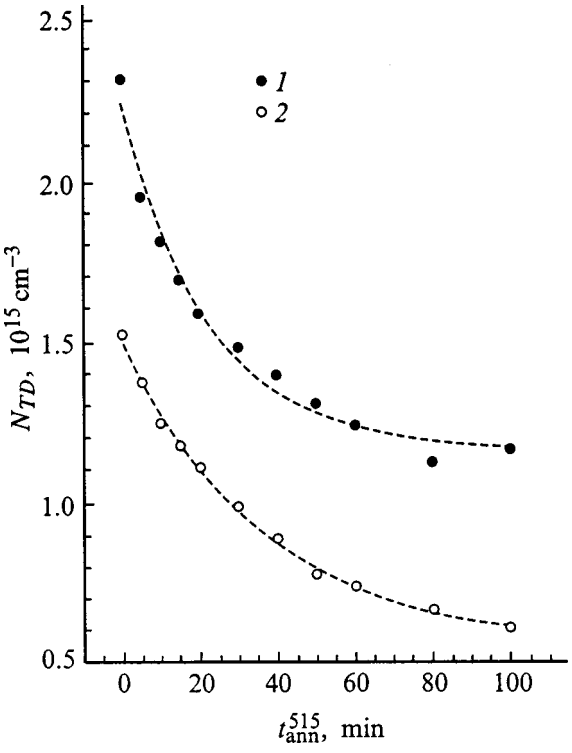


FIG. 3. Dependence of $N_{TD}$ on the annealing time at 515 °C ($t_{ann}^{515}$) for different samples: *1* — after annealing at 450 °C, *2* — sample subjected, in addition, to preliminary heat treatment at 800 °C. Dashed lines — approximation of the form $y=A_0\exp(-t/\tau)$.

In Fig. 3 the points correspond to experimental data, and the dashed lines represent a computer approximation of an exponential function of the form $y=A_0\exp(-t/\tau)$. It is seen that the experiment is faithfully described by a single exponential function. This occurs in all twelve samples. The conclusion drawn in Ref. 11 regarding the two-step annealing of 450 °C oxygen thermal donors is probably due to the small number of experimental points. Thus, preliminary heat treatment at 800 °C significantly slows the annealing of 450 °C oxygen thermal donors at $T=510$ and 515 °C. As was noted above, this finding can support the second theory regarding the nature of the nuclei for thermal donor formation (microfluctuations of the oxygen impurity concentration), i.e., the increased uniformity of the spatial distribution of the oxygen impurities as a result of the preliminary heat treatment at 800 °C leads to a more uniform distribution of the thermal donors themselves and, accordingly, to weakening of their mutual influence through deformation fields, which slows their annealing. In other words, the microclusters of thermal donors formed in crystals preliminarily heat-treated at 800 °C become looser. Thus, the mutual influence of the thermal donors comprising them weakens, and the facilitated annealing of the defects in clusters subsides. In fact, the activation energy for annealing ($E_a$) and the annealing frequency factor ($\nu$), which we determined from experiments on the annealing of 450 °C oxygen thermal donors at $T=510$ and 515 °C, increase significantly after preliminary heat treatment at 800 °C. For different groups of samples we obtained $E_a=1.64-1.88$ eV, $\nu=6.3\times10^8-2.3\times10^7\ s^{-1}$ without preliminary heat treatment and $E_a=2.3-2.47$ eV, $\nu=1.8\times10^{11}-2.4\times10^{12}\ s^{-1}$ after preliminary heat treatment at 800 °C. Moreover, the fairly broad ranges of values for their parameters with measurement errors amounting to $\Delta E_a=\pm0.05$ eV and $\Delta\nu=\pm5\times10^{10}\ s^{-1}$ in both cases are probably due to the already macroscopically inhomogeneous (with a scale equal to the probe spacing) distribution of the microfluctuations themselves. This is supported by the following fact. The rate of thermal donor generation in samples with differences in the integral $O_i$ concentration amounting to less than 20% ($N_O$ was determined from the absorption of infrared radiation in a light beam with a cross section measuring 10×3 mm) can differ by a factor of 4 (when the measurements are performed by the four-point probe technique with a distance between the measuring probes equal to 1 mm). The results of measurements performed on a group of 12 samples unequivocally attest to a general tendency for increases in the activation energy and the frequency factor for the annealing of 450 °C oxygen thermal donors after preliminary heat treatment at 800 °C. It is difficult to attribute such an increase to a decrease in the concentration of nuclei in the form of $SiO_{m-1}$ precipitates during the preliminary heat treatment at 800 °C. Assuming that the nuclei are mi-

crofluctuations, we can attribute the variation of the annealing parameters to the influence of elastic stresses in the lattice, which are created by the microfluctuations and the corresponding clusters of thermal donors. A similar approach was used in Ref. 12, in which the influence of dislocations on the parameters of the annealing of radiation defects in Si was considered.

In the KFR model the diffusion of oxygen atoms is the main factor limiting both the formation of thermal donors and their annealing. Therefore, a change in $E_a$ can characterize a change in the conditions for the diffusion of $O_i$ to a certain extent. Then the increase in $E_a$ following preliminary heat treatment at 800 °C signifies slowing of the diffusion of $O_i$ in the vicinity of thermal donor complexes. The reason for this may be a decrease in the local elastic stresses of the crystal within the thermal-donor clusters due to loosening of the clusters as a consequence of the ''resorption'' of the as-grown microfluctuations of the $O_i$ concentration during the preliminary heat treatment at 800 °C. As can be seen from the results presented, the activation energy $E_a = 2.3 - 2.47$ eV for the ''slowed'' (after preliminary heat treatment at 800 °C) diffusion is close to the value of the activation energy for dispersed $O_i$ (Ref. 13). For the samples without preliminary heat treatment at 800 °C we have $E_a = 1.64 - 1.88$ eV, which corresponds to the activation energy for the generation of 450 °C oxygen thermal donors known from the reports of other investigators,[14] which was explained by advancing the hypothesis of the ''accelerated'' diffusion of $O_i$. Based on the results obtained, we can assume that the ''accelerated'' diffusion of $O_i$ during thermal donor generation is characteristic only of oxygen atoms which are in stressed regions of the crystal within microfluctuations with high values of $N_O$. Their fraction out of the total number of $O_i$ atoms probably does not exceed 1–2% (Ref. 9). However, it is fully sufficient for explaining the real rates of thermal donor generation in the initial stages. We shall next quantitatively analyze the experimental results obtained using such an approach.

Let us consider the annealing at $T = 510$ °C of samples which underwent preliminary heat treatment at 800 °C before the heat treatment at 450 °C. The annealing of 450 °C oxygen thermal donors (we assume that they are $SiO_m$ complexes) at 510 °C occurs mainly by means of dissociation, since the limiting size of the oxygen precipitates in silicon at 450 °C is smaller than the critical size of precipitation nuclei at 510 °C (Ref. 15).

The annealing kinetics of defects can be written in the relaxation time approximation:

$$\frac{dN}{dt} = -\frac{N}{\tau}, \tag{1}$$

$$\frac{1}{\tau} = \nu \exp(-E_a/kT), \tag{2}$$

where $N$ is the defect density at the time $t$.

In the case of the annealing of a thermal-donor complex via dissociation, an oxygen atom must move away to a certain distance $\Delta x$ in order not to be recaptured by the complex. The value of $\Delta x$ can be determined from the relation

$$\Delta x = \sqrt{D_x \tau}, \tag{3}$$

where $D_x$ is the diffusion coefficient of dispersed oxygen. We can calculate $\Delta x$ for various values of $D_x$ obtained by different investigators. For $D_x = 0.09 \exp(-2.4kT)$ from Ref. 16 at $T = 510$ °C the value of $\Delta x$ equals 30 Å. For $D_x = 0.07\exp(-2.44kT)$ (Ref. 17) $\Delta x = 21$ Å; for $D_x = 0.02 \times \exp(-2.42kT)$ (Ref. 15) $\Delta x = 13$ Å; and for $D_x = 0.17 \times \exp(-2.54kT)$ (Ref. 18) $\Delta x = 16$ Å.

Let us now consider the case of the annealing of 450 °C oxygen thermal donors without preliminary heat treatment at 800 °C. According to the data in Ref. 14, the activation energy for the accumulation of 450 °C oxygen thermal donors is $E_a = 1.7 \pm 0.1$ eV. We obtained the same value of $E_a$ from the experiment on the annealing of 450 °C oxygen thermal donors without preliminary heat treatment. The equality between the values of the activation energies for generation and annealing makes it possible to assume that the disappearance of thermal donors (during annealing at higher temperatures) is also limited by the diffusion of $O_i$. We can write a relation similar to (3), in which $D_x = 6.26 \times 10^{-3} \exp(-1.8kT)$ is the diffusion coefficient of oxygen obtained from the experiment on the formation of 450 °C oxygen thermal donors in Ref. 14. Substituting the corresponding experimental values of $\tau$, we obtain $\Delta x = 730$ Å, i.e., we find that in the case of the annealing of thermal donors generated without preliminary heat treatment at 800 °C, the distance $\Delta x$ increases by 40 fold with a considerable decrease in the activation energy of the process. The existence of deformation fields (with an energy exceeding $kT$ at $T = 510$ °C) of such expanse would be more plausible within microfluctuations of the oxygen impurity concentration or thermal-donor clusters (with dimensions on the order of hundreds of angstroms and a local concentration substantially exceeding the mean value) than near nuclei in the form of $SiO_{m-1}$ precipitates.

Thus, the quantitative analysis of the experimental results obtained by us provides evidence in support of the hypothesis of the accelerated diffusion of oxygen within microfluctuations and microclusters of thermal donors. The fraction of oxygen atoms located in microfluctuations does not exceed several percent of their total number; therefore, it would be difficult to detect the accelerated diffusion of $O_i$ by direct methods.

The foregoing analysis of the results has an approximate character. However, in our opinion, it is sufficient for drawing the following conclusions.

1. In thermal donor generation the role of the ''nuclei'' (in the sense of the additional factors stimulating the precipitation of $O_i$) is played by microfluctuations of the concentration of $O_i$ extending over distances on the order of 700 Å.

2. The generation and annealing of thermal donors in microclusters at the sites of as-grown microfluctuations of the oxygen impurity concentration are greatly facilitated by the accelerated diffusion of $O_i$ in the elastic deformation fields near and within microclusters of thermal donors and microfluctuations.

*)E-mail: vova@neimash.elvisti.kiev.ua

[1] C. S. Fuller, J. A. Ditzenberg, N. B. Hannay, and E. Buehler, Phys. Rev. **96**, 833 (1954).
[2] V. M. Babich, N. I. Bletskan, and E. F. Venger, *Oxygen in Silicon Single Crystals* [in Russian], Naukova Dumka, Kiev, 1997.
[3] L. I. Murin and V. P. Markevich, in *Proceedings of the International Conference on Science and Technology of Defect Control in Semiconductors, Yokohama, Japan, 1989*, edited by K. Sumino (North-Holland, Amsterdam, 1990), p. 190.
[4] W. Kaizer, H. Frisch, and H. Reiss, Phys. Rev. **112**, 1546 (1958).
[5] O. M. Kabaldin, V. B. Neĭmash, V. M. Tsmots', V. I. Shakhovtsov, and V. S. Shtim, Ukr. Fiz. Zh. **40**, 218 (1995).
[6] A. N. Kabaldin, V. B. Neĭmash, V. M. Tsmots', V. I. Shakhovtsov, A. V. Batunina, V. V. Voronkov, G. I. Voronkova, and V. P. Kalinushkin, Ukr. Fiz. Zh. **38**, 34 (1993).
[7] O. M. Kabaldin, V. B. Neĭmash, V. M. Tsmots', and L. I. Shpinar, Ukr. Fiz. Zh. **40**, 1079 (1995).
[8] N. T. Bagraev, N. A. Vitovskiĭ, L. S. Vlasenko, E. V. Mashovets, and O. Rakhimov, Fiz. Tekh. Poluprovodn. **17**, 1979 (1983) [Sov. Phys. Semicond. **17**, 1263 (1983)].
[9] D. I. Brinkevich, V. P. Markevich, L. I. Murin, and V. V. Petrov, Fiz. Tekh. Poluprovodn. **26**, 682 (1992) [Sov. Phys. Semicond. **26**, 383 (1992)].
[10] V. P. Markevich and L. I. Murin, Phys. Status Solidi A **111**, K149 (1989).
[11] Yu. M. Babitskiĭ, P. M. Grinshteĭn, M. A. Il'in, and V. P. Kuznetsov, Fiz. Tekh. Poluprovodn. **18**, 1280 (1984) [Sov. Phys. Semicond. **18**, 799 (1984)].
[12] L. A. Kazakevich and P. F. Luganov, Élektron. Tekh., Ser. Mater., No 9, 170 (1982).
[13] G. D. Watkins, J. W. Corbett, and R. S. McDonald, J. Appl. Phys. **53**(10), (1982).
[14] L. I. Murin and V. P. Markevich, Fiz. Tekh. Poluprovodn. **22**, 1324 (1988) [Sov. Phys. Semicond. **22**, 840 (1988)].
[15] R. C. Newman, M. J. Binns, F. M. Livingston, and S. Messoloras, Physica B **116**, 264 (1983).
[16] Y. Takano and M. Maki, in *Semiconductor Silicon 1973*, edited by H. R. Huff and R. R. Burgess (Electrochemical Society, Pennington, 1973), p. 469.
[17] J. C. Mikkelsen, Jr., Appl. Phys. Lett. **40**, 336 (1982).
[18] M. Stavola, J. R. Patel, L. C. Kimerling, and P. E. Freeland, Appl. Phys. Lett. **42**, 73 (1983).

Translated by P. Shelnitz

# Donor-acceptor photoluminescence of weakly compensated GaN:Mg

V. Yu. Nekrasov, L. V. Belyakov, O. M. Sreseli,*) and N. N. Zinov'ev

*A. F. Ioffe Physicotechnical Institute, Russian Academy of Sciences, 194021 St. Petersburg, Russia*
(Submitted May 21, 1999; accepted for publication June 23, 1999)
Fiz. Tekh. Poluprovodn. **33**, 1428–1435 (December 1999)

An analysis of the time-resolved photoluminescence spectra of magnesium-doped layers of gallium nitride grown by molecular epitaxy on GaAs and sapphire substrates is presented. New characteristic features of Mg impurities and their interaction with intrinsic defects, which are manifested via a mechanism of donor-acceptor recombination, are discovered. The donor-acceptor optical transitions in a doped, weakly compensated broad-band semiconductor are considered theoretically under the assumption of a nonrandom distribution of the impurities. A quantitative analysis of the donor-acceptor photoluminescence spectra of diverse samples of GaN:Mg epilayers reveals depletion at short distances in the distribution of the donors and acceptors and/or the presence of a predominant distance between impurities (singularities), depending on the growth conditions. The following are determined from a comparison of the calculated and experimental dependences of the time-resolved photoluminescence: the form of the interimpurity distribution function, the dopant concentration, and the binding energies of the acceptors (Mg atoms) and active donors. © *1999 American Institute of Physics.* [S1063-7826(99)00612-2]

## 1. INTRODUCTION

Despite the formidable advances in the practical development of light-emitting devices based on gallium nitride, many points are still unclear in the mechanism underlying the influence of the doping of GaN on its luminescence properties. GaN layers obtained without doping are characterized by an electronic type of conduction. As in the case of other broad-band compounds, the doping of gallium nitride with acceptor-like impurities is a complex subject. At present, the only dopant which provides relatively stable and reproducible *p*-type conductivity in GaN is magnesium. The introduction of magnesium (as well as other impurity elements) is accompanied by the generation of a considerable number of intrinsic defects and, possibly, by the appearance of impurities in the unionized state. The implantation of such centers in a crystal obviously has a significant influence on the optical and electrical properties of gallium nitride. In particular, the appearance of the broad band at 2.8–3.3 eV in the photoluminescence (PL) spectrum of GaN is assigned to donor-acceptor (DA) recombination.[1,2] The significant differences discovered in the particular features of the donor-acceptor PL spectrum of different samples of GaN:Mg (the spectral position of the maximum, the lineshape, and the unusual decay kinetics for DA recombination)[1–3] require a deeper understanding of the doping processes and of the interaction of an acceptor-like impurity with intrinsic defects in gallium nitride and further investigation of intrinsic DA recombination under the conditions of an inhomogeneous distribution of the impurities.

The foundation of the theory and experiment in the area of donor-acceptor recombination was laid long ago.[4,5] It is based on the model of a defect-free crystal with a random distribution of the impurities. The recombination of electrons and holes localized at spatially separated impurity centers is determined by processes involving tunneling and the Coulomb interaction between individual impurities. On the other hand, the donor-acceptor PL band is a result of averaging of the contributions of radiative transitions between individual centers. As a result, the measured DA recombination band occupies a broad spectral range and can have a complex form. The maximum of the band is located in the interval between the energy specified by the total recombination energy of a donor-acceptor pair,

$$E_{\mathrm{DAP}}(\infty)=E_G-(\Delta E_D+\Delta E_A) \tag{1}$$

($E_G$ is the gap width, $\Delta E_D$ and $\Delta E_A$ are the ionization energies of the donor and acceptor centers), which corresponds to an infinite distance between the donors and acceptors, and the energy

$$E_{\mathrm{DAP}}=E_{\mathrm{DAP}}(\infty)+E_C, \tag{2}$$

where $E_C=e^2/4\pi\varepsilon\varepsilon_0 r$. We note that the magnitude of the Coulomb contribution $E_C$ does not depend on the type of DA pairs or on the mean distance between impurities, which is proportional to $n_{D,A}^{1/3}$ ($n_{D,A}$ denotes the concentration of donors and acceptors) and is determined entirely by the random variable $r$, i.e., the distance between the donor and the acceptor. As a consequence of the interaction between impurities and intrinsic defects during growth, definite correlations are possible in the relative positions of the impurities in the lattice. If such impurity associations appear, they should have a decisive influence on the kinetics of donor-acceptor recombination and can be characterized by investigating the kinetics of the PL of DA pairs. Such possibilities open up new prospects, not accessible to other methods, for investigating a material.

 

The large probability of radiative interband transitions in direct-gap semiconductors precludes achievement of the equilibrium values specified by (1) for the spectral position of the donor-acceptor PL band. This is because a considerable portion of the electrons and holes bound to impurities recombine by means of tunneling transitions between nearest neighbors. In view of the nonequilibrium character of DA recombination noted, estimation of the characteristic recombination energies from the positions of the maxima of the lines for DA pairs using (1) can lead to erroneous identification of the impurity transitions in experiments performed under stationary excitation conditions.

Thus, not only the spectroscopic energies of the impurities, but also the correlation function in the positions of the dopant and the intrinsic compensating defects can be determined from investigations of donor-acceptor PL. Accordingly, the kinetics of DA recombination take on special importance. In this paper we present the results of an experimental study of time-resolved PL spectra and the decay kinetics of a pulse-excited PL flash in gallium nitride slightly doped with magnesium. Donor-acceptor PL is considered phenomenologically under the conditions of a correlation between the positions of the donors and acceptors for an arbitrary ratio between the Bohr radii of the donors and acceptors. Several important numerical characteristics, such as the concentration of the majority impurity, the binding energies of the impurities of both types, the character of the interimpurity correlations, the recombination probabilities, etc., are determined by comparing calculated plots of the donor-acceptor PL kinetics and experimental results.

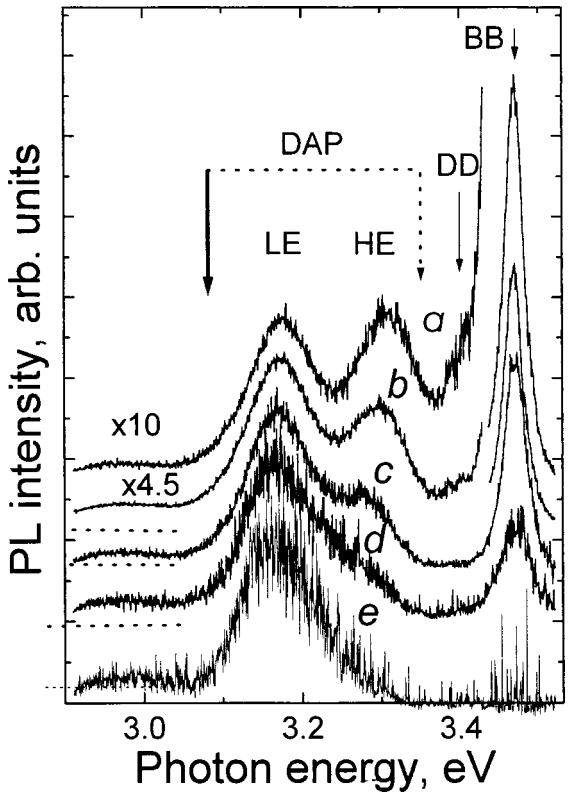


FIG. 1. Time-resolved photoluminescence (PL) spectra of weakly compensated GaN:Mg on a GaAs substrate (sample mg521). Delay time for recording the spectrum relative to the excitation pulse $t_d$, ns: a — 0, b — 10, c — 40, d — 200, e — 1000.

## 2. EXPERIMENTAL METHOD

We investigated samples of GaN lightly doped with magnesium (the magnesium concentration was $1.5\times10^{18}$ $cm^{-3}$ according to SIMS) with a concentration of ionized acceptors $n_A=1.5\times10^{17}\,cm^{-3}$, which was determined from Hall measurements. Samples in the form of films of thickness $0.5-2.0$ $\mu$m were grown by molecular-beam epitaxy on GaAs and sapphire substrates by Prof. Foxon's team in the University of Nottingham. The growth technology was described elsewhere.[6] The photoluminescence (PL) was investigated on combined spectroscopic instrumentation, which included single and double monochromators with diffraction gratings, a photon-counting system operating in a time-resolved regime (using a boxcar integrator), a cryostat with temperature regulation from 4.2 to 300 K, and a control and recording computer system. The PL was excited by a pulsed nitrogen laser with a photon energy $h\nu=3.678$ eV, a pulse duration of 6 ns, and a frequency of $\sim$400 Hz. An excitation level less than 1000 W/cm$^2$ was provided when the diameter of the laser beam on the sample was $\sim$1 mm. This enabled us to avoid introducing the nonlinear effects associated with a high excitation and stimulated-emission intensity. A set of calibrated neutral filters was used to vary the excitation intensity. Auxiliary PL measurements were performed under stationary conditions with excitation by a He–Cd laser ($h\nu=3.8$ eV) and recording of the signal in a phase-sensitive detection regime. The experimental spectral plots are presented with consideration of the spectral sensitivity of the measuring system (the photomultiplier and the monochromator).

## 3. EXPERIMENTAL RESULTS

Figure 1 shows time-resolved PL spectra of a sample of lightly doped gallium nitride (*p*-GaN:Mg deposited on a GaAs substrate), which were obtained at $T=77$ K. The temperature $T=77$ K was chosen because the PL of DA pairs is weakly temperature-dependent at $T<100$ K and, at the same time, the spectral features associated with exciton-impurity complexes do not mask the laws governing donor-acceptor PL at $T>40$ K. In order to isolate the time dependence of the spectral distribution of the PL, the spectra in Fig. 1 were normalized to the PL intensity at $E_{PL}=E_{DAP}(\infty)$ (the heavy arrow in Fig. 1). The value of $E_{DAP}(\infty)$ is discussed in detail in Sec. 5.

We assign peak BB at $E_{PL}=3.47\,eV\approx E_G$ to the interband recombination of free carriers in two overlapping channels: shallow-donor–valence-band and free-exciton recombination (as was noted above, the emission of bound excitons is quenched at temperatures above 40–50 K). The FWHM of the BB peak is $\sim$30 meV and decreases slowly as the temperature is lowered. The small feature on the low-energy side of the principal PL peak, peak DD, is caused, in our opinion, by deep-donor–valence-band recombination and is discussed below in greater detail. As the delay time is in-

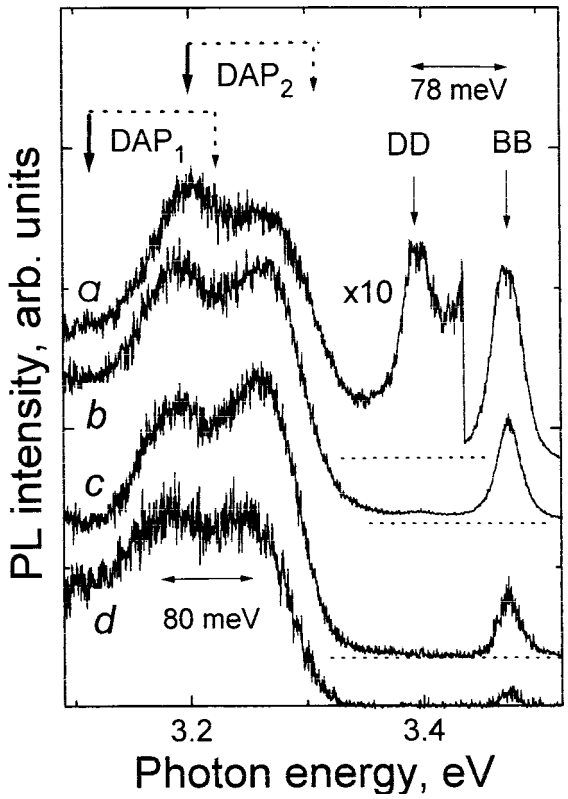


FIG. 2. Time-resolved photoluminescence (PL) spectra of weakly compensated GaN:Mg on a sapphire substrate (sample mg389). Delay time for recording the spectrum relative to the excitation pulse $t_d$, ns: a — 0, b — 50, c — 200, d — 2000.

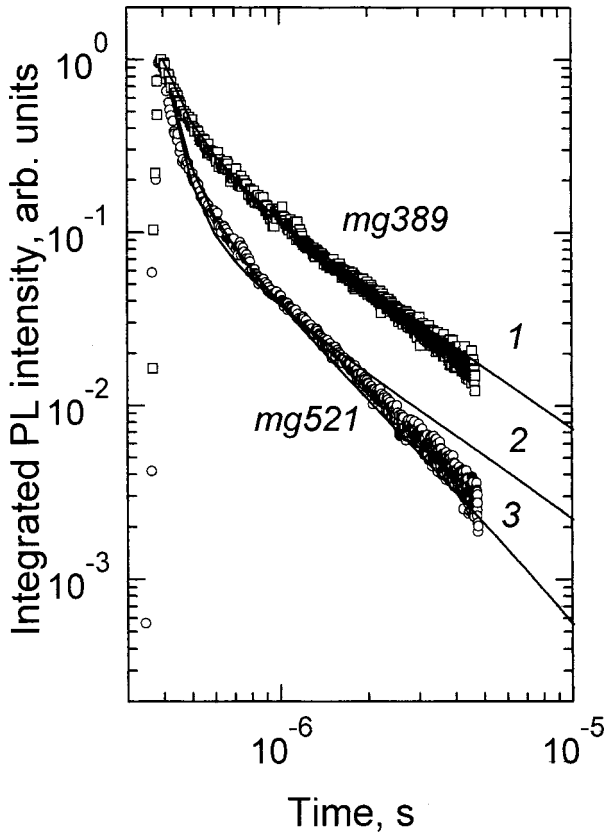


FIG. 3. Kinetics of the donor-acceptor photoluminescence (PL) band for samples mg521 and mg389. Points — experimental data, solid curves — computer calculation for concentrations equal to $9\times10^{17}\,\mathrm{cm}^{-3}$ (*1*, *2*) and $3\times10^{18}\,\mathrm{cm}^{-3}$ (*3*) and the distribution functions $G_2(r)$ (*1*) and $G_1(r)$ (*2*, *3*).

creased, the energetic position of peak BB remains nearly constant, while its amplitude drops sharply during the first 10 ns after the excitation pulse.

The main feature distinguishing the spectra obtained with short delays ($t_d \ll 1$ $\mu$s) from the quasi-steady-state ($t_d > 1$ $\mu$s) and the steady-state spectra known from the literature is the complex character of the band assigned to DA recombination. As can be seen from Fig. 1, the DAP band consists of two peaks, viz., LE and HE. The low-energy (LE) component depends only slightly on the recording time of the spectrum relative to the exciting pulse; nevertheless, a small reproducible shift to lower energies is observed. Conversely, the parameters of the new high-energy (HE) component depend strongly on the delay time $t_d$. As $t_d$ is increased, the band red-shifts fairly quickly, and its amplitude decreases considerably more rapidly than does the amplitude of the LE component. Only the LE band remains in the spectra recorded with large delays under the corresponding quasistationary conditions (curve *e* in Fig. 1).

Figure 2 shows the time-resolved spectra for another sample of *p*-GaN:Mg, which had roughly the same degree of compensation, but was grown on a different substrate, viz., $Al_2O_3$. At first glance, the main features persist in the PL spectra, i.e., there are two DA recombination bands ($DAP_1$ and $DAP_2$), the edge band BB, and the low-energy shoulder DD. However, significant differences are observed in the PL kinetics. Most importantly, the high-energy component of the donor-acceptor PL does not vanish when the spectrum is measured with a large delay relative to the exciting pulse; this component shifts slowly as the delay time is increased, and its kinetics are very similar to the behavior of the low-energy band. The increase in the intensity of band DD varies from sample to sample. We associate the blue shift in the position of peak BB at $E_{\mathrm{PL}} = 3.475$ eV by $\sim$5 meV with the different character of the stresses on the GaN/sapphire boundary than on the GaN–GaAs boundary. It should be noted that the behavior of the DA band noted above is characteristic not just of the epilayers on sapphire. For example, very complicated behavior was also observed for one of the GaN samples grown on a GaAs substrate.

Figure 3 shows kinetic plots of the decay of the intensity of the donor-acceptor PL band measured in the energy range from 3.05 to 3.37 eV for two samples. The differences obtained are striking. While a segment of rapid PL decay at short times can be discerned for one sample (mg521), the time dependence of the other sample (mg389) is characterized by monotonic decay. The time dependence of the donor-acceptor PL intensity has a strongly nonexponential, nearly power-law, character with an exponent of $\sim(-2)$ at large times.

The investigations of the dependence of the time-resolved spectra on the intensity of the exciting light $I_{\mathrm{exc}}$ showed that the variation of $I_{\mathrm{exc}}$ within several orders weakly influences the spectral features of DA recombination. Nevertheless, relative redistribution of the PL intensities in the

spectrum between donor-acceptor PL and interband PL with increasing $I_{exc}$ is observed perfectly clearly with the expected dominance of band BB at high pump levels.

The experimental data presented demonstrate the high sensitivity of the donor-acceptor PL spectra to the characteristic features of GaN epilayers that depend on the growth characteristics and the nature of the substrate. Samples of GaN:Mg with roughly the same doping level exhibit two types of spectra in the donor-acceptor PL band with very different kinetics.

## 4. RECOMBINATION UNDER THE CONDITIONS OF INTERIMPURITY CORRELATIONS

The quantitative solution of the problem of the PL of DA pairs was considered in Refs. 4 and 5 in the approximation of a uniform distribution of the impurities. The results of that phenomenological theory qualitatively describe the behavior of DA recombination in a series of conventional semiconductors (IV, III–IV, and II–VI) with crystal structures of high perfection, although the comprehensive comparison of theory and experiment is essentially confined to Ref. 4. Nevertheless, it was noted in some cases that the experimentally observed features differ from the laws predicted by the theory.[4] For GaN we note the observations in Ref. 3 that were left unexplained and our experimental data, which were presented in the preceding section.

In this section we examine the model of DA recombination with the following significant generalizations, which differ from those considered in Ref. 4. First, we assume an arbitrary distribution of the impurities in the lattice and introduce the correlation function $G(r)$, which specifies the density of the distribution of the impurities (donors and acceptors) in the space of interimpurity distances $r$. Second, we assume an arbitrary ratio between the Bohr radii of the donors ($a_D$) and acceptors ($a_A$) in the problem of the recombination of an electron and a hole localized on neighboring centers. In fact, a rough estimate of the ratio between the Bohr radii in GaN suggests $a_D \sim (3-5)a_A$, rather than $a_D \gg a_A$.

Let us calculate the recombination rate of donor-acceptor pairs, following the initial assumptions in Ref. 4. We assume that a neutral donor is found at the origin of coordinates in an environment of $N_A$ acceptors located at the positions $r_i$. Let $N_A > N_D$, i.e., let the acceptors be the majority dopant, and let the donors be the minority impurity, which compensates for the effect of doping by the acceptors. For each donor there are $N_A$ parallel channels for recombination with acceptors, and the probability of recombination of an electron ($e$) located at a donor center with a hole ($h$) bound to the $i$th acceptor center depends on the distance $r_i$ between them. Denoting the filling factor of the donors with electrons by $Q$ and using $W(r_i)$ to denote the probability for the radiative recombination of a bound $e-h$ pair separated in space by the distance $r_i$, we write the rate of variation of the filling factor as

$$\frac{dQ}{dt} = -Q\sum W(r_i). \tag{3}$$

This equation has the solution

$$Q(t) = \exp\left[-\sum W(r_i)t\right]. \tag{4}$$

We obtain the filling factor averaged over all possible interimpurity configurations, i.e., values of $r_i$, $\langle Q(t)\rangle$ by multiplying (4) by the probability of a given configuration and summing over all possible configurations:

$$\langle Q(t)\rangle = \left[\frac{1}{V}\int_V G(r)\exp[-W(r)t]\,d^3r\right]^{N_A}. \tag{5}$$

The quantity $d^3r/V$ is the probability of finding an impurity in the volume $d^3r$ when the donors (acceptors) are uniformly distributed in the volume $V$, and the correlation function $G(r)$ is the density of the probability distribution characterizing the relative distribution of donor-acceptor pairs in the space of interimpurity distances $r$. Imposing the normalization condition

$$\frac{4\pi}{V}\int_0^\infty G(r)\,r^2dr = 1$$

on $G(r)$, after some simple transformations we obtain

$$\langle Q(t)\rangle = \exp\left[4\pi n_A\int_0^\infty G(r)\{\exp[-W(r)t]-1\}\,r^2dr\right]. \tag{6}$$

Here $n_A = N_A/V$. The PL intensity as a function of time, $I_{PL}(t)$, is determined by the rate of variation of $\langle Q(t)\rangle$:

$$I_{PL}(t) = -\frac{d\langle Q(t)\rangle}{dt} = 4\pi n_A\int_0^\infty G(r)W(r) \times \exp[-W(r)t]\,r^2dr\exp\left[4\pi n_A\int_0^\infty G(r) \times\{\exp[-W(r)t]-1\}\,r^2dr\right]. \tag{7}$$

It is noteworthy that Eq. (7) describes the variation of the integrated PL of the DA pairs, rather than the intensity of an individual band in the PL spectrum. The latter can also be calculated with allowance for the fact that an individual pair separated by the distance $r_1$ emits a photon with the energy $E_1 = e^2/4\pi\varepsilon\varepsilon_0 r_1$, which is measured relative to $E^0_{PL} = E_{DAP}(\infty) = E_G - (\Delta E_D + \Delta E_A)$. Thus, the filling factor of the state of a particular DA pair is defined as

$$Q_{E_1}(t) = \exp[-W(r_1)t]\exp\left[-\sum_{i\neq 1} W(r_i)t\right]. \tag{8}$$

The subscript 1 in (8) denotes the pair singled out. The deexcitation rate of this particular state also determines the spectral PL intensity, which, after averaging over an ensemble of DA pairs, can be brought into the form

$$J_E(t) = W(r_1)\exp[-W(r_1)t]\exp\left[-\sum_{i\neq 1} W(r_i)t\right] \approx W(r)\exp[-W(r)t]\cdot\langle Q(t)\rangle. \tag{9}$$

The difference between ensembles of $N_A - 1$ and $N_A$ pairs is ignored in performing the averaging in (9). This is valid in

the approximation of $N_A \gg 1$. After the averaging, if we omit the subscript 1 ($r_1 \Rightarrow r$) and define the number of acceptors in the epilayer between $r$ and $r+dr$ as $dN = G(r)N_A 4\pi r^2 dr$, we obtain the PL intensity in the energy band between $E$ and $E+dE$, which, after switching from the spatial coordinate to the recombination energy $E$ using the relation $r = e^2/4\pi\varepsilon\varepsilon_0 E = A_C/E$, can be expressed in the form

$$\frac{dI_E(t)}{dE} = 4\pi n_A A_C^3 G\left(\frac{A_C}{E}\right)\frac{1}{E^4} W\left(\frac{A_C}{E}\right) \times \exp\left[-W\left(\frac{A_C}{E}\right)t\right]\cdot\langle Q(t)\rangle. \quad (10)$$

To calculate the PL spectra within this model, we must find the function $W(r)$, which, in turn, is defined by the square of the overlap integral of the wave functions of an electron at a donor and a hole at an acceptor. In the previous studies[4,5] an expression obtained in a very simple approximation, in which the Bohr radii of the acceptor and donor differ strongly, served as $W(r)$. In that case $W(r) = W_0 \exp(-2r/r_B)$, where $r_B = \max(a_D, a_A)$ is the Bohr radius of the more weakly bound center. However, the Bohr radii of shallow hydrogen-like impurities generally differ by only several factors. This situation significantly modifies the values of $W(r)$ in the most important region of variation of $r$ from $\sim 0$ to $\max(a_D, a_A)$. The behavior of $W(r)$ in this region is the main factor determining the entire kinetics of donor-acceptor PL. Under the assumption that the ground states of electrons and holes at impurities can be described by $s$-type functions, the overlap integral is given by the equality

$$I_{D-A}(r) = \frac{1}{\pi(a_D, a_B)^{3/2}}\int_0^\infty \exp\left(-\frac{R}{a_A}\right)\exp\left(\frac{|R-r|}{a_D}\right) d^3R. \quad (11)$$

The calculation of this integral for an arbitrary ratio between $a_D$ and $a_A$ leads to the following expression for the probability of the tunneling recombination of a bound electron and a bound hole $W(r)$:

$$W = \text{const}\cdot 64\left\{\beta^3\left\|\left[\beta(1-\beta^2) + 4\frac{\beta(1-e^{\rho})}{\rho}\right]e^{-\rho} + \left[1-\beta^2 - 4\frac{\beta(1-e^{\beta\rho})}{\rho}\right]e^{-\beta\rho}\right\|^2/(1-\beta^2)^6\right\}. \quad (12)$$

Here $\beta = a_A/a_D$, $\rho = r/a_A$, and $\beta\rho = r/a_D$, respectively. We note that const$\cdot 64\beta^3$ is exactly equal to $W_0$ in the expression for $W(r)$ used in Ref. 4 and in the ensuing studies.

## 5. DISCUSSION OF THE EXPERIMENTAL RESULTS

Let us move on to a comparison of the dependences calculated from (7), (10), and (12) to the experimental data. The parameters in the calculation are the concentration of the majority impurity, $n_A$, the Bohr radii of the donor and the acceptor, $a_D$ and $a_A$, respectively, and the correlation function $G(r)$. The analytic form of (7), (10), and (12) allows us to reduce the calculation problem to the dimensionless parameters $a_A^3 n_A$ and $\beta$ (or $W_0$) and the coordinate $\rho$. Iterative computer simulation of the PL spectra and the time dependences was carried out according to the following self-consistent procedure to compare the theoretical results with experiment. The time dependences of the donor-acceptor PL (7) and spectral series of the time-resolved spectra (10) for various values of the delay time $t_d$ with a typical number of spectra in each series equal to $\sim 5-10$ were calculated simultaneously. The parameters $a_D$, $a_A$, $\beta$, and $W_0$, which are constants of the material, were set equal to constant values for all the samples investigated in the final iterations. Thus, the only variable parameters for different samples in the last stage of the calculation were the concentration of the majority impurity $n_A$ and the distribution function $G(r)$, which were varied to achieve the closest fit between the theoretical and experimental dependences.

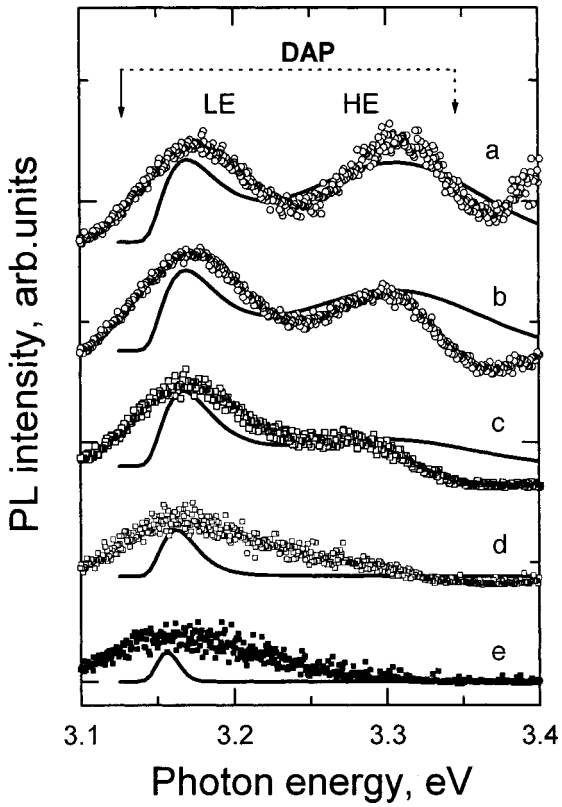


FIG. 4. Calculated (solid curves) and experimental (points) time-resolved donor-acceptor photoluminescence (PL) spectra of sample mg521 from the first group (Fig. 1). $t_d$, ns: a — 0, b — 10, c — 40, d — 200, e — 1000.

Comparisons of the calculation and the experimental spectra in the region of donor-acceptor PL shown in Figs. 1 and 2 are made in Figs. 4 and 5, respectively. We note not only the good fit between the calculated curves and the experimental dependences, but also the repetition of the dynamics of the variation of peak HE with time for the sample of the first type in the calculated curves. The complicated form of the donor-acceptor PL spectrum, as well as the differences in the transformation of the donor-acceptor PL spectra obtained for different GaN:Mg samples with time, are, in fact, specified by the distribution function $G(r)$ (Fig. 6). The presence of peak HE in the spectra of a number of samples is caused by the maximum of $G_1(r)$ at $r \simeq 7$ Å. In these samples the relative fraction of impurities separated from one another by large distances is fairly small. The correlations

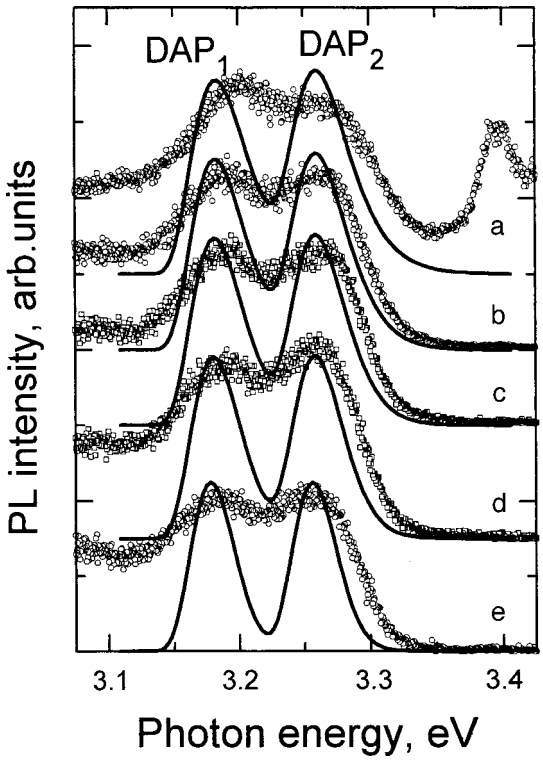


FIG. 5. Calculated (solid curves) and experimental (points) time-resolved donor-acceptor photoluminescence (PL) spectra of sample mg389 from the second group (Fig. 2). $t_d$, ns: a — 0, b — 50, c — 100, d — 200, e — 500.

noted imply the appearance of a certain preferential short-range order in the distribution of the impurities. The presence of this maximum in the relative distribution of the impurities is probably due to the unique self-compensation mechanism of Mg, i.e., complexation with intrinsic defects

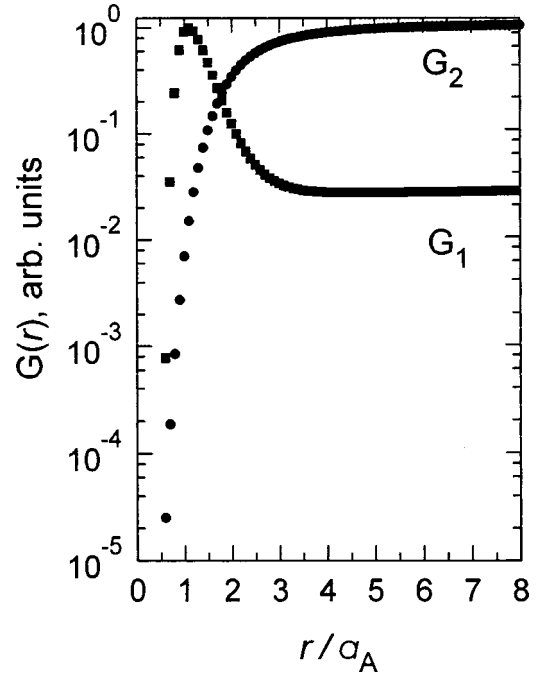


FIG. 6. Distribution function of DA pairs $G(r)$ for GaN:Mg: $G_1$ — sample mg 521 (Figs. 1 and 4); $G_2$ — sample mg389 (Figs. 2 and 5).

formed when the majority impurity is introduced. We note that both the character and the magnitude of the self-compensation effect of the acceptor impurity introduced depend on the growth parameters, i.e., in the final analysis on the level of nonstoichiometry.[6] The correlation function $G_2(r)$ for the samples of the second type, which are characterized by two bands of slow donor-acceptor PL, is likewise not constant at any $r$. However, in contrast with the samples of the first group, they exhibit depletion of the impurities at short distances (Fig. 6, curve *2*). Such behavior signifies weaker compensation by the implanted impurity as a result of neutralization by intrinsic defects.

The fast component in the time dependence of the donor-acceptor PL $I_{\mathrm{PL}}(t)$ of the sample of the first type (mg521) at short times (Fig. 3) is also caused by the correlation between the positions of the acceptors and the compensating intrinsic defects (donors). This feature, i.e., the fast component of $I_{\mathrm{PL}}(t)$ at short times, was first observed in Ref. 3, but was left unexplained.

The data obtained on a large series of GaN:Mg samples demonstrate the correspondence between the characteristic features of the spectra and kinetic measurements in the samples for which the high-energy band in the PL spectrum does not vanish with large delay times and the fast component is not observed in the decay kinetics of the donor-acceptor PL (see Fig. 3, curve *1*). The $I_{\mathrm{PL}}(t)$ curve for such samples is characterized by a power-law function. Thus, the features of $G(r)$ are manifested both in series of time-resolved spectra and in the time dependence of the donor-acceptor PL.

The values of the concentration determined by secondary-ion mass spectrometry (SIMS), $n_{\mathrm{Mg}}^{\mathrm{SIMS}}$, in Ref. 6 are in reasonably good agreement with the values determined by comparing the theoretical and experimental dependences ($n_{\mathrm{Mg}}^{\mathrm{PL}}$): $n_{\mathrm{Mg}}^{\mathrm{PL}}/n_{\mathrm{Mg}}^{\mathrm{SIMS}} \sim 1-2$. The slight systematic upward deviation of the values of $n_{\mathrm{Mg}}^{\mathrm{PL}}$ obtained by us in comparison with the SIMS data[6] can be attributed to some indefiniteness in the calibration of the SIMS spectrometer, which was based on the use of a secondary, or ''reference,'' sample.

Returning to the DA recombination spectra, we turn our attention to the unique ''doublet'' structure, which is displayed especially clearly in the second group of samples with large delay times: in all the samples investigated the spectral distance between the peaks of the double maximum of the donor-acceptor PL band amounts to ~80 meV. This is the same energy which we observe as the energy gap between bands DD and BB. We associate the presence of two donor-acceptor PL bands with two different families of DA pairs. One forms from a shallow donor and a Mg acceptor, and the other forms from a deep donor and a Mg acceptor. Thus, the duplication of the DA band is due to the participation of two different donors in the donor-acceptor transitions. It is known that at moderately low temperatures the main contribution to peak BB is made by the recombination of free excitons and of carriers in shallow-donor–valence-band transitions. We assume that the center of gravity of line BB is located below the true conduction-band edge, being separated from it by $\Delta E \sim 30$ meV. Here $\Delta E \sim \Delta E_D, R_X$, where

$\Delta E_D$ is the binding energy of the donor (shallow), and $R_X$ is the binding energy of free excitons in GaN.

All the spectra also display peak DD, which is located ~80 meV below the principal peak. This peak has characteristic decay times which are similar to those observed for peak BB and mimic the time-resolution limit of the system ($\sim 10^{-9}$ s). Such behavior of band DD is characteristic of impurity-band recombination. The optical energy of peak DD can be assigned to the binding energy of a deep donor, which we estimate as $\Delta E_{\mathrm{DD}} \sim (100 \pm 3)$ meV. Such deep donors can be, for example, intrinsic defects. The relative amplitude of peak DD with respect to the principal band BB varies from sample to sample, but it always remains distinguishable against the background of the latter band. We note that the agreement achieved between the calculated and experimental time dependences, which was demonstrated above in Figs. 4 and 5, was obtained for the following Bohr radii of a deep donor and an ordinary donor: $a_{\mathrm{DD}} \approx 14$ Å and $a_D \approx 25$ Å, respectively. It must be stressed that the shape and character of the calculated time dependence are very sensitive to the values of these parameters. The donor Bohr radius thus determined corresponds to a donor binding energy $\Delta E_{\mathrm{DD}} \sim 100$ meV, which appreciably exceeds the binding energy of a shallow hydrogen-like donor in GaN,[7] but corresponds well to the binding energy determined from the spectra for the deep donor participating in DA transitions that is associated with the DD band. We can therefore estimate the optical binding energies of the participating intrinsic donor defects in the following crude classification: $\Delta E_{\mathrm{DD}} \sim (100 \pm 3)$ meV for the deep donor and $\Delta E_D \sim (30 \pm 3)$ meV for the shallow donor. Using the values obtained for the energies of the donors participating in the DA transitions, we can determine the optical binding energies of the acceptor-like Mg centers that participate in the recombination. First of all, the ''zero'' energy $E_{\mathrm{PL}} = E_{\mathrm{DAP}}(\infty) = E_G - (\Delta E_D + \Delta E_A)$ was determined from the limiting value of the spectral position of the DA band for $t \to \infty$ in the calculated spectrum. The value of $\Delta E_D$ was estimated on the basis of the values of $a_D$ and $a_{\mathrm{DD}}$ that are determined and from the positions of peaks BB and DD, respectively. Assuming that the intrinsic defects appearing upon doping comprise two groups of donors with energies of ~30 meV (Ref. 7) and ~100 meV, we obtain the level of a Mg acceptor $\Delta E_A^{\mathrm{Mg}} \sim (240 \pm 10)$ meV, which fits the known values of the binding energy of magnesium in GaN: 150–300 meV (see, for example, Refs. 8–11). We note that we determined these energies on the basis of a comparison of a series of time-resolved PL spectra with spectra calculated from (12), where the ''zero'' energy $E_{\mathrm{PL}} = E_{\mathrm{DAP}}(\infty) = E_G - (\Delta E_D + \Delta E_A)$ was selected on the basis of the limiting value of the spectral position of the DA band for $t \to \infty$ in the calculated spectrum.

## 6. CONCLUSIONS

Time-resolved spectra and the kinetics of donor-acceptor recombination in magnesium-doped gallium nitride with *p*-type conduction have been investigated. The correlation spectrum of Mg-acceptor–intrinsic-defect complexes has been determined by comparing experimental data with series of calculated spectra and time dependences obtained on the basis of a modified version of the theory in Ref. 4 under the assumption of an arbitrary distribution of the impurities and an arbitrary ratio between the Bohr radii of the donors and acceptors. A method for determining the parameters of the dopant and its interaction with intrinsic defects has been developed. The binding energies of Mg acceptors (240 meV) and two intrinsic donor defects, viz., a deep donor (100 meV) and a shallow donor (30 meV), have been determined.

This work was carried out with financial support from INTAS (Grant 94-2608).

N.N.Z. thanks B. S. Monozon for a discussion of the theoretical part of this study.

*)E-mail: olga.sreseli@pop.ioffe.rssi.ru

[1] H. Amano, M. Kito, K. Hiramatsu, and I. Akasaki, J. Electrochem. Soc. **137**, 1639 (1990); I. Akasaki, H. Amano, M. Kito, and K. Hiramatsu, J. Lumin. **48–49**, 666 (1991).
[2] T. Detchprohm, K. Hiramatsu, N. Sawaki, and I. Akasaki, J. Cryst. Growth **145**, 192 (1994).
[3] M. Ilegems and R. Dingle, J. Appl. Phys. **44**, 4234 (1973); Solid State Commun. **9**, 175 (1973).
[4] D. G. Thomas, J. J. Hopfield, and W. M. Augustyniak, Phys. Rev. **140**, 202 (1965); C. H. Henry, R. A. Faulkner, and K. Nassau, Phys. Rev. **183**, 798 (1969); P. J. Dean, *Progress in Solid State Chemistry*, edited by J. O. McCaldin and G. Somorjai (Oxford, Pergamon Press, 1973), Vol. 8, p. 1.
[5] F. Williams, Phys. Status Solidi **25**, 493 (1968).
[6] T. S. Cheng, C. T. Foxon, N. J. Jetts, D. J. Dewsnip, L. Flannery, J. W. Orton, S. V. Novikov, B. Ya. Ber, and Yu. A. Kudriavtsev, MRS Internet J. Nitride Semicond. Res. **2**, Article 13 (1997).
[7] W. Götz, N. M. Johnson, C. Chen, H. Liu, C. Kuo, and W. Imler, Appl. Phys. Lett. **68**, 3144 (1996).
[8] W. Götz, N. M. Johnson, J. Walker, D. P. Bour, H. Amano, and I. Akasaki, Appl. Phys. Lett. **67**, 2666 (1995).
[9] W. Götz, N. M. Johnson, and D. P. Bour, Appl. Phys. Lett. **68**, 3470 (1996).
[10] P. Hacke, H. Nakayama, T. Detchprohm, K. Hiramatsu, and N. Sawaki, Appl. Phys. Lett. **68**, 1362 (1996).
[11] M. Smith, G. D. Chen, J. Y. Lin, H. X. Jiang, A. Salvador, B. N. Sverdlov, A. Botchkarev, H. M. Morkoç, and B. Goldenberg, Appl. Phys. Lett. **68**, 1883 (1996).

Translated by P. Shelnitz

# Cascade capture of electrons by dislocations in many-valley semiconductors

Z. A. Veliev

*Yu. G. Mamedaliev Nakhichevan State University, 373630 Nakhichevan, Azerbaijan*
(Submitted August 25, 1998; accepted for publication June 24, 1999)
Fiz. Tekh. Poluprovodn. **33**, 1436–1437 (December 1999)

The process of electron capture in many-valley semiconductors in a quantizing magnetic field is investigated theoretically. An analytical expression is obtained for the cross section of electron capture by dislocations. It is found that the electron capture cross section depends substantially on the orientation of the valley relative to the magnetic field. © *1999 American Institute of Physics.* [S1063-7826(99)00712-7]

The influence of charged edge dislocations on the properties of semiconductors depends strongly on the interaction of the charge carriers with the dislocations, on the physical situation, and also on the actual structure of the crystals.[1] The properties of charged dislocations have been mainly investigated experimentally in Ge and Si crystals, which are many-valley semiconductors. The constant-energy surface for the electronic conductivity at the $L$ and $X$ points is a prolate ellipsoid. In silicon there are six equivalent valleys located at the $X$ points on the $\langle 100\rangle$ axis.[2] In germanium the valleys are located at the $L$ points in the $\langle 111\rangle$ direction and the number of equivalent valleys is equal to four.

In the present paper we examine the cross section for electron capture by dislocation centers in many-valley $n$-type semiconductors in the presence of a quantizing magnetic field. The electron capture cross section $\sigma$ is calculated on the basis of the modified edge-dislocation model proposed by Shikin and Shikina.[3] According to their model,[3] the deformation potential of the dislocation creates a distinct potential well for the electrons, which increases the rate of capture of electrons.

Let us investigate the temperature range in which the electrons are scattered by acoustic phonons quasielastically, i.e., the case in which

$$kT \gg \hbar\omega_{\mathbf{q}} \sim (\hbar\Omega m_{\perp} s)^{1/2}.$$

Here $T$ is the lattice temperature, $k$ is the Boltzmann constant, $\hbar\omega_{\mathbf{q}}$ is the energy of an acoustic phonon,

$$\Omega = eH/cm_{\Omega}, \quad \frac{1}{m_{\Omega}^2} = \frac{\cos^2\Theta}{m_{\perp}^2} + \frac{\sin^2\Theta}{m_{\parallel} m_{\perp}}, \tag{1}$$

$\Theta$ is the angle between the magnetic field vector $\mathbf{H}$ and the axis of rotation of the ellipsoid, $m_{\parallel}$ and $m_{\perp}$ are the effective masses of electrons moving along the rotation axis of the ellipsoid and in the plane perpendicular to it, respectively, and $s$ is the speed of sound in the crystal. Under these conditions, the electron loses energy in small amounts and the capture process can be described as a continuous transfer of energy carriers from the region of positive energies to the region of negative energies. The electron is considered to be essentially captured when it drops down below the energy level $E=-kT$.

Let us consider the case of a small concentration of dislocations for which the Reed cylinders of individual dislocations do not intersect and act independently of one another as independent centers. Under these conditions, the electron capture cross section is given by

$$\sigma = J/n_0\langle v\rangle. \tag{2}$$

Here $J$ is the electron flux per dislocation center, $n_0$ is the equilibrium electron density in the bulk of the semiconductor, and $\langle v\rangle$ is the thermal electron velocity. The flux $J$ is calculated as in Ref. 4. Following Ref. 4, we have for $\sigma$

$$\sigma = J/n_0\langle v\rangle = \frac{AkT}{\langle v\rangle}\left(\int_{-\infty}^{0} dE \exp(E/kT)/B(E)\right)^{-1}, \tag{3}$$

where

$$A = \frac{1}{2\alpha}\frac{(2\pi)^{3/2}\hbar^2}{m_{\perp} m_{\parallel}^{1/2}\Omega(kT)^{1/2}},$$

and $\alpha$ is the number of valleys in the conduction band. The quantity $kTB(E)$ is the diffusion coefficient in energy space and is defined by the relation

$$B(E) = \frac{1}{2kTv}\int d^3\mathbf{r}\alpha \sum_{i,j} W_{ij}(\varepsilon_i - \varepsilon_j)^2 \delta(E - \varepsilon_i - \Phi(\mathbf{r})), \tag{4}$$

where $\Phi(\mathbf{r})$ is the total potential energy of the electrostatic and deformation fields of the edge dislocation,[2] the indices $i$ and $j$ denote the triples of quantum numbers of the electrons $(n,k_x,k_z)$ and $(n',k_x',k_z')$, and $W_{ij}$ is the transition probability of the electron from the $i$th to the $j$th quantum state under interaction of the electrons with the acoustic phonons, and in the ultraquantum limit $(n=n'=0)$ has the form

$$W_{ij} = \frac{2\pi}{\hbar}\sum_{\mathbf{q},\alpha}\frac{E_{c\alpha}^2 q\hbar}{2\rho s\alpha v}\delta_{k_x,k_x'+q_x}\delta_{k_z,k_z'+q_z} \times \exp\left(-\frac{q_x^2+q_y^2}{2}\mathbf{r}_H^2\right)[N_{\mathbf{q}}\delta(\varepsilon_i-\varepsilon_j-\hbar\omega_{\mathbf{q}}) + (N_{\mathbf{q}}+1)\delta(\varepsilon_i-\varepsilon_j+\hbar\omega_{\mathbf{q}})]^2, \tag{5}$$

$$\varepsilon_i = \frac{\hbar^2 k_{zi}^2}{2m_{\perp}} + \hbar\Omega\left(n+\frac{1}{2}\right), \tag{6}$$

 

$$r_H=(\hbar c/eH)^{1/2}. \tag{7}$$

Here $\varepsilon_i$ is the electron energy in the $i$th quantum state, $\rho$ is the density of the crystal, and $N_{\mathbf{q}}=kT/\hbar\omega_{\mathbf{q}}$ is the equilibrium distribution function of the phonons.

In this expression, $\alpha=1$ corresponds to the longitudinal branches, $\alpha=2$ corresponds to the transverse branches of the phonon spectrum, and $E_{c\alpha}$ can be represented in the form

$$E_{c\alpha}=\begin{cases}\Sigma_d+\Sigma_u\cos^2\beta & \text{if} \quad \alpha=1,\\ \Sigma_u\sin\beta\cos\beta & \text{if} \quad \alpha=2,\end{cases} \tag{8}$$

where $\Sigma_\alpha$ and $\Sigma_u$ are constants of the deformation potential introduced by Hering, and $\beta$ is the angle between the phonon wave vector $\mathbf{q}$ and the rotation axis of the ellipsoid.

For the quantity $B(E)$, after some straightforward but rather lengthy calculations we have

$$B(E)=\frac{\langle E_c^4\rangle b^2\lambda^2}{6\pi^3\hbar\rho U_0^3}\left(\frac{eH}{c\hbar}\right)^3(m_\perp+m_c)e^{-3|E|/U_0}\times\left\{\ln\frac{U_0}{\sqrt{\hbar\Omega m_\perp s^2}}+\frac{1}{3}+\frac{4U_0}{\hbar\Omega}C(\Theta)\right\}\times\cosh\frac{3\sqrt{\hbar\Omega m_\perp s^2}}{U_0}, \tag{9}$$

$$C(\Theta)=\frac{\sin^2\Theta\cos^2\Theta(m_\parallel-m_\perp)^2+m_z^2}{m_\perp[(m_\parallel m_z)^{1/2}+m_z]}, \tag{10}$$

$$\langle E_c^2\rangle=\left(\Sigma_d^2+\frac{2}{3}\Sigma_d\Sigma_u+\frac{1}{3}\Sigma_u^2\right),\quad m_z=m_\perp^2\sin^2\Theta+m_\parallel\cos^2\Theta.$$

Here $\lambda=(1-2\nu)/(1-\nu)$, $\nu$ is the Poisson coefficient, $b$ is the Burgers dislocation vector, $U_0=2e^2f/a_0\varepsilon$, $a_0$ is the lattice constant, $f$ is the filling coefficient of the dislocation by electrons, and $\varepsilon$ is the dielectric constant.

Substituting expression (9) into Eq. (4), after a straightforward integration, we obtain

$$\sigma=\frac{(2\pi)^{3/2}}{12\pi^3}\frac{b^2\lambda^2\langle E_c^4\rangle}{\langle v\rangle\rho U_0^3}\left(\frac{eH}{\hbar c}\right)^2(m_\perp+m_c)\times\left\{\ln\frac{U_0}{\sqrt{\hbar\Omega m_\perp s^2}}+\frac{1}{3}+\frac{4U_0}{\hbar\Omega}C(\Theta)\right\}\times\cosh\frac{3\sqrt{\hbar\Omega m_\perp s^2}}{U_0}. \tag{11}$$

As can be seen from expression (11), the cross section for capture in a magnetic field depends essentially on the orientation of the valley relative to the magnetic field. Although $\hbar\Omega\gg kT$, under certain physical conditions the term $(U_0/\hbar\Omega)C(\Theta)$ can play an important role because at small values of $\Theta$ the factor $C(\Theta)$ is much greater than 1. In this case $\sigma\sim H$, and for values of $\Theta$ for which $C(\Theta)\lesssim 1$ we have $\sigma\sim H^2$.

In conclusion, let us estimate the quantity $\sqrt{\hbar\Omega m_\perp s^2}$ and determine the region of applicability of formula (11). For $f\simeq 0.1$, $H\simeq 10^5$ Oe, and $s\simeq 5\times 10^5$ m/s the quantity $\sqrt{\hbar\Omega m_\perp s^2}/U_0\simeq 0.1$. The values of the magnetic field for which formula (11) is valid are determined by the inequality

$$(\hbar\Omega m_\perp s^2)^{1/2}<kT\ll\hbar\Omega. \tag{12}$$

This inequality, on the one hand, ensures quasi-elasticity of electron scattering by acoustic phonons and, on the other, that the electron energy spectrum is quantized in a strong magnetic field. Conditions (12) can be written in the form $1\ll(H/H^*)\ll\delta^{-1}$, where $\delta=m_\perp s^2/kT$ and $H^*\simeq(m_\perp c/\hbar e)\times kT\simeq kT/2\mu_B$ ($\mu_B=e\hbar/2m_\perp c$ is the effective Bohr magneton). For $m\simeq 10^{-28}$ g and $T\simeq 300$ K we have $H^*\simeq 250$ Oe.

[1] F. Mataze, J. Appl. Phys. **56** (15), 2605 (1984).
[2] B. K. Ridley, *Quantum Processes in Semiconductors*, 2nd ed. (Oxford Univ. Press, 1988).
[3] V. B. Shikin and Yu. V. Shikina, Usp. Fiz. Nauk 165(8), 887 (1995) [Phys. Usp. **36**, 655 (1995)].
[4] V. N. Abakumov and I. N. Yassievich, Zh. Éksp. Teor. Fiz. **71**(2), 657 (1976) [Sov. Phys. JETP **44**, 345 (1976)].

Translated by Paul F. Schippnick

## SEMICONDUCTORS STRUCTURES, INTERFACE, AND SURFACES

# Electrical properties of $Hg_{1-x}Mn_xTe$-based photodiodes

L. A. Kosyachenko,*) I. M. Rarenko, and O. A. Bodnaruk

*Chernovtsy State University, 274012 Chernovtsy, Ukraine*

Sun Weiguo

*Institute of Optoelectronics, 471009 Loyan, China*

(Submitted February 8, 1999; accepted for publication April 1, 1999)
Fiz. Tekh. Poluprovodn. **33**, 1438–1442 (December 1999)

Electrical properties (at 80 K) of $p-n$ junctions fabricated by ion milling of $p$-type $Hg_{0.91}Mn_{0.09}Te$ are analyzed. The forward current-voltage characteristics at low biases is shown to be governed by carrier recombination in the space charge region and at higher biases its voltage dependence is deformed due to the voltage drop across the high-resistance layer in the diode structure. Under reverse bias, carrier tunneling suppresses other transport mechanisms. At higher reverse biases, impact ionization by high-energy carriers is responsible for the additional increase in the diode current. © *1999 American Institute of Physics.* [S1063-7826(99)00812-1]

### 1. INTRODUCTION

$Hg_{1-x}Mn_xTe$ is a promising material for infrared detectors whose use in comparison with $Hg_{1-x}Cd_xTe$ allows one to enhance the stability of device characteristics.[1–3] For $x=0.09$ $Hg_{1-x}Mn_xTe$ is a semiconductor with a wide band gap $E_g=0.09$ eV at 77 K, i.e., the sensitivity range of a diode based on this material covers both atmospheric ''windows''—3–5 and 8–13 $\mu$m. The $p-n$ junctions, which are suitable for practical use, are fabricated in HgMnTe by diffusion in saturated Hg vapor or by ion implantation with subsequent annealing to eliminate lattice defects.[3–5]

In this paper we report the results of an experimental study of $p-n$ junctions based on $Hg_{0.91}Mn_{0.09}Te$, prepared by ion milling at low accelerating voltages compared with those used in ion implantation.[6] This technique in combination with photolithography and surface passivation has made it possible to fabricate multielement matrices of planar and mesa photodiodes with reproducible and stable properties.[7]

### 2. SAMPLES

To fabricate the photodiodes we used single crystals of $p$-$Hg_{0.91}Mn_{0.09}Te$, obtained by a modified zone melting method.[8] After an extended anneal (several weeks) of the bar at ~200 °C, the hole density in the samples, which was found from the Hall measurements, varied in the range $(1-3)\times10^{16}$ cm$^{-3}$ at 77 K. As a result of ion milling with $Ar^+$ (ion energy 700 eV, current density 0.5 mA/cm$^2$) for 2–2.5 min, the conductivity type in the skin layer of the $p$-HgMnTe sample changes, and a high electron density is observed[7] ($\sim10^{18}$ cm$^{-3}$). The HgMnTe surface was passivated by fluorides of Mn, Te, and Hg formed during anodization in a $NH_4F$ solution in ethylene glycol.[9] A ZnS layer (~0.3 $\mu$m) was also deposited above the fluoride surface (~0.03 $\mu$m). Ohmic contacts with the substrate and the $n$-layer were created by chemical deposition of Pd with subsequent vacuum sputtering of Cr (~0.05 $\mu$m) followed by Au (~1 $\mu$m). The ohmic contact to the $n$-region, whose dimensions are 50 $\times$100 $\mu$m, covers roughly half the active area of the diode (Fig. 1).

### 3. CHARGE TRANSPORT MECHANISM UNDER FORWARD BIAS

Figure 2 shows a typical current–voltage ($I-V$) characteristic of one of the elements of the photodiode of the matrix at $T=80$ K, illustrating the rectifying properties of the investigated $p-n$ junctions (at 0.3 V the forward current exceeds the reverse current by more than two orders of magnitude). A distinguishing feature of the $I-V$ characteristic plotted in semilog coordinates is the presence at $V<0.1$ V of a rectilinear segment with slope nearly coincident with $e/2kT$ ($e$ is the charge of the electron, $k$ is Boltzmann's constant, and $T$ is the temperature). This is evidence of a recombination mechanism of the forward current, which for an asymmetric $p-n$

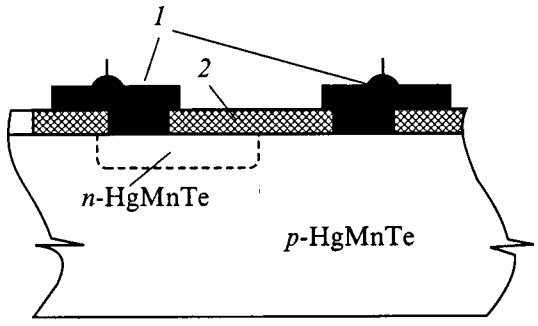


FIG. 1. Structure of a planar HgMnTe photodiode: *1* — metal contacts to the $n$ and $p$ regions, *2* — passivating layer.

 

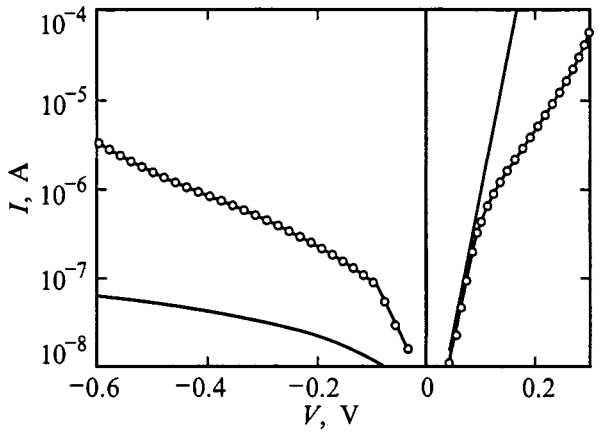


FIG. 2. Current–voltage characteristic of a HgMnTe diode at 80 K. Points — experimental data, solid lines — results of calculations using formulas (1) and (2).

junction for recombination through levels located near the middle of the band gap (the most efficient recombination levels) and $eV \gg kT$ is described by the formula[10,11]

$$I = A\frac{en_i d}{\tau}\frac{kT}{\varphi_0 - eV}\exp\left(\frac{eV}{2kT}\right), \tag{1}$$

where $A$ is the area of the diode, $n_i$ is the intrinsic carrier density, $\tau$ is the effective lifetime of the carriers in the space charge region (SCR), $\varphi_0$ is the height of the potential barrier at the $p-n$ junction, $d=[2\varepsilon\varepsilon_0(\varphi_0-eV)/e^2(N_a-N_d)]^{1/2}$ is the width of the space charge region (in this case the space charge region is located in the $p$-type region, which is a region of much higher resistance), $\varepsilon$ is the relative dielectric constant equal to 17.8 for $Hg_{0.91}Mn_{0.09}Te$ (Ref. 3), $\varepsilon_0$ is the permittivity of free space, and $N_a-N_d$ is the concentration of the uncompensated acceptors in the $p$-type region. [The factor $kT/(\varphi_0-eV)$, whose dependence on $V$ can be ignored in comparison with the exponential function, takes into account the fact that recombination does not take place uniformly over the entire space charge region, but only in some part of it.]

According to formula (1), the cutoff on the current axis (Fig. 2) gives the value $Aed_0kT/\tau\varphi_0$, where $d_0=[2\varepsilon\varepsilon_0\varphi_0/e^2(N_a-N_d)]^{1/2}$ is the width of the space charge region at $V=0$. Assuming for our estimate $\varphi_0 \approx E_g = 0.09$ eV (the value of $E_g$ was found from the optical transmission curve of the substrate) and $(N_a-N_d)=p=2\times10^{16}\,\mathrm{cm}^{-3}$, we obtain $d_0 \simeq 3\times10^{-5}$ cm. For the investigated diodes $A=5\times10^{-5}\,\mathrm{cm}^2$, and for $E_g=0.09$ eV at 80 K $n_i \simeq 10^{14}\,\mathrm{cm}^{-3}$ (Ref. 3). In Eq. (1) the only unknown quantity is therefore the lifetime $\tau$, which must be set equal to $6\times10^{-6}$ s in order to obtain agreement with the experimental dependence (for $V<0.1$ V in Fig. 2). This value is close to the value for $\tau$ in HgCdTe, which was subjected to ion etching.[6]

The deviation from a straight line in Fig. 2 for $V>0.1$ V can be explained by the drop of part of the voltage applied to the diode on the resistance $R_0$ connected in series with the $p-n$ junction. Such a resistance is always present in a diode structure. This shows up, in particular, in the fact that for large forward biases, when the contact potential $\varphi_0/e$ is compensated by the external voltage, the $I-V$ characteristic becomes linear (if $R_0$ is a linear resistance). That this is indeed the case is confirmed by Fig. 3a, which plots the dependence $I(V)$ on regular Cartesian coordinates. As can be seen, when $I>50\,\mu$A, the experimental dependence is represented by a straight line.

#### 4. ENERGY-LEVEL DIAGRAM OF A $p-n$ JUNCTION

Analysis of the results presented in Figs. 2 and 3a leads to the following conclusions.

1. The cutoff on the voltage axis in Fig. 3a gives the value 0.28 V for the contact potential (0.28−0.29 V for the various samples), which is much greater than the value $E_g/e=0.09$ V. Such a large discrepancy is explained by the fact that the $n$ layer of the diode structure formed by ion etching is a degenerate semiconductor. In this case the Fermi level $E_F$ is located above the bottom of the conduction band $E_c$ by the distance $E_F-E_c=(h^2/2m_e^*)(3n/8\pi)^{2/3}$, where $m_e^*$ is the effective mass of the electron, and $n$ is the electron density. Setting $m_e^*=0.01m_0$ ($m_0$ is the electron mass in vacuum),[3] for $n=10^{18}\,\mathrm{cm}^{-3}$ we obtain $E_F-E_c \simeq 0.03$ eV, which also explains the ''anomalously'' large value of $\varphi_0$ that follows from Fig. 3a (taking into account the degeneracy of the $n$ region $\varphi_0=E_F-E_c+E_g-\Delta\mu$, where $\Delta\mu$ is the distance to the Fermi level from the valence band in the $p$ region of the diode structure.

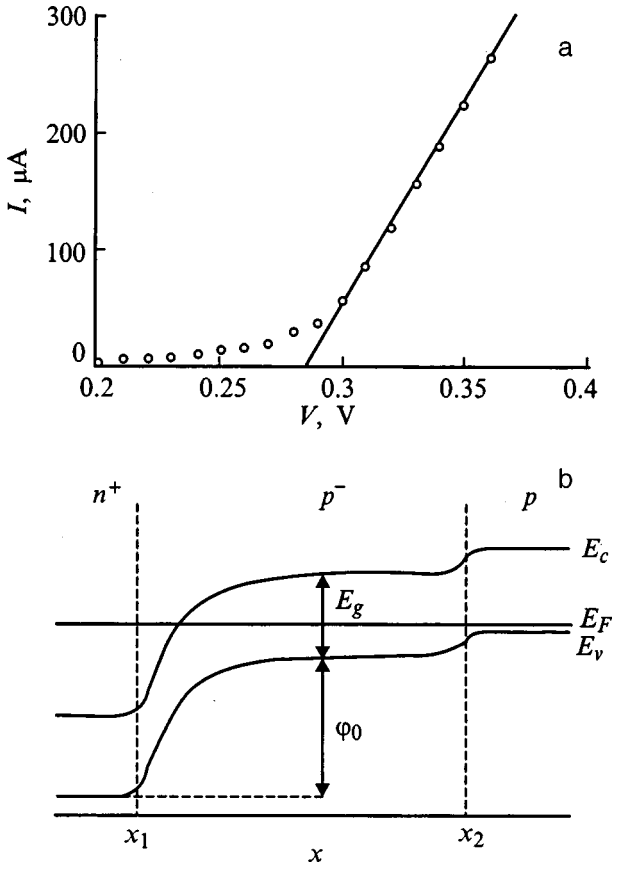


FIG. 3. Current–voltage characteristic of a HgMnTe diode in the region of large direct currents (a) and energy-level diagram of a diode structure based on HgMnTe (b).

2. The value of $R_0=\Delta V/\Delta I$ found from the slope of the rectangular segment in Fig. 3a is equal to $\sim 280\ \Omega$, which is close to the value of the resistance between the two ohmic contacts to the substrate. Although the differential resistances at $V=0$ for different elements of the photodiode matrix can differ considerably [in the limits $(0.3-1)\times 10^6\ \Omega$] for large forward currents the values of $R_0=\Delta V/\Delta I$ nearly coincide. Thus, the resistance $R_0$ found from Fig. 3a is the resistance of the substrate. The voltage drop across $R_0$ alters the dependence $I(V)$, but has a noticeable effect only in the region $V>0.2$ V. In order to move the experimental points in Fig. 2 for voltages somewhat greater than (on the order of) 0.1 V to the straight line, the series resistance should be roughly two orders of magnitude greater than $R_0=280\ \Omega$. It must be assumed that the investigated diode structure contains a layer whose resistance greatly exceeds the substrate resistance, and that its conductivity (i.e., that of this layer) grows considerably at large forward currents.

The observed features of the $I-V$ characteristic are explainable if for the investigated diodes we posit an energy-level diagram corresponding to a $n^+-p^--p$ structure similar to the one formed under ion implantation in $p$-HgCdTe (Ref. 12) (see Fig. 3b). As is well known,[3] the conductivity of $p$-HgMnTe (and likewise $p$-HgCdTe) is mainly determined by mercury vacancies, which act as acceptors. As a result of ion etching, there arises on the surface of the crystal an excess of Hg atoms, which by diffusing into the interior of the crystal fill the Hg vacancies, thereby compensating for the acceptors. In the surface layer the concentration of excess Hg atoms is large, which leads to strong overcompensation of acceptors and a change in the conductivity type of the material ($n^+$ layer, $1-2\ \mu$m). Although the concentration of diffused Hg atoms decreases monotonically with distance from the surface, the Fermi level in some interval of variation of the Hg concentration is fixed at the level of the residual acceptors ($\sim 10^{15}\ \mathrm{cm}^{-3}$ in HgCdTe, Ref. 12). As a result, an extended ($5-10\ \mu$m) layer of $p$-type conductivity with hole density less than in the substrate ($p^-$ layer) is formed. Under a forward bias the current is governed by recombination in the $n^+-p^-$ junction; however, with increase of the bias, part of the applied voltage drops across the high-resistance $p^-$ layer and growth of the current with the voltage ''falls behind'' the dependence $I\sim\exp(eV/2kT)$ (the segment $V=0.1-0.2$ V in Fig. 2). The injection of electrons into the $p^-$ layer occurs at the same time as the recombination in the $n^+-p^-$ junction (diffusion current of minority carriers), which can decrease its resistance (if the diffusion length of the electrons is comparable with or greater than the thickness of the $p^-$ layer). If the lifetime of the carriers $\tau$ is known, the diffusion length of the electrons can be found as $L_n=(D_n\tau)^{1/2}$, where $D_n$ is the diffusion of the electrons, which is related to their mobility $\mu_n$ by the relation $eD_n/kT=\mu_n$ (for a nondegenerate semiconductor, which the $p^-$ layer is). Assuming $\mu_n=10^5\ \mathrm{cm}^2/(V\cdot\mathrm{s})$ at $T=80$ K, we obtain $D_n\simeq 700\ \mathrm{cm}^2/\mathrm{s}$ and $L_n=(6-7)\times 10^{-2}$ cm. Since $L_n$ greatly exceeds the thickness of the $p^-$ layer, its conductivity under electron injection is modulated considerably, i.e., the resistance is decreases. The electrons injected into the $p$ substrate cannot substantially alter its conductivity since its resistivity is relatively small.

## 5. REVERSE CURRENTS

One possible mechanism of charge transport under reverse bias of the $p-n$ junction is generation in the space charge region. If the levels involved in generation (such as recombination under a reverse bias) are located near the middle of the band gap, the reverse current in an asymmetric $p-n$ junction[10,11] is

$$I_{\mathrm{gen}}=A\frac{en_i d\ \sqrt{E_g/2-eV}-\sqrt{E_g/2}}{\tau\sqrt{\varphi_0-eV}}, \tag{2}$$

where the last factor takes into account the nonuniformity of generation in the space charge region. As can be seen, the current calculated for low bias voltages is less than the measured current by roughly an order of magnitude, and for large biases—it is less than the current by several orders of magnitude. The character of the dependence $I(V)$ also differs qualitatively: the calculated current increases with $V$ sublinearly, and the measured current increases superlinearly. There is reason to assume that the reverse current of the investigated $p-n$ junctions is governed by tunneling processes. The expression for the reverse current for an abrupt $p-n$ junction, in which the maximum intensity of the electric field is equal to $2(\varphi_0-eV)/ed$, can be represented for interband tunneling in the form[13]

$$I_{\mathrm{tun}}=\gamma A\frac{e\sqrt{2m_r}}{2\pi^2\hbar^2E_g^{1/2}d_0}(\varphi_0-eV)^{3/2}\times\exp\left[-\frac{4}{3\hbar(N_a-N_d)^{1/2}}\sqrt{m_r\varepsilon\varepsilon_0}\,\frac{E_g^{3/2}}{\sqrt{\varphi_0-eV}}\right], \tag{3}$$

where $m_r=m_e^*m_h^*/(m_e+m_h^*)$ is the reduced mass of the electron and the hole, and $\gamma$ is a constant which does not depend on $V$ and is introduced as a fitting parameter to compare with experiment since expression (3) assumes that the electric field in the $p-n$ junction is uniform and that its intensity is equal to the maximum intensity of the field in an asymmetric junction $2(\varphi_0-eV)/e^2d$ [for $\gamma=1$ formula (3) overestimates the current]. In Fig. 4a the measured and calculated dependences of the current on the voltage are plotted in coordinates which, according to Eq. (3), should give a straight line. It can be seen that Eq. (3) describes the experimental dependence of $I(V)$ only for relatively low reverse biases $|V|<0.3$ V (to ''match'' the calculated and experimental dependences it is necessary to set $\gamma=0.32$). For larger voltages the experimental points deviate noticeably upward from the obtained values of the calculated reverse current. This may be due to impact ionization of the atoms of the crystalline lattice, which leads to a multiplication of charge carriers. Of course, after tunneling an electron, like the newly formed hole, finds itself in a region where it is under the influence of a strong electric field and can therefore participate in avalanche processes. This conjecture is confirmed by the curves plotted in Fig. 4b, which plot the voltage dependence of the photocurrent $I_{\mathrm{ph}}$ arising under infrared irradia-

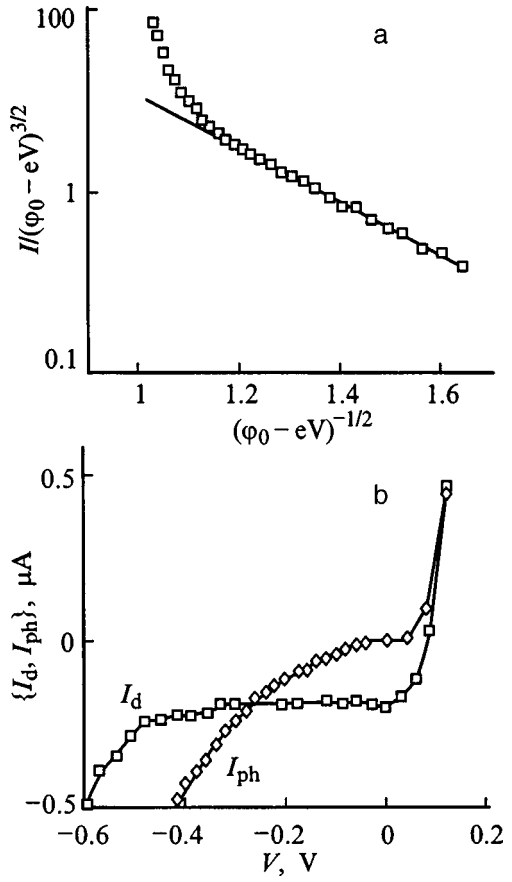


FIG. 4. a — Comparison of calculation based on formula (3) with the experimental voltage dependence of the reverse current. b — voltage dependence of the dark current $I_d$ and the photocurrent $I_{ph}$.

tion of the investigated $p-n$ junction. In the diode structure under consideration, the photocurrent is formed mainly as a result of an accumulation of carriers generated in the $n^+$ layer (its thickness clearly is much less than the diffusion length of the holes), and therefore the photocurrent does not depend on the voltage when $|V|<0.3$ V. However, as soon as the reverse bias exceeds 0.3 V, the photocurrent begins to grow quite abruptly, which is direct evidence of impact ionization. At almost the same reverse bias the experimental points in Fig. 4a begin to deviate from the dependence described by formula (3).

It follows from the data plotted in Fig. 4b that the no-load voltage for irradiation of the diode ($V_{oc}$) is equal to 0.09 V. Such a value of $V_{oc}$ is impossible for a diode with nondegenerate $p^-$ and $n$ regions since $V_{oc}$ cannot exceed the contact potential $\varphi_0/e$, and $\varphi_0<E_g=0.09$ eV. On the other hand, $V_{oc}=0.09$ V is completely realistic for the investigated $n^+-p^--p$ structure which has a $n^+$ region. Since the space charge region in such a structure is located in the high-resistance $p^-$ region, we should set $N_a-N_d\simeq10^{15}\,\mathrm{cm}^{-3}$ in formula (3). However, in order that the slope of the line in Fig. 4a coincide with the experimental dependence it is necessary to set $N_a-N_d\simeq(1-2)\times10^{16}\,\mathrm{cm}^{-3}$. The contradiction is eliminated if we adopt the model according to which tunneling in diodes occurs with the participation of deep impurity levels (defects).[3,5] In this case, in formula (3) we must replace $E_g$ by a smaller quantity, and then to preserve the necessary slope of the rectilinear segment in Fig. 4a we must correspondingly decrease $N_a-N_d$. For example, if tunneling takes place through levels located in the middle of the band gap, then we must decrease $N_a-N_d$ by a factor of $2^3=8$. Of course, this change in $N_a-N_d$ must also be taken into account in the expressions for the generation–recombination currents (1) and (2). However, this does not introduce any major changes in the estimates for the lifetime and the diffusion length of the carriers since we must replace $\varphi_0\simeq E_g$ by $\sim3$ times this value as the width of the space charge region is increased.

## 6. CONCLUSIONS

Ion etching of $p$-$Hg_{1-x}Mn_xTe$ has been used to obtain $n^+-p^--n$ structures with stable rectifying characteristics. The forward current of the investigated diodes is governed by carrier recombination in the space charge region. Its voltage dependence for large $V$ includes a voltage drop on the $p^-$ layer, whose resistance decreases with growth of the current. The reverse current for low bias voltages is produced by tunneling processes, and it grows further as a result of the avalanche processes as the bias voltage is raised.

*)E-mail: oe-dpt@phys.chsu.cv.ua

[1] J. K. Furduna, J. Vac. Sci. Technol. **21**(1), 220 (1982).
[2] R. Tribonlet, Semicond. Sci. Technol. **5**, 1073 (1990).
[3] A. Rogalski, Infrared Phys. **31**, 117 (1991).
[4] P. Becla, J. Vac. Sci. Technol. A **4**, 2014 (1986).
[5] E. Janik and G. Karczewski, Acta Phys. Pol. A **73**, 439 (1998).
[6] P. Brogowski, H. Mucha, and J. Piotrowski, Phys. Status Solidi A **114**, K37 (1989).
[7] L. A. Kosyachenko, I. M. Rarenko, O. O. Bodnaruk, Sun Veĭgua, and Khu Zheng Ksiong, *Scientific Bulletin of Chernovtsy University* [in Russian], Ruta, Chernovtsy (1998), No. 40, p. 59.
[8] O. A. Bodnaruk, I. N. Gorbatyuk, S. É. Ostapov, I. M. Rarenko, V. P. Shafranyuk, and S. V. Nichiĭ, Neorg. Mater. **31**, 1347 (1995).
[9] Sun Weiguo, L. A. Kosyachenko, and I. M. Rarenko, J. Vac. Sci. Technol. A **15**(4), 2202 (1997).
[10] C. Sah, R. Noice, and W. Shockley, Proc. IRE **45**, 1228 (1957).
[11] L. A. Kosyachenko, M. M. Slyotov, D. V. Galchenkov, and L. I. Voyevidko, Ukr. Fiz. Zh. **39**, 1001 (1994).
[12] L. O. Bubulac, J. Cryst. Growth **86**, 723 (1988).
[13] S. M. Sze, *Physics of Semiconductor Devices* (Wiley, New York, 1969).

Translated by Paul F. Schippnick

# Drag current for ionization of impurities by an electromagnetic wave in a semiconductor superlattice

M. V. Vyazovskiĭ and G. A. Syrodoev

*Volgograd State Pedagogical University, 400013 Volgograd, Russia*
(Submitted September 14, 1998; accepted for publication April 26, 1999)
Fiz. Tekh. Poluprovodn. **33**, 1443–1446 (December 1999)

The drag current for ionization of a shallow impurity by a strong electromagnetic wave in a semiconductor superlattice is found. It is shown that at low temperatures, when it is possible to ignore the equilibrium carrier density, the dependence of the drag current on the intensity of the electromagnetic wave is nonlinear and it oscillates with growth of the intensity of the electromagnetic field. These oscillations are a consequence of the many-photon character of absorption of the electromagnetic wave by the impurities and also of nonparabolicity of the energy spectrum of the superlattice. A comparison is made of the contributions to the drag current from the anisotropic part of the impurity ionization probability and from its isotropic part, with allowance for modification of the distribution function by the electromagnetic wave. It is found that for $\hbar\omega \ll \Delta$ ($\Delta$ is the width of the conduction miniband) the main contribution to the drag current comes from the isotropic part of the ionization probability. © *1999 American Institute of Physics.* [S1063-7826(99)00912-6]

The drag current of conduction electrons in semiconductor superlattices (SL's) due to electromagnetic waves (EMW's) (both monochromatic and solitary) has been considered in a number of papers.[1–4] In Refs. 5–7 the drag current in a homogeneous semiconductor was found for two- and three-photon interband absorption of light. Ionization of impurities in the superlattice, on the other hand, and its contribution to the drag current have been examined in less detail. In Ref. 8 the drag current caused by electromagnetic solitons in a superlattice was found with allowance for only the anisotropic nature of the probability for ionization of the impurity for one-photon absorption. As we will show below, when the conditions $a/\lambda \ll 1$, $eEd/\hbar\omega \geqslant 1$, and $\hbar\omega/\Delta \ll 1$ are satisfied ($a$ is the Bohr radius of the impurity, $\lambda$ is the wavelength of the electromagnetic wave, $E$ is the electric field of the electromagnetic wave, $\omega$ is the frequency of the electromagnetic wave, $\Delta$ is the width of the conduction miniband, and $e$ is the electron charge), the anisotropic part of the ionization probability of the impurity can be disregarded, but the variation of the electron distribution function $f(\mathbf{p},t)$ caused by the field of the electromagnetic wave should be taken into account. If the conditions $eEd \ll \Delta$ and $\hbar/\tau_p \ll \Delta$ are satisfied ($\tau_p$ is the mean relaxation time of the electrons), it is possible to solve the problem in the semiclassical and one-miniband approximation. We write the kinetic equation for the distribution function in the form

$$\frac{\partial f}{\partial t} + \mathbf{F}\cdot\frac{\partial f}{\partial \mathbf{p}} = -\frac{f-f_0}{\tau_p} + N_0 G(\mathbf{p}) - \frac{f}{\tau_r}, \tag{1}$$

where $\mathbf{F} = -e\mathbf{E} - (e/c)\,\mathbf{v}\times\mathbf{H}$, $f_0(\mathbf{p})$ is the equilibrium distribution function, $N_0$ is the impurity concentration, and $\tau_r$ is the mean electron and hole recombination time.

$$G(\mathbf{p}) = \lim_{T\to\infty}\frac{d}{dT}\left|\int_{-\infty}^{T}\langle \mathbf{k}|\hat{H}'|n\rangle e^{-i\omega_{\mathbf{k},t}t}dt\right|^2 \tag{2}$$

is the transition (ionization) probability per unit time,

$$\hat{H} = \varepsilon\left(\hat{\mathbf{p}} + \frac{e}{c}\mathbf{A}(t)\right) - \varepsilon(\hat{\mathbf{p}}) \tag{3}$$

is the effective Hamiltonian for the interaction of the electromagnetic wave with an electron in the conduction miniband,

$$\varepsilon(\mathbf{p}) = \frac{p_\perp^2}{2m} + \frac{\Delta}{2}\left(1 - \cos\left(\frac{p_z d}{\hbar}\right)\right) \tag{4}$$

is the electron energy in this band, $\mathbf{p} = \hbar\mathbf{k}$ is the quasimomentum, $\hat{\mathbf{p}} = -i\hbar\nabla$, $\mathbf{A}(t)$ is the vector potential of the electromagnetic wave, $\hbar\omega_{\mathbf{k},n} = \varepsilon(\mathbf{p}) + I_n$, $I_n$ is the ionization energy of the $n$th impurity level, and $|\mathbf{k}\rangle$ and $|n\rangle$ are the wave functions of the electron in the conduction miniband and in the bound state on the impurity.

In the kinetic equation we have dropped the term with the spatial derivative since the mean velocity of the electrons is significantly less than the velocity of the electromagnetic wave, and the mean free path is significantly less than the wavelength of the electromagnetic wave. We find the solution of Eq. (1) by the method of characteristics[9]

$$f(\mathbf{p},t) = \frac{1}{\tau_p}\int_{-\infty}^{t} e^{-\frac{t-t'}{\tau}} f_0(\mathbf{p}'(t',\mathbf{p},t))dt' + N_0\int_{-\infty}^{t} G(\mathbf{p}'(t';\mathbf{p},t)) e^{-\frac{t-t'}{\tau}} dt', \tag{5}$$

where $\tau = \tau_p\tau_r/\tau_p + \tau_r$, and $\mathbf{p}'$ is found by solving the equation of motion

$$\frac{d\mathbf{p}'}{dt'} = \mathbf{F}(\mathbf{v}',t') \tag{6}$$

 

with the initial condition $t'=t$, $\mathbf{p}'=\mathbf{p}$. Let a monochromatic electromagnetic wave propagate perpendicular to the superlattice axis: $A_z=A_0\cos(\omega t-kx)$, $\mathbf{E}=-1/c\ \partial\mathbf{A}/\partial t$, $\mathbf{H}=\mathrm{curl}\,\mathbf{A}$. Solving the equation of motion (6) and taking into account that $v/c\ll 1$, we find

$$p_z'=p_z-\frac{e}{c}(A_z(t')-A_z(t)),$$

$$p_x'=p_x-\frac{\Delta\sqrt{\kappa}}{2c}\left[2\sin^2\left\{\frac{1}{2}\frac{ed}{\hbar c}(A_z(t')-A_z(t))\right\}\times\cos\frac{p_z'd}{\hbar}-\sin\left\{\frac{ed}{\hbar c}(A_z(t')-A_z(t))\right\}\sin\frac{p_z'd}{\hbar}\right] \quad (7)$$

($\kappa$ is the high-frequency dielectric constant).

For $G(\mathbf{p})$ in the dipole approximation in the case of a hydrogen-like impurity (in the ground state $|0\rangle$) we obtain the expression

$$G(\mathbf{p})=\frac{32\pi^2a^3\Delta^2}{V(1+a^2\mathbf{k}^2)^4\hbar^2}\times\left[\cos^2\frac{p_zd}{\hbar}\sum_{s=1}^{\infty}J_{2s}^2(b)\,\delta(\omega_{\mathbf{k},0}-2s\omega)+\sin^2\frac{p_zd}{\hbar}\sum_{s=0}^{\infty}J_{2s+1}^2(b)\,\delta(\omega_{\mathbf{k},0}-(2s+1)\omega)\right]. \quad (8)$$

Here $J_s(b)$ is the Bessel function of $s$th order, $b=(ed/\hbar c)A_0=eE_0d/\hbar\omega$, and $V$ is the volume of the crystal. From this expression it can be seen that the terms of the sums correspond to contributions from multiphoton ionization.[1)] In an exact calculation of the transition probability (not in the dipole approximation) the denominator of the first factor of this expression contains terms of order $a/\lambda$, which can be ignored when $a/\lambda\ll 1$. The drag current is

$$j_x=-\frac{e}{m}\int f(\mathbf{p},t)p_x\,d^3p, \quad (9)$$

where $m$ is the effective mass along the $x$ axis. Substituting the distribution function (5) in Eq. (9) and interchanging the order of integration and transforming to new variables in accordance with Eqs. (7) and then averaging the expression so obtained over one period of the electromagnetic wave, we find the constant component of the drag current

$$\overline{j_x}=\left(1-J_0^2(b)-2\sum_{s=1}^{\infty}\frac{J_s^2(b)}{1+(s\omega\tau)^2}\right)(j_0^{(1)}+j_0^{(2)}\Phi_1(b)), \quad (10)$$

where

$$\Phi_1(b)=\left(\sum_{s=0}^{\infty}J_{2s+1}(b)\Theta(\eta_s)\int_{-x_s}^{x_s}\frac{\sin^2 x\,\cos x\,dx}{\left[1+\left(\frac{2ma^2}{\hbar^2}\right)\left((2s+1)\hbar\omega-\frac{\Delta}{2}(1-\cos x)-I\right)+\frac{a^2}{d^2}x^2\right]^4}+\sum_{s=1}^{\infty}J_{2s}^2(b)\Theta(\eta_s')\int_{-x_s'}^{x_s'}\frac{\cos^3 x\,dx}{\left[1+\left(\frac{2ma^2}{\hbar^2}\right)\left(2s\hbar\omega-\frac{\Delta}{2}(1-\cos x)-I\right)+\frac{a^2}{d^2}x^2\right]^4}\right), \quad (11)$$

where

$$x_s=2\arcsin\sqrt{\xi_s}\,\Theta(1-\xi_s)+\pi\Theta(\xi_s-1),$$

$$x_s'=2\arcsin\sqrt{\xi_s'}\,\Theta(1-\xi_s')+\pi\Theta(\xi_s'-1),$$

$$\xi_s=\frac{(2s+1)\hbar\omega-I}{\Delta},\quad \xi_s'=\frac{2s\hbar\omega-I}{\Delta},$$

$$\eta_s=\left\{\frac{(2s+1)\hbar\omega}{I}\right\}-1,\quad \eta_s'=\left\{\frac{2s\hbar\omega}{I}\right\}-1,$$

the braces $\{\}$ denote the integer part of the number, $\Theta(x)$ is the unit step function [$\Theta(x)=1$ for $x\geqslant 0$, $\Theta(x)=0$ for $x<0$], $I$ is the ionization energy of the ground state,

$$j_0^{(1)}=-en_0\frac{\Delta\sqrt{\kappa}}{2mc}\frac{I_1(\beta)}{I_0(\beta)}\frac{\tau}{\tau_p}, \quad (12)$$

$\beta=\Delta/k_0T$, $n_0$ is the electron density in the conduction miniband in the equilibrium state, $I_n(\beta)$ is the Bessel function of $n$th order with imaginary argument, and

$$j_0^{(2)} = -\frac{4\pi^2 e N_0 \Delta^3 a^3 \tau \sqrt{\kappa}}{cd\hbar^3}. \tag{13}$$

In the limiting case $b \to 0$ we find

$$\overline{j_x} = \left[ j_0^{(1)} + j_0^{(2)} \frac{I}{\Delta} \left( \frac{eE_0 d}{\hbar\omega} \right)^2 \sqrt{\frac{\hbar\omega - I}{\Delta}} \right] \frac{\omega^2 \tau^2}{1+\omega^2\tau^2} \left( \frac{eE_0 d}{\hbar\omega} \right)^2. \tag{14}$$

If the inequality

$$j_0^{(1)} \gg j_0^{(2)} \frac{I}{\Delta} \sqrt{\frac{\hbar\omega - I}{\Delta}} \left( \frac{eE_0 d}{\hbar\omega} \right)^2 \tag{15}$$

is satisfied, then the drag current $\overline{j_x} \sim E_0^2$ (the drag current depends linearly on the intensity of the electromagnetic wave). This is a well-known result of the linear theory of the photoelectric effect (Ref. 12).[2] The inequality (15) is satisfied at those temperatures at which the impurities are almost completely ionized (for shallow impurities this temperature is on the order of 100 K). If the inequality

$$j_0^{(1)} \ll j_0^{(2)} \frac{I}{\Delta} \sqrt{\frac{\hbar\omega - I}{\Delta}} \left( \frac{eE_0 d}{\hbar\omega} \right)^2 \tag{16}$$

is satisfied, then the drag current $\overline{j_x} \sim E_0^4$; i.e., the drag current is proportional to the square of the intensity of the electromagnetic wave. This is explained by the two-step nature of the formation of the current: by ionization of the impurity and subsequent entrainment of carriers by the electromagnetic wave. As can be seen from Eq. (10), the first factor of this expression oscillates with growth of $b$, the factor multiplying $j_0^{(2)}$ also has an oscillatory character. For $b \leqslant 1$, $\omega\tau \gg 1$ and $\hbar\omega > I$, $\hbar\omega - I \ll \Delta$ it is possible to give the following estimate for the drag current:

$$\overline{j_x} \approx \frac{2}{3} j_0^{(2)} (1 - J_0^2(b)) \frac{J_1^2(b)}{[\omega\tau]^2} \frac{I}{\Delta} \varphi(b), \tag{17}$$

where $\varphi(b) = \Sigma_{s=1}^{\infty} J_s^2(b)/s^2 = 1/\omega\tau^2 \, (2/\pi \int_0^{\pi/2} t^2 J_0(2b\cos t)\, dt - \pi/12\, J_0^2(b))$ (Ref. 11). We thus see that the current at first grows, and then decreases with growth of $b$, vanishing at $b = b_1$, where $b_1$ is the first zero of $J_1(b)$. Such behavior of the drag current is explained by the fact that acted on by the electric field of the electromagnetic wave the electron traverses the entire conduction miniband and its velocity near the top of the miniband vanishes (correspondingly, the magnetic component of the Lorentz force also vanishes there). In the case $b \geqslant 1$, when the contribution from multiphoton transitions grows, the drag current can be found by numerical integration. Figure 1 shows two graphs of the variation of $\overline{j_x}/j_0^{(2)}$ as a function of $b = eE_0 d/\hbar\omega$ for $\omega\tau = 10$ and $a/d = 1$, $a = 10^{-7}$ cm, $\Delta = 10^{-1}$ eV, $I = 10^{-2}$ eV, $\hbar\omega = (1 - 0.5) \times 10^{-2}$ eV, constructed by numerical integration. From these graphs of the variation of the drag current it can be seen that the current oscillates with growth of $b$. Such behavior of the drag current is explained, first of all, by the multiphoton character of ionization of the impurity by the electromagnetic wave.[13,14] The multiphoton character of absorption under these conditions must be taken into account for intensities $J \geqslant 10^7$ W/cm$^2$. But in addition to multiphoton absorption, the first factor in expression (10), which oscillates and asymptotically approaches unity as $b \to \infty$, also contributes to the drag current. These oscillations are caused by the nonparabolic character of the electron energy spectrum of the superlattice (the electron velocity decreases at the top of the miniband). Thus, the oscillations of the drag current are caused by multiphoton absorption of the electromagnetic wave and by the nonparabolic character of the electron energy spectrum of the superlattice. The decrease in the amplitude of the oscillations of the drag current with growth of the field of the electromagnetic wave represents, in our opinion, a phenomenon related to the above-mentioned stabilizationof an atom in a laser field.[8] To compare the contributions to the drag current from the anisotropic part of the ionization

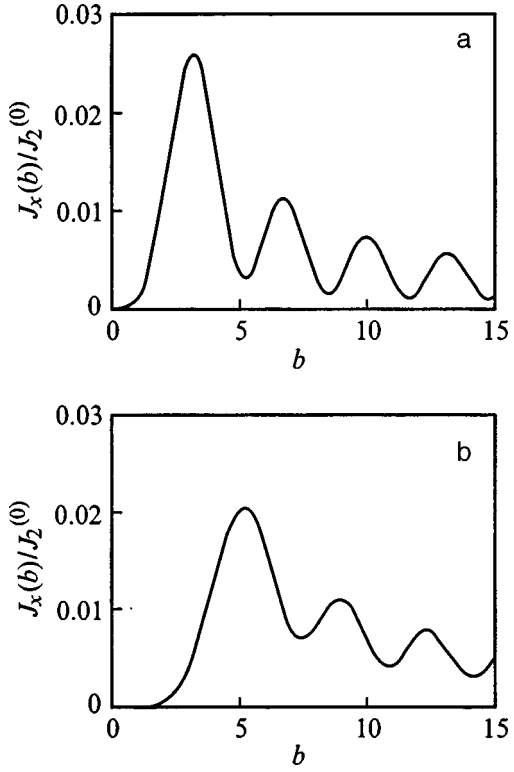


FIG. 1. Dependence of the drag current $j_x j_0^{(2)}$ on $b = eE_0 d/\hbar\omega$ for $\hbar\omega = I = 0.01\,eV$ (a) and $\hbar\omega = 0.5I = 0.005\,eV$ (b).

probability and from its isotropic part (with subsequent modification of the distribution function by the electromagnetic wave), we find the anisotropic part of the ionization probability $G_{\mathbf{k}}^{a}$ and the drag current

$$\overline{j_x^a} = eN_0\tau\frac{V}{(2\pi)^3}\int G_{\mathbf{k}}^{a} v_x d^3k = -\frac{8eN_0\tau\Delta^2 aq}{mId}\Phi_2(b),$$

where

$$\Phi_2(b) = \left( \sum_{s=0}^{\infty} J_{2s+1}(b)\Theta(\eta_s) \int_{-x_s}^{x_s} \frac{(2s+1)\left((2s+1)\dfrac{\hbar\omega}{I} - 1 - \dfrac{\Delta}{I}\sin^2\dfrac{x}{2}\right)\sin^2 x\, dx}{\left[1+\left(\dfrac{2ma^2}{\hbar^2}\right)\left((2s+1)\hbar\omega - \dfrac{\Delta}{2}(1-\cos x) - I\right) + \dfrac{a^2}{d^2}x^2\right]^5} \right.$$

$$\left. + \sum_{s=1}^{\infty} J_{2s}^2(b)\Theta(\eta_s') \int_{-x_s'}^{x_s'} \frac{2s\left(2s\dfrac{\hbar\omega}{I} - 1 - \dfrac{\Delta}{I}\sin^2\dfrac{x}{2}\right)\cos^2 x\, dx}{\left[1+\left(\dfrac{2ma^2}{\hbar^2}\right)\left(2s\hbar\omega - \dfrac{\Delta}{2}(1-\cos x) - I\right) + \dfrac{a^2}{d^2}x^2\right]^5} \right).$$

The ratio of currents $\overline{j_x^a}/j_x = 4/\pi^2\ (\hbar\omega/\Delta)\,\Phi_2(b)/\Phi_1(b)$ (here we have taken into account that $\hbar^2/2ma^2 = I$). We see that for $\hbar\omega \ll \Delta$ this ratio can become significantly less than unity. Numerical integration for $b = 1$ (5) and $\hbar\omega = I$ and the above values of the remaining parameters gives $\Phi_2(b)/\Phi_1(b) = 2.3(4.1)$, and for $\hbar\omega = 0.5I$ and the same values of the parameter $b$ $\Phi_2(b)/\Phi_1(b) = 3(4.4)$. Thus, in this case the main contribution to the drag current comes from the isotropic part of the ionization probability and subsequent entrainment of the electrons by the field of the electromagnetic wave.

[1)] Integrating $G(\mathbf{p})$ over all the remaining states of the continuum, we obtain the total probability of the transition $G$. Numerical integration shows that $G$, while oscillating, decreases with growth of $\mathbf{E}$, tending to a constant value (this phenomenon in the context of photoionization of atoms is called stabilization of atoms in a laser field).[10,11]

[2)] In the case of a homogeneous semiconductor $\beta = \Delta/k_0T \gg 1$ and $I_1(\beta)/I_0(\beta) = 1$.


[1] A. A. Ignatov, Fiz. Tverd. Tela (Leningrad) **22**(11), 3319 (1980) [Sov. Phys. Solid State **22**, 1942 (1980)].
[2] É. M. Épshteĭn, Fiz. Tekh. Poluprovodn. **14**(12), 2422 (1980) [Sov. Phys. Semicond. **14**, 1438 (1980)].
[3] É. M. Épshteĭn, Izv. Vuzov. Radiofizika **24**(4), 514 (1981).
[4] É. M. Épshteĭn, Fiz. Tekh. Poluprovodn. **16**(12), 2231 (1982) [Sov. Phys. Semicond. **16**, 1445 (1982)].
[5] N. A. Brynskiĭ and S. A. Sagdullaeva, Fiz. Tekh. Poluprovodn. **12**(4), 798 (1978) [Sov. Phys. Semicond. **12**, 467 (1978)].
[6] S. D. Ganichev, S. A. Emel'yanov, E. L. Ivchenko, E. Yu. Perlin, Ya. V. Terent'ev, A. V. Fedorov, and I. D. Yaroshetskiĭ, Zh. Éksp. Teor. Fiz. **91**(4), 1233 (1986) [Sov. Phys. JETP **64**, 729 (1986)].
[7] R. Ya. Rasulov, Fiz. Tekh. Poluprovodn. **22**(11), 2077 (1988) [Sov. Phys. Semicond. **22**, 1316 (1988)].
[8] S. V. Kryuchkov, Fiz. Tekh. Poluprovodn. **25**(4), 740 (1991) [Sov. Phys. Semicond. **25**, 446 (1991)].
[9] F. G. Bass, A. A. Bulgakov, and A. P. Tetervov, *High-Frequency Properties of Semiconductors with Superlattices* [in Russian], Nauka, Moscow, 1989.
[10] N. B. Delone and V. P. Kraĭnov, Usp. Fiz. Nauk **165**(11), 1295 (1995) [Phys. Usp. **36**, 805 (1995)].
[11] M. V. Fedorov, Usp. Fiz. Nauk **169**(1), 66 (1999).
[12] K. Seeger, *Semiconductor Physics* (Springer-Verlag, Berlin, 1974).
[13] L. V. Keldysh, Zh. Éksp. Teor. Fiz. **47**(5), 1945 (1964) [Sov. Phys. JETP **20**, 1307 (1964)].
[14] M. V. Fedorov, *Electron in a Strong Light Field* [in Russian], Nauka, Moscow, 1991.


Translated by Paul F. Schippnick

# Position of the Fermi level on an indium arsenide surface treated in sulfur vapor

N. N. Bezryadin, E. A. Tatokhin, A. V. Budanov, and A. V. Linnik

*Voronezh State Technological Academy, 394017 Voronezh, Russia*

I. N. Arsent'ev

*A. F. Ioffe Physicotechnical Institute, Russian Academy of Sciences, 194021 St. Petersburg, Russia*
(Submitted April 8, 1999; accepted for publication June 11, 1999)
Fiz. Tekh. Poluprovodn. **33**, 1447–1449 (December 1999)

The characteristic features of the formation kinetics of $In_2S_3$ layers on indium arsenide substrates by heterovalent substitution are studied. The activation energies of two steps in this process are separated and determined. The variation of the position of the Fermi level on an InAs surface during treatment in sulfur vapor is recorded by measuring the thermodynamic work function using the Kelvin probe method. © *1999 American Institute of Physics.* [S1063-7826(99)01012-1]

The use of III–V semiconductor compounds to create field-effect devices is restricted by the high density of surface electron states existing in these compounds. A technology for passivating the surfaces of III–V compounds in chalcogen-containing media has found application in lowering the density of surface electron states and, thus, in depinning the Fermi level.[1] In this paper we report the results of an experimental study of the passivation of an InAs surface as a result of treatment in sulfur vapor.

When GaAs and InAs substrates are annealed in selenium or sulfur vapor in a quasiclosed vessel, thin films of III–VI compounds are known to form on their surface as a result of heterovalent substitution of the chalcogen for arsenic atoms in the anion sublattice of the substrates.[2,3] On the basis of the results in Ref. 4, the sulfur vapor pressure was held at $P \simeq 10^{-2}$ Pa, the substrate temperature ($T_s$) was varied in the range 453–523 K, and the treatment time was varied from 10 to 45 min. The thickness ($d$) of the $In_2S_3$ layers formed was determined ellipsometrically using the method described in Ref. 5 and monitored according to the images of cross sections obtained in a scanning electron microscope (SEM).

The values of the thickness of the $In_2S_3$ films formed with various values of $T_s$ at a fixed time in the process were obtained during the measurements. The slopes of the different segments of the plot of $d^2 = f(1/kT_s)$ constructed in semilogarithmic coordinates (Fig. 1), which describes the temperature dependence of the rate of formation of the layer,[6] were used to calculate the activation energies corresponding to the two stages of the process. They are $E_1 = 3.29$ eV/atom for segment *AB* and $E_2 = 1.47$ eV/atom for segment *BC*. The error in the estimation of the activation energies was determined by the errors in both the direct measurements of the substrate temperature and the ellipsometric measurements and amounted to about 10%.

Since the concentrations of the reactants can be considered unrestricted and independent of the variation of $T_s$ in the initial stages of the treatment and since the arsenic evolved during the heterovalent substitution reaction in the vapor phase can be assumed to be removed from the reaction zone (its influence on the layer formation kinetics is insignificant), the heterovalent substitution reaction is presumably an equilibrium process. Therefore, segment *AB* of the $\ln(d^2)$-versus-$1/kT$ curve can be described by the van't Hoff equation. Since the amount of indium sulfide is proportional to the thickness of the layer, the equilibrium constant of the reaction can be expressed in terms of the thickness of the layer $d$. We can then write the van't Hoff equation in the form

$$\ln(d^2) = \ln A - \frac{\Delta H}{kT}, \tag{1}$$

where $A$ is a coefficient, which depends on the concentra-

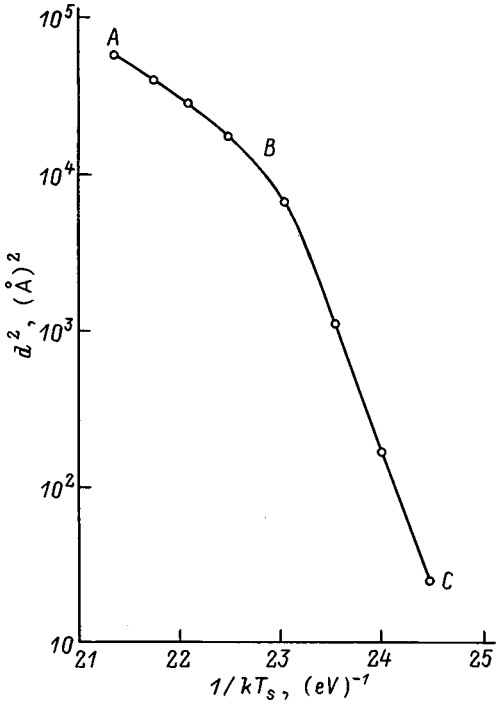


FIG. 1. Dependence of the square of the thickness of an $In_2S_3$ layer formed on an InAs surface on substrate temperature.

 

tions of the reactants and the rate constants of the forward and reverse reactions at infinite temperature, and $\Delta H$ is the heat of reaction.

The equation of the heterovalent substitution reaction in the InAs–S system has the form

$$3S_2 + 4InAs \rightarrow 2In_2S_3 + As_4, \quad (2)$$

i.e., the heat of the heterovalent reaction should correspond to the difference between the enthalpies of indium sulfide and indium arsenide (the enthalpies of elemental sulfur and arsenic are equal to zero), which amounts to 3.49 eV/atom in the present case and is close to the value of the activation energy $E_1$ corresponding to segment *AB* of the experimental plot of $d^2 = f(1/kT)$ (Fig. 1). This allows us to conclude that the heterovalent substitution process is determined by the endothermic chemical reaction described by Eq. (2) in the initial stages of the process.

Reactions in heterogeneous systems generally take place in several consecutive steps, and the rate of the overall reaction is determined by the rate of the slowest step.[7] In the case of our heterovalent substitution process, at least two steps are possible:

a) the heterovalent substitution reaction on the ⟨InAs solid phase ⟩/⟨gaseous sulfur⟩ interface (segment *AB* in Fig. 1);

b) the diffusion of sulfur through the $In_2S_3$ layer.

In fact, as was shown in Ref. 3, when the thickness of the $In_2S_3$ layer exceeds 500 Å, the diffusion step determines the rate of the total heterovalent substitution reactions; i.e., segment *BC* of the plot of $d^2 = f(1/kT)$ (Fig. 1) can be described by the Arrhenius equation expressing the temperature dependence of the diffusion. The value of the activation energy obtained from the slope of this segment $E_2 = 1.47$ eV/atom is close to the value of the activation energy for the diffusion of sulfur in $In_2S_3$ reported in Ref. 8 ($E = 1.51$ eV/atom).

It is known from the data in Ref. 9 that the Fermi level is pinned at 0.13 eV above the bottom of the conduction band in InAs. Depinning of the Fermi level was demonstrated on the basis of an analysis of the capacitance-voltage ($C-V$) characteristics of Al/$In_2S_3$/InAs MIS heterostructures in Ref. 3. However, at thicknesses of the $In_2S_3$ layer less than 300 Å the high level of the leakage currents precludes recording the $C-V$ characteristics of heterostructures of this type. We have therefore measured the variation of the Fermi level by the Kelvin-probe method. The external contact potential difference was measured using the device described in Ref. 10 with a vibrating platinum electrode. The result of each measurement was the difference between the work functions of platinum and the sample surface.

It follows from an analysis of the dependence of the thermodynamic work function of the sample ($\chi$) on the thickness $d$ of the $In_2S_3$ layer formed (Fig. 2) that without treatment in sulfur vapor, i.e., in the case of a substrate which has undergone only chemical polishing, the Fermi level on the InAs surface is, in fact, pinned at 0.13 eV above the bottom of the conduction band. The course of the $\chi(d)$ curve in the initial treatment stages corresponding to the formation of films with a thickness up to 100 Å corresponds to variation

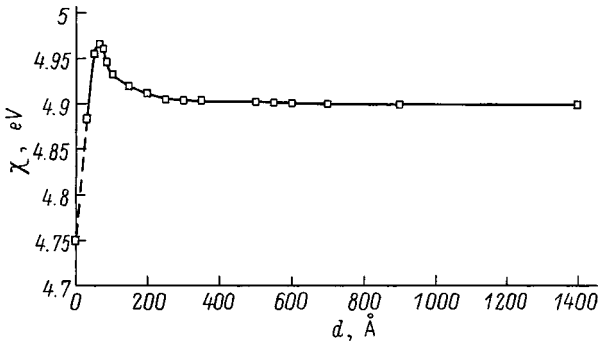


FIG. 2. Dependence of the thermodynamic work function $\chi$ on the thickness of the $In_2S_3$ layer.

of the Fermi level from 0.13 eV above the bottom of the conduction at $d \simeq 0$ nm to values roughly 0.08 eV below the bottom of the conduction band at thicknesses greater than 50 Å. Since the latter value corresponds to the position of the Fermi level in the bulk of the indium arsenide used (IMÉa-3 InAs) at 300 K, it may be concluded that the Fermi level on the InAs surface is depinned as a result of treatment in sulfur vapor. The subsequent increase in the thickness of the $In_2S_3$ layer formed is accompanied by gradual lowering of the measured thermodynamic work function, and at $d \simeq (30-40)$ nm it reaches 4.9 eV. This decrease in the thermodynamic work function is associated with an increase in the degree of screening of the electric field by charges in the indium sulfide layer formed. At layer thicknesses exceeding the generalized screening length[11,12] the measured values of $\chi$ correspond to the thermodynamic work function of $In_2S_3$.

Thus, the brief treatments of an indium arsenide surface in sulfur vapor during times corresponding to the formation of an indium sulfide layer with a thickness much smaller than the Debye screening length and with the corresponding tunneling transparency (the latter was analyzed by comparing the current-voltage characteristics of metal/InAs contacts before and after the treatment), which were studied in the present work, and prolonged treatments accompanied by the formation of a semi-insulating $In_2S_3$ layer, which provides for the formation of MIS heterostructures based on the $In_2S_3$–InAs system,[3] lead to depinning of the Fermi level on the indium arsenide surface, which is attributable to lowering of the density of surface electron states within the known models.[13] We note that the growth kinetics undergo a change with the passage of time from kinetics limited by the reaction rate on the interface to kinetics limited by diffusion of the reaction components through the $In_2S_3$ layer. This should lead to a change in the concentration gradient of the reaction components across the thickness of the $In_2S_3$ layer and, accordingly, to a change in the sulfur and arsenic concentrations at the interface. Since the Fermi level on the InAs surface is depinned regardless of the thickness of the sulfide layer, it can be assumed that the surface electron states in InAs are not associated with an excess or deficiency of sulfur or arsenic at the interface. It was shown in Ref. 14 that after the treatment of gallium arsenide in various chalcogens, a layer with a crystallographic orientation differing from the orientation of the GaAs substrate forms on its surface. This is

attributed to reconstruction of the gallium arsenide surface during its interaction with the chalcogen. Such a state of the GaAs surface is stabilized by a pseudomorphic layer of the $Ga_2Se_3$ type formed during the treatment in the chalcogen. As a result, the interface remains reconstructed even after it is formed. Thus, the escape of electron states from the band gap to the GaAs surface is explained by analogy with the familiar mechanism for a GaAs surface cleaved in a vacuum.[13,14] Similar reconstruction was observed in the case of the treatment of indium arsenide in sulfur vapor when $In_2S_3$/InAs heterostructures were obtained by heterovalent substitution.[4] Thus, the depinning of the Fermi level and the corresponding lowering of the electron density of states on an indium arsenide surface treated in sulfur can also be associated with rearrangement of the atoms on its surface relative to their configuration in the bulk of the crystal during the interaction with sulfur.

[1] V. N. Bessolov and M. V. Lebedev, Fiz. Tekh. Poluprovodn. **32**, 1281 (1998) [Semiconductors **32**, 1141 (1998)].
[2] B. S. Sysoev, V. D. Strygin, E. I. Chursina, and G. I. Kotov, Izv. Akad. Nauk SSSR, Neorg. Mater. **27**, 1583 (1991).
[3] B. I. Sysoev, N. N. Bezryadin, A. V. Budanov, and Yu. K. Shlyk, Mikroelektronika **19**, 591 (1990).
[4] B. I. Sysoev, N. N. Bezryadin, A. V. Budanov, T. V. Prokopova, and B. L. Agapov, Neorg. Mater. **31**(7), 891 (1995).
[5] S. A. Titov, V. D. Linnik, and B. I. Sysoev, Prib. Tekh. Éksp., No. 4, 125 (1994).
[6] P. Barret, *Cinétique Hétérogène* [Gauthier Villars, Paris, 1973; Mir, Moscow, 1976].
[7] B. F. Ormont, *Introduction to the Physical Chemistry and Crystal Chemistry of Semiconductors* [in Russian], Vysshkaya Shkola, Moscow, 1973.
[8] N. Kh. Abrikosov, V. F. Bankina, L. V. Poretskaya, E. V. Skudnova, and S. N. Chizhevskaya, *Semiconductor Chalcogenides and Alloys Based on Them* [in Russian], Nauka, Moscow, 1975.
[9] H. U. Baier, L. Koenders, and W. Monch, Solid State Commun. **58**, 327 (1986).
[10] I. Yu. Butusov, V. V. Kryachko, I. E. Lobov, and V. V. Kotov, Élektron. Prom., No. 4–5, 111 (1994).
[11] B. I. Sysoev and V. F. Synorov, Fiz. Tekh. Poluprovodn. **6**, 1856 (1972) [Sov. Phys. Semicond. **6**, 1603 (1973)].
[12] V. E. Lashkarev, Izv. Akad. Nauk SSSR, Ser. Fiz. **16**(2), 203 (1952).
[13] W. E. Spicer, J. Lindau, P. Pianetta, P. W. Chye, and C. M. Garner, Thin Solid Films **56**, 1 (1979).
[14] B. I. Sysoev, N. N. Bezryadin, G. I. Kotovr, B. L. Agapov, and V. D. Strygin, Fiz. Tekh. Poluprovodn. **29**, 24 (1995) [Semiconductors **29**, 12 (1995)].

Translated by P. Shelnitz

## LOW-DIMENSIONAL SYSTEMS

# Effect of anisotropy of band structure on optical gain in spherical quantum dots based on PbS and PbSe

A. D. Andreev

*A. F. Ioffe Physicotechnical Institute, Russian Academy of Sciences, 194021 St. Petersburg, Russia*

A. A. Lipovskiĭ

*St. Petersburg State Technical University, 195251 St. Petersburg, Russia*

(Submitted January 11, 1999; accepted for publication May 20, 1999)
Fiz. Tekh. Poluprovodn. **33**, 1450–1455 (December 1999)

Results of an experimental and theoretical study of the optical absorption spectra of spherical quantum dots based on PbS and PbSe are presented. A rigorous theoretical analysis of the energy spectra and optical transitions is performed within the framework of the four-band $\mathbf{k}\cdot\mathbf{p}$ approximation with full account of the effect of anisotropy of the band structure. It is shown that strong anisotropy of the band structure of PbS and PbSe leads to the appearance of optical transitions that are forbidden in the isotropic approximation. These transitions were detected in the optical absorption spectra of the investigated quantum dots. © *1999 American Institute of Physics.* [S1063-7826(99)01112-6]

### 1. INTRODUCTION

Glass matrices with semiconductor quantum dots are of interest in connection with the fundamental properties of low-dimensional structures and the effect of quantum limitation on optical transitions. The dependence of the energy of these transitions on size makes it possible to ''tune'' such glasses to the wavelength of a source under the condition that this wavelength exceed the band gap for the bulk semiconductor. In the case of a narrow size distribution of the ensemble of quantum dots, resonant tuning is possible. The main body of studies of quantum dots formed in glass matrices has been devoted to quantum dots based on wideband II–VI semiconductors whose band gap corresponds to the visible range of wavelengths.[1] Recently, glasses with quantum dots based on narrow-band semiconductors of the type IV–VI have been synthesized, and the energy structure of these quantum dots has been modeled.[2–5] In particular,[3] the energy spectra and matrix elements responsible for optical transitions in PbS and PbSe quantum dots were calculated. These calculations used the isotropic approximation, and anisotropy effects were taken into account only within the framework of first-order perturbation theory. However, as is shown in the present work, anisotropy of the band structure has a substantial effect on the optical properties of quantum dots based on lead sulfide and lead selenide and, consequently, it should be taken into account in a full treatment.

In this paper we present results of a theoretical and experimental study of the energy structure and optical transitions in spherical quantum dots based on PbS and PbSe. We show that taking the effect of anisotropy fully into account provides a satisfactory description of the experimental optical absorption spectra and allows one to identify the observed optical transitions, including transitions which are not described in the isotropic approximation or within the framework of the model proposed earlier in Ref. 3.

### 2. SYNTHESIS AND EXPERIMENTAL STUDY OF QUANTUM DOTS

To form semiconductor quantum dots in the phase decay of a supersaturated solid solution, we used a recently developed $P_2O_5$–$Na_2O$–ZnO–$AlF_3$–$Ga_2O_3$ glass[4,5] doped with PbS or PbSe. The glass was synthesized at 1100 °C, with glass-transition temperature $T_G \sim 380$ °C. We used the technique of synthesis from a feedstock. After synthesis and quenching at room temperature, the glass samples had a slightly yellowish color, typical of lead-containing glasses. Heat treatment of the synthesized glasses at 390–400 °C lead to a change in their coloration to a color ranging from brown to black, depending the duration and temperature of the anneal. X-ray diffraction studies and transmission electron microscopy of the annealed glass samples demonstrated the existence of spherical PbS and PbSe quantum dots with dimensions varying from 2 to 15 nm for various conditions of heat treatment. The estimated width of the size distribution of these microcrystals for the sample with the narrowest size distribution of the quantum dots was ~5–7 %. Such a narrow size distribution of the quantum dots in a glass matrix is quite unique, with the exception of the glass samples with quantum dots described in Ref. 2. Usually distributions of such width can be obtained in the formation of quantum dots by chemical synthesis.[6] The optical absorption spectra of annealed samples of glass matrices with PbS or PbSe quantum dots were measured in the wavelength range 350–3500 nm at room temperature and at liquid-helium temperature. The

 

narrow size distribution of the quantum dots made it possible to observe the optical absorption peaks corresponding to various quantum transitions even at room temperature. The measurements at liquid-helium temperature demonstrated the presence of narrow optical absorption peaks corresponding to the narrow size distribution of the quantum dots. Increasing the duration of the anneal led to a shift of the optical absorption spectra of the samples from spectra of unannealed glasses (glasses that had not been subjected to heat treatment) to spectra characteristic of bulk crystals of PbS and PbSe.

### 3. MODELING AND COMPARISON WITH EXPERIMENT

To calculate the energy levels and wave functions of the electrons and holes in a spherical quantum dot, we used the four-band $\mathbf{k}\cdot\mathbf{p}$ model, which takes into account the anisotropy of the dependence of the energy on the quasimomentum and quite accurately describes the energy band structure near the $L$ point.[7,8] This model takes into account the interaction of the valence band and the conduction band, which is important for a calculation of the energy levels of spherical quantum dots in the isotropic approximation.[3] We used the $\mathbf{k}\cdot\mathbf{p}$ expansion near the $L$ point since the minimum of the conduction band and the maximum of the valence band of PbS and PbSe are found at the $L$ point of $k$ space. The effective Hamiltonian $\hat{H}$ of the four-band $\mathbf{k}\cdot\mathbf{p}$ model can be represented in the form $H=H_{isotr}+H_{an}$, where the first term corresponds to the isotropic part,[3] and the second term describes the anisotropy of the dispersion relation of the energy versus the momentum $E(\mathbf{k})$:

$$\hat{H}_{isotr}=\begin{pmatrix} \frac{E_g}{2}+\frac{\hbar^2k^2}{2m^-} & \frac{\hbar}{m_0}P\sigma\mathbf{k} \\ \frac{\hbar}{m_0}P\sigma\mathbf{k} & -\frac{E_g}{2}-\frac{\hbar^2k^2}{2m^+} \end{pmatrix}, \tag{1}$$

where

$$P^2=(2P_t^2+P_l^2)/3, \tag{2}$$

$$\frac{1}{m^\pm}=\frac{1}{3}\left(\frac{2}{m_t^\pm}+\frac{1}{m_l^\pm}\right); \tag{3}$$

$\sigma$ is the Pauli matrix, $\mathbf{k}=-i\,\partial/\partial\mathbf{r}$, $E_g$ is the band gap of the bulk semiconductors, $m_t^\pm$ and $m_l^{pm}$ are the transverse and longitudinal effective masses for the electrons $(+)$ or holes $(-)$, $P_t$ and $P_l$ are the transverse and longitudinal matrix elements of the momentum between the Bloch wave functions of the conduction band edge and the valence band (analogous to the Kane matrix element for III–V semiconductors), $z$ is the coordinate in the $\langle 111\rangle$ direction, and $m_0$ is the free electron mass. The anisotropic part of the Hamiltonian has the form

$$\hat{\mathbf{H}}_0^{an}=\begin{pmatrix} \frac{\hbar^2}{2m_{lt}^-}(k^2-3k_z^2) & 0 & \frac{\hbar}{m_0}(P_l-P)k_z & \frac{\hbar}{m_0}(P_t-P)k_- \\ 0 & \frac{\hbar^2}{2m_{lt}^-}(k^2-3k_z^2) & \frac{\hbar}{m_0}(P_t-P)k_+ & -\frac{\hbar}{m_0}(P_l-P)k_z \\ \frac{\hbar}{m_0}(P_l-P)k_z & \frac{\hbar}{m_0}(P_t-P)k_- & -\frac{\hbar^2}{2m_{lt}^+}(k^2-3k_z^2) & 0 \\ \frac{\hbar}{m_0}(P_t-P)k_+ & -\frac{\hbar}{m_0}(P_l-P)k_z & 0 & -\frac{\hbar^2}{2m_{lt}^+}(k^2-3k_z^2) \end{pmatrix}, \tag{4}$$

where $k_\pm=k_x\pm ik_g$, $p_t=P_t-P$, $p_l=P_l-P$, and

$$\frac{1}{m_{lt}^\pm}=\frac{1}{3}\left(\frac{1}{m_t^\pm}-\frac{1}{m_l^\pm}\right). \tag{5}$$

The wave functions of the carriers localized at the spherical quantum dots, i.e., the eigenfunctions of the Hamiltonian $\hat{H}$, can be represented in the form of a superposition of eigenfunctions $|\alpha\rangle$ of the Hamiltonian $H_{isotr}$ corresponding to the isotropic band structure

$$\Psi=\sum_\alpha C_\alpha|\alpha\rangle, \tag{6}$$

the sum is over all states $\alpha$ of the isotropic Hamiltonian with allowance for degeneracy. In this case, for the calculations it is sufficient to restrict the sum (6) to a finite number of terms that ensures the necessary accuracy in the relevant energy interval. In the present work we included 42 terms in the sum (6), which provided a relative accuracy better than 0.1% in the calculation of the energy levels and matrix elements of the optical transition.

In the isotropic model each state $|\alpha\rangle$ of the electrons and holes in a spherical quantum dot is characterized by four quantum numbers:[3] $|\alpha\rangle=|j,m,\nu,n_r\rangle$, where $j$ and $m$ are the total angular momentum and its projection, $n_r$ is the radial quantum number, and $\nu$ denotes the parity of the state. The coefficients $C_\alpha$ in expansion (6) and the energy levels in the

spherical quantum dot can be found numerically as the solution of the problem of eigenvalues and eigenvectors of the matrix $H_{\alpha\beta}=\delta_{\alpha\beta}E_\alpha+\langle\alpha|\hat{H}_{an}|\beta\rangle$, where $\hat{H}_{isotr}|\alpha\rangle=E_\alpha|\alpha\rangle$ and $E_\alpha$ is the energy of the state $\alpha$.

The wave functions of the isotropic part of the Hamiltonian $H_{isotr}$ can be found in a way that is analogous to how it is done in the solution of the problem of the motion of a Dirac electron in a central field[3,9,10]

$$|\gamma,\alpha\rangle=A^{\gamma}_{l\nu\bar{m}}\begin{pmatrix} B_1^{l\nu\bar{m}}\cdot f^{\gamma}_{l\nu}(r) & \mathbf{Y}^{\bar{m}}_{l}(\theta,\varphi) \\ B_2^{l\nu\bar{m}}\cdot f^{\gamma}_{l\nu}(r) & \mathbf{Y}^{\bar{m}+1}_{l+\nu}(\theta,\varphi) \\ B_3^{l\nu\bar{m}}\cdot g^{\gamma}_{l\nu}(r) & \mathbf{Y}^{\bar{m}}_{l}(\theta,\varphi) \\ B_4^{l\nu\bar{m}}\cdot g^{\gamma}_{l\nu}(f) & \mathbf{Y}^{\bar{m}+1}_{l+\nu}(\theta,\varphi) \end{pmatrix}. \tag{7}$$

Here $\gamma=e,h$ denotes the type of carrier (electron or hole, respectively); the integers $l$ and $\bar{m}$ have been introduced to simplify the form of the formulas and are expressed in terms of the quantum numbers $j$, $m$, $\nu$: $l=j-\nu/2$, $\bar{m}=m-1/2$; $A_{l\nu\bar{m}}$ is a normalization factor; $B_i^{l\nu m}$ are constants; $\mathbf{Y}^m_l(\theta,\varphi)$ are the spherical harmonics,[10] $f^{\gamma}_{l\nu}(r)$ and $g^{\gamma}_{l\nu}(r)$ are the radial components, which are expressed in terms of the Bessel function

$$f(r)=\frac{1}{\sqrt{kr}}J_{l+1/2}(kr)+\frac{b}{\sqrt{\lambda r}}I_{l+1/2}(\lambda r), \tag{8}$$

$$g(r)=\frac{\nu c}{\sqrt{kr}}J_{l+\nu+1/2}(kr)+\frac{db}{\sqrt{\lambda r}}I_{l+\nu+1/2}(\lambda r). \tag{9}$$

In expressions (8) and (9), the indices $\gamma, l, \bar{m}$ have been dropped; here it is understood that the quantities $k$, $\lambda$, $b$, $c$, and $d$ depend on the quantum numbers and on the energy of the corresponding level $E^{\gamma}_{l\nu\bar{m}}\equiv E$ in the isotropic model

$$b=-\sqrt{\frac{\lambda}{k}}\frac{\lambda_{l+1/2}(ka)}{I_{l+1/2}(\lambda a)},\quad c=\frac{\frac{E_g}{2}-E+\frac{\hbar^2k^2}{2m_{\pm}}}{\frac{\hbar P}{m}k},$$

$$d=\frac{\frac{E_g}{2}-E-\frac{\hbar^2\lambda^2}{2m_{\pm}}}{\frac{\hbar P}{m}\lambda}. \tag{10}$$

Taking the boundary conditions into account: $\Psi_0=0$ for $|\mathbf{r}|=1$, and also the explicit form of the wave functions (7)–(9), the energy levels in the quantum dot can be found within the framework of the isotropic model numerically as the solution of the corresponding dispersion relation (3).

The matrix elements $\langle\alpha|\hat{H}_{an}|\beta\rangle$ are calculated analytically using the Wigner–Eckart theorem[9] and the explicit expressions (7)–(9) for the wave functions $|\alpha\rangle$. The matrix elements for the optical transition between the levels $i$ and $f$ in the quantum dot are calculated using the formula

$$M_{i\to f}=\sum_{\alpha,\beta}[C^{(i)}_{\alpha}]^*C^{(f)}_{\beta}M_{\alpha\beta}, \tag{11}$$

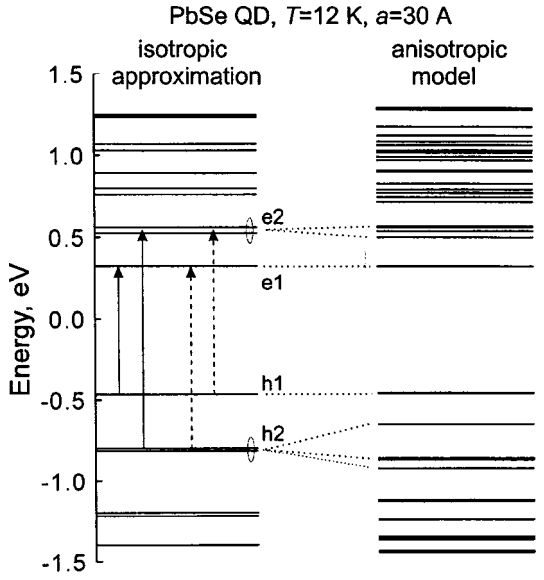


FIG. 1. Energy levels of spherical PbSe quantum dots, calculated in the isotropic approximation (horizontal lines on the left) and with full account for anisotropy of the band structure (horizontal lines on the right). The solid and dashed vertical lines, respectively, denote allowed and forbidden transitions in the isotropic approximation. The dotted lines, running from the levels on the left to the levels on the right, show isotropic states which give the main contribution to level formation in a spherical quantum dot. Radius of the quantum dot $a=40$ Å, temperature $T=12$ K.

where the matrix elements $M_{\alpha\beta}$ for the optical transition between isotropic states $\alpha$ and $\beta$ are calculated analytically. Finally, the square of the matrix element for a given polarization is calculated according to formula (1), and then averaged over directions of the polarization vector, where the distribution over orientations of the spherical quantum dots in the glass matrix is assumed to be uniform. Note also that in the case in which the sum is restricted to degenerate (or quasi-degenerate) states with given energy in Eq. (6), we obtain the first-order perturbation theory result obtained in Ref. 3. However, this approximation is inapplicable due to strong mixing of isotropic states with different energies, leading to a nonzero optical matrix element for transitions forbidden in the isotropic model.

Figure 1 shows the energy levels of a spherical quantum well, calculated in the isotropic and anisotropic models. The ground-state energies in both models are very close. The anisotropy of the band structure shifts the ground-state energy insignificantly since we used a set of averaged band parameters for the isotropic model in the calculations:[3] $P^2=(2P_t^2+P_l^2)/3$ and $3/m^{\pm}=2/m_t^{\pm}+1/m_l^{\pm}$. The ground state of the electrons and holes (the levels $e1$, $h1$; see Fig. 1) consists of states with $j=1/2$, $\nu=\theta$, $n_r=1$; the higher levels $e2$ and $h2$ consist of states with $j=1/2$, $3/2$, $\nu=-\theta$, $n_r=1$ (where $\theta=1$ for the electrons and $\theta=-1$ for the holes). In the isotropic approximation we have the following selection rules for the direct optical transitions: $\Delta j=0,\pm1$; $\Delta m=0$, $\pm1$; $\nu_c\nu_h=-1$. Consequently, all optical transitions between the groups of levels $e1\leftrightarrow h2$ and $e2\leftrightarrow h1$ (the dashed lines in Fig. 1) in the isotropic model are forbidden by parity. Analogous conclusions are valid for higher levels. However, the situation changes markedly in a full account of anisot-

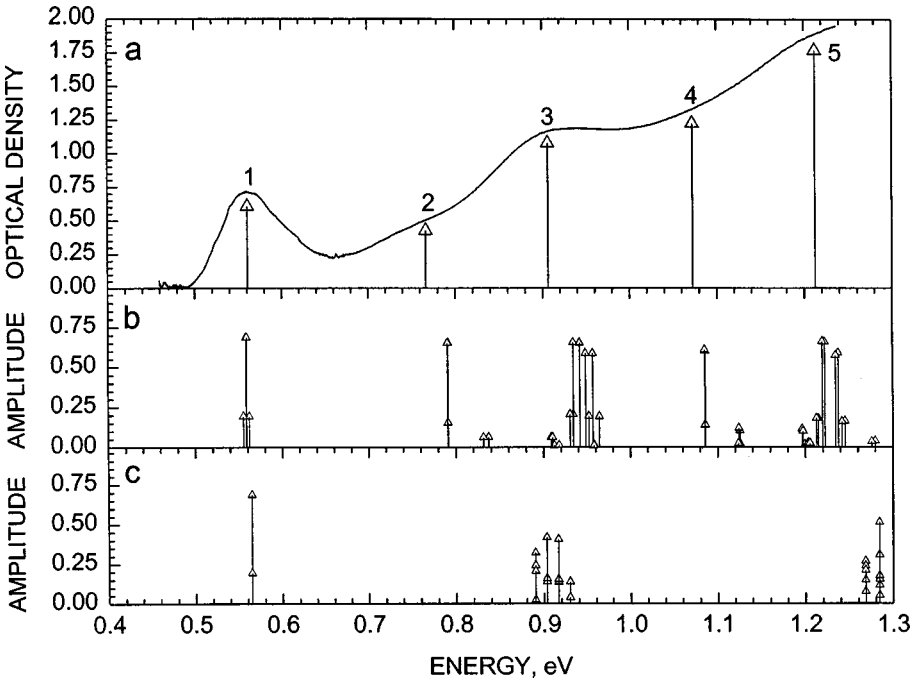


FIG. 2. a — Measured optical absorption spectrum of spherical PbSe quantum dots in a glass matrix; arrows indicate transition energies obtained from an analysis of the second derivative; b — squares of the modulus of the matrix elements of the optical transitions, averaged over orientations of the quantum dots and calculated with full account of anisotropy of the band structure; c — the same for the isotropic model. Radius of the spherical quantum dot $a=40$ Å; the calculations used the following parameters: $E_g(T=12\ \mathrm{K})=0.166$ eV, $P_t^2/m=1.7$ eV, $2P_l^2/m=3.0$ eV, $m/m_t^-=4.3$, $m/m_l^-=3.1$, $m/m_t^+=8.7$, $m/m_l^+=3.3$.

ropy of the dependence of the energy on the quasimomentum $E(\mathbf{k})$. The influence of anisotropy reduces to two effects. First, the energy levels shift and split (see Fig. 1). Second, strong mixing of the various isotropic states takes place. Consequently, transitions that were forbidden in the isotropic approximation are now allowed as a result of this mixing. These transitions are observed in the measured absorption spectra (see Figs. 2 and 3). Thus, anisotropy of the band structure exerts a substantial influence on the optical absorption spectra of spherical quantum dots based on PbS and PbSe.

Figure 2a shows the measured absorption spectrum of PbS quantum dots at $T=12$ K. Analysis of the second derivative of this spectrum allowed us to distinguish five absorption bands corresponding to optical transitions or groups of transitions. The isotropic model and the model used in Ref. 3 can predict only three transitions (see Fig. 2c) since the remaining transitions are forbidden within the framework of these simple approaches. The calculations performed by us with full allowance for the anisotropy of the band structure show that the amplitudes of the ''forbidden'' transitions (peaks *2* and *4* in Fig. 2) are of the same order of magnitude as the amplitudes of the ''allowed'' transitions. The energies of transitions *1–5*, calculated in the anisotropic model, are found to be in good agreement with experiment (see Fig. 2). The difference between the theoretical results and experi-

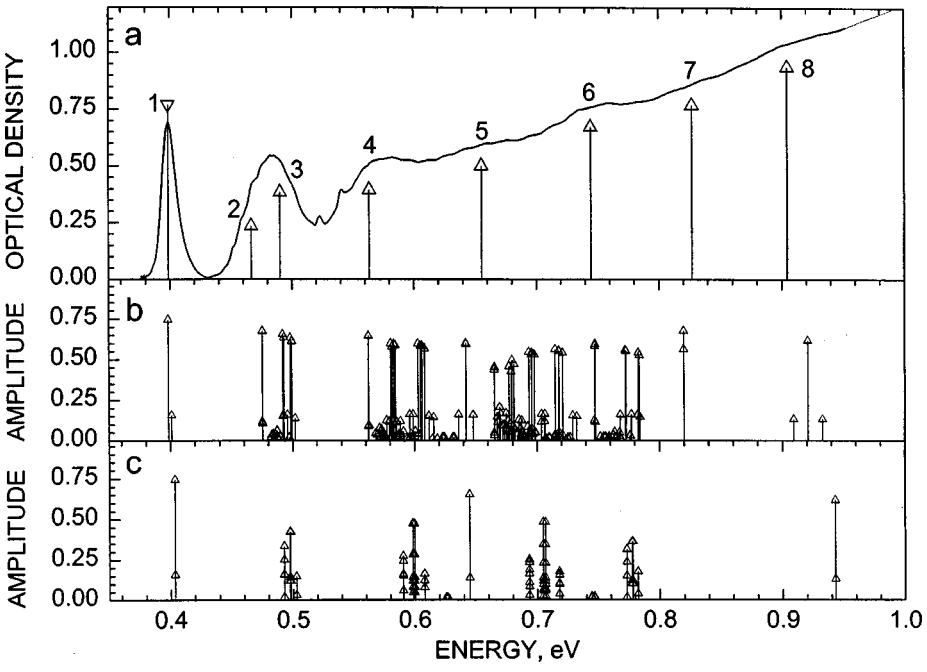


FIG. 3. The same as in Fig. 2, but for PbS quantum dots of radius $a=73$ Å. The calculations used the following parameters: $E_g(T=12\ \mathrm{K})=0.299$ eV, $2P_t^2/m=1.4$ eV, $2P_l^2/m=3.3$ eV, $m/m_t^-=1.3$, $m/m_l^-=2.9$, $m/m_t^+=1.6$, $m/m_l^+=2.9$.

ment do not exceed 20–30 meV, which may be due to the influence of such factors as a deviation from sphericity of the quantum dots, the influence of a boundary, and also some uncertainty in the values of the band parameters. To estimate the influence of nonsphericity of a quantum dot on the absorption spectra, we calculated the shift of the energy levels in a quantum dot in the case where its shape is an ellipsoid of revolution with semi-axes $a_1$ and $a_2$. We have accordingly used perturbation-theory methods analogous to those described by Migdal.[11] The shift of the energy levels associated with nonsphericity can be represented in the form $\Delta F_\alpha = \delta_\alpha E_\alpha D_\alpha$, where $\delta_\alpha = 2(a_1 - a_2)/(a_1 + a_2)$ is a measure of the ''nonsphericity'' of a quantum dot, and $D_\alpha$ are numerical coefficients which depend on the quantum numbers $\alpha = (j, m, \nu, n_r)$. On the basis of transmission-electron-microscope measurements we estimated the value of $\delta_\alpha$ to be $\leqslant 0.05$. The corresponding shift of the energy levels turned out to be no greater than 5 and 12 meV for PbS and PbSe quantum dots, respectively. Consequently, the influence of a deviation of the shape of the quantum dots from spherical on the absorption spectra is much less than the influence of anisotropy of the band structure, and it cannot be the reason for the appearance of additional transitions in the optical absorption spectra.

The measured absorption spectrum of spherical PbS quantum dots is shown in Fig. 3a. For PbS the first forbidden transition *2* is closer in energy to the second allowed transition *3* (Fig. 3) than in the case of quantum dots based on PbSe (Fig. 2). This is because of the weaker anisotropy of the energy band structure of PbS in comparison with PbSe. The rather wide peak *4* and the corresponding plateau consist of one ''purely'' forbidden transition with a lower energy and several allowed transitions shifted in energy in comparison with the results of the isotropic model. Note that the isotropic model gives a transition energy corresponding to peak *4* that is 40 meV greater than the experimental value. The features of the absorption spectrum *5–8* in the higher energy region cannot be interpreted unambiguously for the reasons mentioned above. However, we may conclude that the weak peak *7* most likely corresponds to a forbidden transition while peak *8* corresponds to an allowed transition and features *5* and *6* of the absorption spectrum consists of forbidden and allowed transitions. Thus, we were able to observe and interpret up to four optical transitions in spherical quantum dots based on lead sulfide.

## 4. CONCLUSIONS

We have developed a theoretical model which takes full account of anisotropy of the band structure. This model adequately describes the measured optical absorption spectra of spherical quantum dots based on lead sulfide and lead selenide and allowed us to identify up to five quantum transitions for PbSe and up to four quantum transitions for PbS quantum dots. We have shown that optical transitions that are forbidden in the isotropic model turn out to be allowed for a strict account of anisotropy. Because of the narrow size distribution of the quantum dots, these ''forbidden'' transitions, which are associated with anisotropy, can be observed experimentally in the optical absorption spectra of spherical PbS and PbSe quantum dots formed in a new phosphate glass.

This work was supported in part by the program Physics of Solid-State Nanostructures (A. A. Lipovskiĭ and A. D. Andreev) and also by a grant from the Russian Fund for for Fundamental Research (Grant No. 99-02-16750) (A. D. Andreev).

[1] D. J. Norris, A. L. Efros, M. Rosen, and M. G. Bawendi, Phys. Rev. B **53**, 16347 (1996).
[2] N. F. Borrelli and D. W. Smith, J. Non-Cryst. Solids **80**, 25 (1994).
[3] I. Kang and F. W. Wise, J. Opt. Soc. Am. B **14**, 1632 (1997).
[4] A. A. Lipovskii, E. V. Kolobkova, and V. D. Petrikov, Electron. Lett. **33**, 101 (1997).
[5] A. Lipovskii, E. Kolobkova, V. Petrikova, I. Kang, A. Olkhovets, T. Krauss, M. Thomas, J. Silcox, F. Wise, Q. Shen, and S. Kycia, Appl. Phys. Lett. **71**, 3406 (1997).
[6] C. B. Murray, D. J. Norris, and M. G. Bawendi, J. Am. Ceram. Soc. **115**, 8706 (1993).
[7] D. L. Mitchel and R. F. Wallis, Phys. Rev. **151**, 581 (1966).
[8] J. O. Dimmock, *The Physics of Semimetals and Narrow-Gap Semiconductors*, edited by D. L. Carter and R. T. Bates (Oxford, Pergamon Press, 1971).
[9] L. D. Landau and E. M. Lifshitz, *Quantum Mechanics: Non-Relativistic Theory*, 3rd ed. [Pergamon Press, Oxford, 1977; Nauka, Moscow, 1974].
[10] V. B. Berestetskiĭ, E. M. Lifshitz, and L. P. Pitaevskiĭ, *Relativistic Quantum Theory* [Pergamon Press, Oxford, 1971; Pt. 1 and 2, Nauka, Moscow, 1968, 1971].
[11] A. B. Migdal, *Qualitative Methods in Quantum Theory* (W. A. Benjamin, Massachusetts, 1977).

Translated by Paul F. Schippnick

# Superradiance in semiconductors

S. V. Zaĭtsev, L. A. Graham, and D. L. Huffaker

*Microelectronics Research Center, University of Texas at Austin, Bldg. 160, Burnet Rd, Austin, TX 78758, USA*

N. Yu. Gordeev, V. I. Kopchatov, L. Ya. Karachinsky, I. I. Novikov, and P. S. Kop'ev

*A.F. Ioffe Physicotechnical Institute, Russian Academy of Sciences, 194021 St. Petersburg, Russia*
(Submitted June 21, 1999; accepted for publication June 24, 1999)
Fiz. Tekh. Poluprovodn. **33**, 1456–1461 (December 1999)

The dependences of the characteristic superradiance time in quantum well InGaAs/GaAs laser heterostructures on the pump current, temperature, and cross sections of the active region are studied by analyzing electroluminescence spectra. The number of dipoles involved in forming a superradiant pulse is estimated using elementary equations from the theory of superradiance in two-level systems. A mechanism is proposed for superradiance in semiconductors. © *1999 American Institute of Physics.* [S1063-7826(99)01212-0]

## INTRODUCTION

In the last two years, there has been a rapidly growing interest in resonant interactions of nonequilibrium charge carriers in semiconductor heterostructures through the combined electromagnetic field of their recombination radiation.[1–4] This type of effect, which results from the small distance between the radiating centers compared to the wavelength of the radiation, has been known for a long time and has been well studied theoretically and experimentally in the case of solid state lasers,[5–7] where it is known as Dicke superradiance. The effect essentially reduces to spontaneous phasing of closely spaced dipoles and their merging into a combined ''macrodipole,'' whose radiant efficiency is proportional to the square of the number of constituent elementary dipoles. This leads to an avalanche growth in the radiant intensity and, accordingly, to production of a short optical burst.[8]

The role of this kind of interaction among the carriers in semiconductor materials has long been underrated, although the density of electron-hole pairs in these materials is usually far higher than the density of impurity centers in solid state lasers. Increasing the number of dipoles involved in a resonance sharply reduces the duration of the resulting pulse and the durations appropriate to semiconductor materials lie far beyond the time resolution of modern photodetectors. In addition, these pulses occur randomly, which makes them difficult to detect. Nevertheless, they have been observed under certain conditions using streak cameras in a single-photon counting mode.[9,10] Unfortunately, the complex experimental conditions have precluded a unique interpretation.

A specially created optical autocorrelator[11] has been used in some preliminary experiments in 1993–1994 and superradiant pulses were observed in an injection laser, both above and below the lasing threshold.[12,13] Appropriate measurements of the pulse parameters were made. The sensitivity and resolution of the apparatus, however, were not adequate for measuring the emission parameters below the lasing threshold. Nevertheless, the results have been used to explain the previously studied behavior of Q-switched injection lasers.[14] Vasil'ev[3] obtained the same results independently.

All of the above experiments were conducted at room temperature. Under these conditions, the homogeneous broadening of the line emitted as a result of the collective resonance, which was described in detail in 1971 for solid-state lasers,[7] is concealed by the thermal distribution of the carriers in a semiconductor. At $T=77$ K, however, the picture is completely different. The distinctive electroluminescence spectral profile of quantum-well heterostructures was first noted by Eliseev and Akimova,[15] but it was not interpreted correctly. We have made a detailed investigation[16] of the emission spectra of quantum wells at 77 K under conditions such that the spectral distortions are eliminated and theoretically justified identifying the spectra with the homogeneous line broadening profile under superradiance conditions. The major parameters of the corresponding superradiance pulses were also estimated in that paper.

In this paper we present results from a study of the dependences of the superradiance parameters on the temperature, pump current density, and size of the emitting region. An attempt is also made to estimate the minimum absolute pump current for generation of superradiant pulses.

## MODEL

The resonant interaction of closely spaced dipoles with the electromagnetic field of their own radiation is known to cause a change from the ordinary time dependence

$$I(t)\sim N\mathrm{e}^{-t/\tau} \tag{1}$$

of the radiant intensity, i.e., an exponential decrease in the intensity with time ($t$), to the dependence given by Dicke,[8] with an intensity rise followed by a relatively rapid fall (Fig. 1),

 

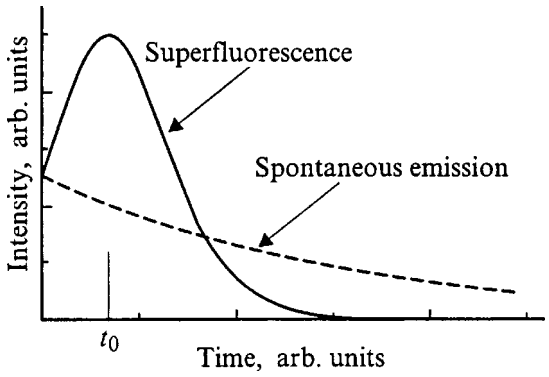


FIG. 1. Characteristic time dependence of the superradiance intensity. The dashed curve is the ordinary time dependence of the radiant intensity.

$$I(t)=\frac{\hbar\omega_0}{4\mu\tau_N}(N\mu+1)^2\ \mathrm{sech}^2\left(\frac{t-t_0}{2\tau_N}\right), \tag{2a}$$

in which

$$\frac{1}{\tau_N}=(N\mu+1)\frac{1}{\tau_1} \tag{2b}$$

and

$$t_0=\tau_N\ \ln\ (N\mu), \tag{2c}$$

where $N$ is the number of dipoles, $\mu$ is the form factor for their mutual positions which determines the degree to which they interact, $\tau_1$ is the characteristic emission time for an isolated dipole, $\tau_N$ is the characteristic emission time for the macrodipole, and $t_0$ is the pulse delay time or the duration of the macrodipole formation stage. Here it is assumed that all the dipoles are identical and are in an excited state at $t=0$.

In the case of a radiating body in the shape of a cylinder with cross section $S$, the expression for $\mu$ takes the form[7]

$$\mu=\frac{3\lambda^2}{8\pi S}. \tag{3}$$

Taking into account the loss of phase coherence (dephasing) of the dipoles in a semiconductor material, with a characteristic time $T_{\mathrm{deph}}$, increases the time for the establishment of phase coherence of the dipoles (the delay in the superradiant pulse) to[3]

$$t_0^*=t_0\left(1+\frac{\sqrt{t_0\tau_N}}{T_{\mathrm{deph}}}\right). \tag{4}$$

On the other hand, the shape of the spectrum line is a convolution of the form factors for homogeneous $(F(\omega))$ and inhomogeneous $(R(E))$ broadening,[15] where

$$R(\hbar\omega)=\int_0^{+\infty}R_0(E)F\left(\frac{E-\hbar\omega}{\hbar}\right)dE. \tag{5}$$

In contrast with Eq. (1), which yields the standard Lorentz broadening form factor, Eq. (2) gives

$$F(\omega-\omega_0)\propto 2\pi\tau_N\,\mathrm{sech}\,[\pi\tau_N(\omega-\omega_0)], \tag{6}$$

which, for negligible inhomogeneous broadening, i.e.,

$$R_0(E)=\delta(E_0),$$

leads to

$$R(E)=A\ \mathrm{sech}\left(\pi\tau_N\frac{E-E_0}{\hbar}\right). \tag{7}$$

A line with this shape has characteristic exponential, symmetric rise and fall, which have been observed experimentally.[16] It has been pointed out[7] that optical losses can cause an asymmetry of the spectrum, which has been observed.[15] According to Eq. (7), the characteristic energy $\varepsilon$ (slope of the rise and fall), determined experimentally from the spectrum, represents the quantity

$$\varepsilon=\frac{\hbar}{\pi\tau_N},$$

which makes it possible to calculate the characteristic collective radiation time as

$$\tau_N=\frac{\hbar}{\pi\varepsilon}. \tag{8}$$

## EXPERIMENT

We have studied samples of various AlGaAs/GaAs laser heterostructures with a single InGaAs quantum well that has a width of 100 Å. The structures were grown by molecular beam epitaxy. As noted above, selective optical losses during extraction of the radiation from the sample distort the initial emission spectrum. These losses occur, in particular, during waveguide propagation of the light along the epitaxial layers. Thus, the samples were prepared so that the radiation would emerge perpendicular to the epitaxial layers. The end cleavages of the samples were processed by selective etching in order to suppress laser action and coated with high refractive index black paint. Thus, in terms of their operating regime, the test samples were surface-radiating, ligh-emitting diodes.

For the temperature studies, the crystals were soldered, with the epitaxial layers underneath, onto a copper heat sink, which made it possible to control the temperature of the active region of the sample reliably when it was placed in a cryostat. A quasicontinuous current (3 $\mu$s, 5 kHz) was used for pumping.

We have shown[16] that the emission spectrum of a quantum well at $T=77$ K corresponds almost ideally to the homogeneously broadened spectrum of a superradiance line [Eq. (7)]. It is perfectly evident that at higher temperatures the thermal spread of the carriers should distort the spectrum, since the factor $R_0$ in Eq. (5) cannot be represented in the form of a $\delta$-function. This has been verified experimentally. Figure 2 is a semilog plot of the emission spectra at different temperatures for a pump current density of 500 A/cm$^2$. Clearly, at 100 K the homogeneous broadening factor is dominant and the spectrum has a distinct symmetric exponential rise and fall. With increasing temperature, the peak in the spectrum shifts toward lower energies in accordance with the temperature dependence of the band gap width. The drop in the spectrum to the right is distorted by emission from carriers with energies substantially greater than the band gap. Beginning at 250 K, the spectrum has a distinct plateau. The

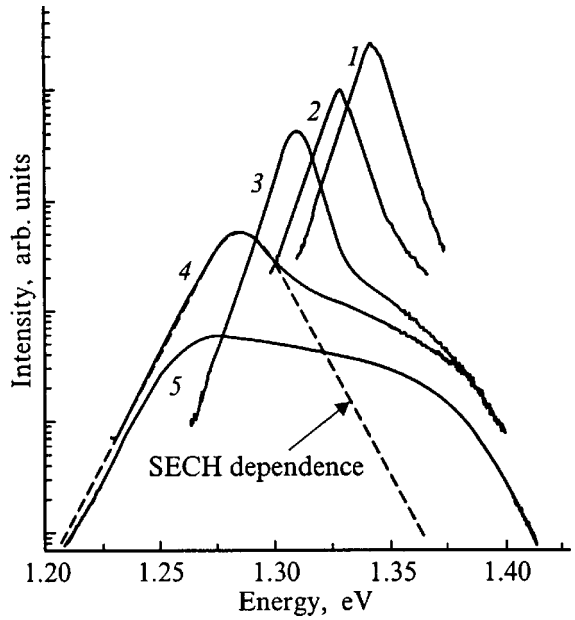


FIG. 2. Spontaneous emission spectra of a quantum-well laser heterostructure at temperatures $T$ (K): *1* — 100, *2* — 150, *3* — 200, *4* — 250, *5* — 300. The pump current density is 500 A/cm$^2$.

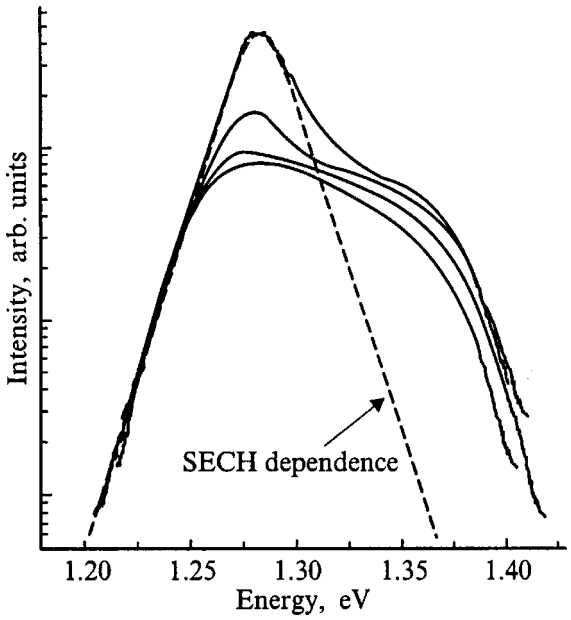


FIG. 4. Spontaneous emission spectra of the quantum-well laser heterostructure at pump current densities of 166, 500, 830, and 1660 A/cm$^2$. $T=300$ K.

slope of the left edge of the spectrum decreases with temperature, but it is still distinctly exponential, so it is possible to calculate the parameter $\tau_N$ in the entire temperature range. This dependence is plotted in Fig. 3, which also shows $\tau_N$ for other current densities. The nonmonotonic variation in these curves is noteworthy.

On the whole, inhomogeneous broadening of the emission line predominates at room temperature for this current density.

The emission spectrum of the samples was also studied in a wide range of pump current densities at temperatures ranging from 77 K to room temperature. The higher the pump current was, the longer the homogeneous broadening predominated as the temperature was raised. Figure 4 illustrates the dependence of the emission spectrum on current at room temperature. It is clear that, for pumping at 500 A/cm$^2$ the spectrum has a flattened peak, and that as the current is raised further, a maximum appears with a characteristic shape similar to that given by Eq. (7). The right-hand edge of the spectrum continues to be broadened by the thermal distribution of the carriers. The spectrum also shows that for a current density of 1660 A/cm$^2$, most of the energy is emitted by a collective resonance. The dependence of the characteristic time $\tau_N$ on the pump current at room temperature calculated from the slope of the left edge of the spectrum is shown in Fig. 5. It is noteworthy that this parameter varies little when the pump current is changed by an order of magnitude, while Eq. (2b) implies a reciprocal dependence of $\tau_N$ on $N$ for $\mu N \gg 1$, i.e.,

$$\tau_N = \tau_1/\mu N, \quad \mu N \gg 1. \tag{9}$$

It is significant that the falloff on the right of the emission spectrum is close to exponential. Probably the entire spectrum is formed by a set of optical resonance processes, but the theoretical curves shown here indicate that, as the pump current is raised, a single collective process encom-

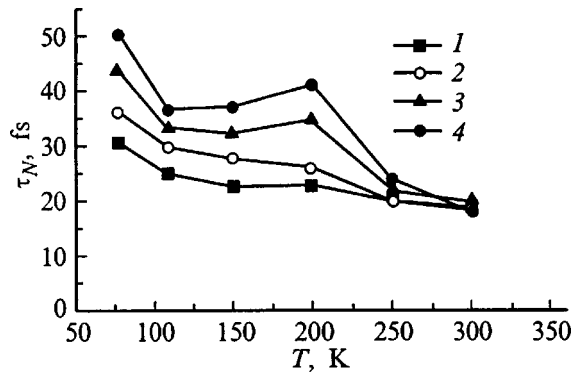


FIG. 3. Characteristic collective emission time ($\tau_N$) of the quantum-well laser heterostructure as a function of temperature ($T$). Pump current density (A/cm$^2$):*1* — 330, *2* — 500, *3* — 660, *4* — 830.

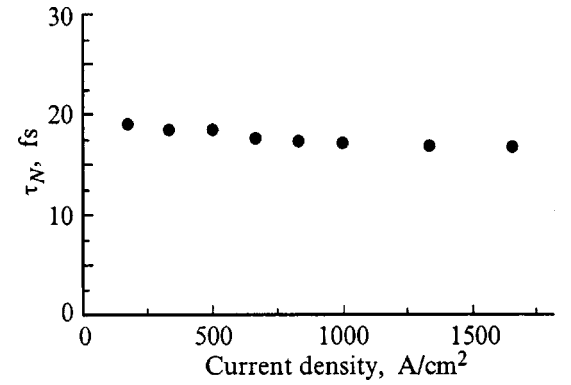


FIG. 5. The characteristic collective emission time ($\tau_N$) of the quantum-well laser heterostructure as a function of the pump current density. $T=300$ K.

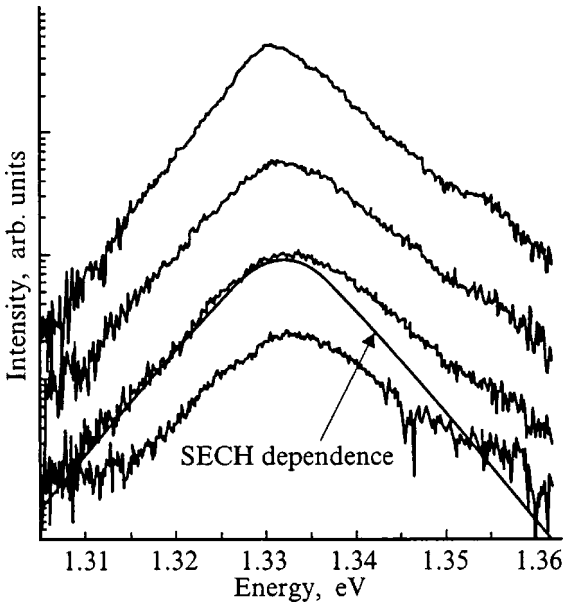


FIG. 6. Spontaneous emission spectra in a structure with a small aperture for pump currents of (bottom to top) 15, 30, 240, and 960 $\mu$A. $T=77$ K. The aperture size is 4 $\mu$m.

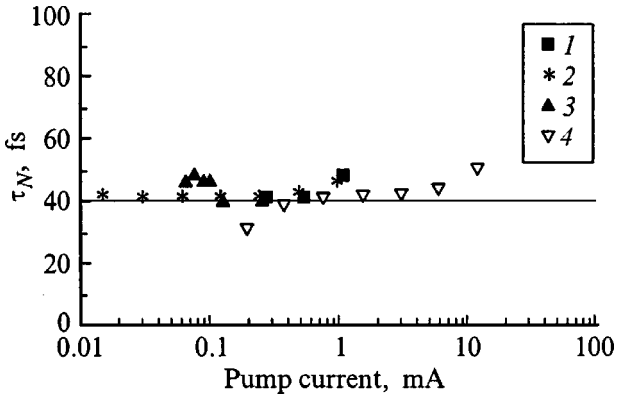


FIG. 7. The characteristic collective emission time ($\tau_N$) of a quantum-well laser heterojunction structure with small apertures as a function of the pump current for aperture sizes of 1.5 (*1*), 4 (*2*), 6(*3*), and 20 $\mu$m (*4*).

passes ever higher energies, while maintaining the exponential falloff on the left almost unchanged. This observation may make it possible to account for the shift in the peak of the ''spontaneous'' emission spectrum as the pump current is raised.

The radiating ensemble has a characteristic size that does not exceed the path of the light in the semiconductor over a time $\tau_N$.[17] The characteristic superradiance time implies that at room temperature the emitting region is smaller than 1.5 $\mu$m.

It has been shown[16] that at liquid-nitrogen temperatures superradiance takes place at pump current densities as low as 170 A/cm$^2$. This raised the question of how large a space can be occupied by an optical resonance.

In order to study the dependence of the characteristic emission time on the transverse dimensions of the active region of InGaAs quantum well AlGaAs/GaAs heterostructures, light-emitting diodes with small oxide apertures were prepared as active regions using the technology employed for creating vertical cavity surface emitting lasers (VCSEL).[18] However, the surface of the heterostructures was not covered with a dielectric mirror and this prevented lasing. The diameter of the apertures was varied from 20 to 1.5 $\mu$m. These studies were made at 77 K. For the measurements, a sample was glued with thermally conducting glue, substrate facing downward, onto a copper holder. This way of mounting the sample inevitably increases the thermal resistance. In addition, the high ohmic resistance of the small aperture caused significant heating of the active layer, i.e., the actual temperature of the active layer exceeded 77 K. Nevertheless, the resulting emission spectra (Fig. 6) are in fairly good agreement with Eq. (7) and always exhibit a pronounced exponential rise and fall. It is apparent from Fig. 7 that no significant dependence of the characteristic emission time $\tau_N$ on the aperture size was observed. Although this parameter limits the size of the radiating region just to a level of $\sim 4$ $\mu$m, according to this experiment, the actual scale length of the radiating group (the characteristic superradiance time is 40–50 fs) is considerably smaller than 1.5 $\mu$m, i.e., is clearly less than five times the wavelength of the radiation in the semiconductor.

The experiment with small-diameter oxide apertures also made it possible to establish an upper limit for the absolute current at which the shape of the spectrum still contains traces of superradiance. It is apparent from Fig. 6 that the spectrum for a current of 30 $\mu$A is in good agreement with the theory of superradiance, while for a pump level of 15 $\mu$A, this cannot be stated with certainty due to the high noise level. It is important to note that the characteristic time $\tau_N$ corresponding to a 30 $\mu$A pump current does not change significantly when the absolute pump current is raised by three orders of magnitude (Fig. 7).

Currents at a level of 30 $\mu$A correspond to the recombination of $\sim 2\times 10^{14}$ electron-hole pairs per second, which for a typical average carrier lifetime of $\tilde{\tau}=3$ ns yields an average of $N=6\times 10^5$ pairs within a region with a diameter of 4 $\mu$m. Here a characteristic spectrum corresponding to superradiance with $\tau_N=42$ fs was observed.

## DISCUSSION

Figure 8 shows the time delay to the superradiant pulse, $t_0^*$, as a function of the number $N$ of participating dipoles calculated using Eqs. (2)–(4) (Ref. 7) for different dephasing times $T_{\text{deph}}$. $T_{\text{deph}}=100$ fs corresponds to room temperature.[3] At liquid-nitrogen temperature, $T_{\text{deph}}$ is a few picoseconds,[1)] so that $T_{\text{deph}}=1$ ps is a reasonable estimate for the temperature, 77 K, at which the experiment was done. For $N=6\times 10^5$ a calculation gives a delay (phasing) time of $\sim 3$ ns. Based on the assertion which was proved above – that the actual typical size of the radiating group of dipoles is less than 1.5 $\mu$m, we must assume that the real number of electron-hole pairs that actually produce the superradiant pulse is smaller by an order of magnitude in this experiment, i.e., is no more than $5\times 10^4$. This yields a value for $t_0^*$ of hundreds of nanoseconds. It is well known that such radiation delay times are not observed in direct experiments. (In

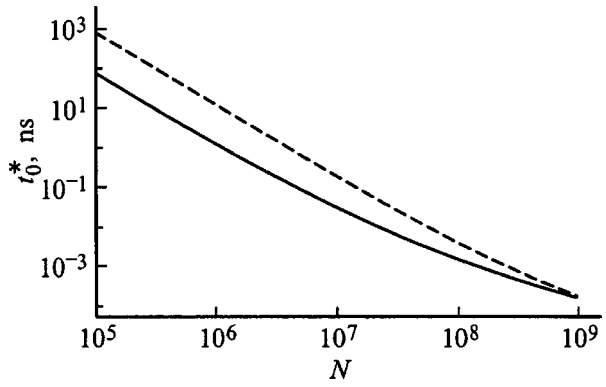


FIG. 8. The dependence of the delay time until laser turn on ($t_0^*$) as a function of the number of dipoles ($N$) for dephasing times $T_{\text{deph}}=1000$ fs (solid curve) and $T_{\text{deph}}=100$ fs (dashed curve).

fact, we are unaware of any experiments on the direct measurement of the switch-on delay in light-emitting diodes at pump currents of 30 $\mu$A.) The calculated time $\tau_N$ for this value of $N$ (assuming that $\tau_1=3$ ns) is on the order of 70 ps, in obvious conflict with the spectral data from our experiment.

Knowing the number of electron-hole pairs that produce an optical pulse upon recombination, we can estimate the pulse energy. For $N=5\times10^4$, at this wavelength it is $\sim$10 fJ.

Equation (9) implies that, in order to attain the observed $\tau_N=42$ fs for $\tau_1=3$ ns, it is necessary that $\mu N\sim0.7\times10^5$. On the other hand, for the experimental parameters, Eq. (3) gives $\mu\sim7\times10^{-4}$, i.e., the number of dipoles must be $N\sim10^8$, or more than two orders of magnitude higher than the experimental value. Accumulating this number of carriers at a current of 30 $\mu$A would require about 0.5 $\mu$s. As noted above, the actual size of the radiating collective is substantially less than 4 $\mu$m and the actual value of $N$ is smaller by at least an order of magnitude. However, it is apparent from Eq. (3) that a reduction in $S$ leads to an inversely proportional change in $\mu$, so that, for a given density of dipoles in the plane, the characteristic superradiance time is independent of $S$. This sort of independence of $\mu N$ from the aperture size is in excellent agreement with the experimental data.

If we proceed from the fact that $N$ is the number of electron-hole pairs in the active region, then we should observe a strong dependence of the emission spectrum on the pump current. At the same time, the experiment indicates the exact opposite: the spectrum does not change when the pump current (and the pump current density) is varied by almost three orders of magnitude. It should be noted that the estimated superradiance time[16] for surface radiating diodes based on heterostructures similar to those studied here is essentially the same as the times calculated for small apertures and also depends weakly on the pump current density.

In order to resolve this contradiction, a number of calculations must be done to determine $N$ from an analysis of the emission spectrum.

Here it is important to note that the parameter $\tau_1$ cannot be measured directly, since it has the significance of a radiative lifetime for an isolated electron-hole pair. The value of 3 ns chosen above as a basis is a typical experimental value of another physical quantity, namely the average carrier lifetime $\tilde{\tau}$ for a high excitation level. Certainly, during a resonant interaction of the carriers, $\tau_1$ should always be greater than $\tilde{\tau}$. The largest value of $\tilde{\tau}$ for quantum wells known to us is 650 ns,[19] which raises the required value of $N$ by more than an order of magnitude. It may be concluded that the required number of dipoles in no way corresponds to the number of injected carriers.

Thus far, we have assumed implicitly that only excited dipoles participate in the collective resonance. Evidently, this cannot be so. A dipole that is capable of absorbing radiation with a given wavelength is just as much a participant in the resonance as a radiating dipole in immediate proximity to it. Thus, we are dealing with a system of closely spaced dipoles, of which only a small fraction is in an excited state. Certainly, excited centers in the lattice interact with unexcited centers through an electromagnetic field and the process shows up as a quantized response of the electronic system of the crystal as a unified whole to excitation by a current. In fact, given the above mentioned peculiarities of the parameter $\mu$, the product $N\mu$ is independent of the size of the aperture, although it should depend on the thickness of the active layer and optical boundary factors (the presence of waveguides, mirrors, optical losses, etc.), as well as on the temperature.

From the basic principles of quantum mechanics, it is known that a single photon is absorbed in an interaction with the electronic system of a crystal as a unified whole, even though an electron-hole pair is formed at a single, definite center. This follows obviously from studies of the absorption spectrum. The results presented here provide serious justification for considering that the converse statement regarding the emission spectrum is also true.

## CONCLUSIONS

In this paper we have, for the first time, been able to observe spectral manifestations of superradiance in semiconductor heterostructures at room temperature. The characteristic superradiance time has been determined as a function of temperature and pump current for the first time on the basis of spectral data. It ha been shown for the first time that superradiance in a quantum well can occur at a pump current of 30 $\mu$A, as well as in an active zone with a diameter of 1.5 $\mu$m.

The data obtained here indicate that luminescence in these semiconducting materials is not the result of the recombination of isolated electron-hole pairs, but is a mechanism for the relaxation of excitation in the electronic system of the crystal as a whole.

This work was supported by Grant No. 98-02-18212 of the Russian Fund for Fundamental Research, ''A study of the spatial-temporal structure of radiation from quantum-well and quantum-dot heterostructures in III-V systems.''

[1)]Personal communication from P. P. Vasil'ev.

[1] A. A. Belyanin, V. V. Kocharovsky, and V1. V. Kocharovsky, Quantum Semiclassic. Opt. **10**, L13 (1998).
[2] D. G. Deppe, Phys. Rev. A **54**, 2506 (1996).
[3] P. P. Vasil'ev, Kvant. Elektron. (Moscow) **24**, 885 (1997).
[4] A. A. Belyanin, V. V. Kocharovsky, and V1. V. Kocharovsky, in *Proceedings of the 6th International Symposium Nanostructures: Physics and Technology* (St. Petersburg, 1998), p. 398.
[5] F. T. Arecchi and E. Courtens, Phys. Rev. A **2**, 1730 (1970).
[6] M. F. H. Shuurmans, Q. H. F. Vrehen, and D. Polder, Adv. At. Mol. Phys. **17**, 167 (1981).
[7] R. Friedberg and S. R. Hartmann, Phys. Lett. A. **37**, 285 (1971).
[8] R. H. Dicke, Phys. Rev. **93**, 99 (1954).
[9] A. I. Guriev, A. V. Grudinin, A. G. Deryagin, S. V. Zaitsev, D. V. Kuksenkov, V. I. Kuchinskiĭ, E. L. Portnoi, and I. Yu. Khrushchev, Pis'ma Zh. Tekh. Fiz. **18**(3), 38 (1992) [Sov. Tech. Phys. Lett. **18**, 45 (1992)].
[10] E. M. Dianov, A. B. Grudinin, I. Yu. Khrushchev, D. V. Kuksenkov, E. L. Portnoi, and S. V. Zaitsev, Sov. Lightwave Commun. **2**, 31 (1992).
[11] A. M. Georgievskiĭ and S. V. Zaitsev, PTÉ (1), 132 (1996).
[12] S. V. Zaitsev and A. M. Georgievski, in *Proceedings of the International Conference SPIE on Optical Diagnostics of Materials and Devices for Opto-, Micro-, and Quantum Electronics* (Kiev, 1995), p. 319.
[13] S. V. Zaitsev and A. M. Georgievskiĭ, Fiz. Tekh. Poluprovodn. **32**, 366 (1998) [Semiconductors **32**, 332 (1998)].
[14] S. V. Zaitsev, N. Yu. Gordeev, M. P. Soshnikov, J. S. Massa, and G. S. Buller, J. Appl. Phys. **84**, 5441 (1998).
[15] P. G. Eliseev and I. V. Akimova, Fiz. Tekh. Poluprovodn. **32**, 472, 478 (1998) [Semiconductors **32**, 423, 428 (1998)].
[16] A. M. Georgievskiĭ, S. V. Zaitsev, N. Yu. Gordeev, V. I. Kopchatov, L. Ya. Karachinskiĭ, I. I. Novikov, and P. S. Kop'ev, Fiz. Tekh. Poluprovodn. **33**, 847 (1999) [Semiconductors **33**, 762 (1999)].
[17] A. V. Andreev, V. I. Emel'yanov, and Yu. A. Il'inskiĭ, Usp. Fiz. Nauk **131**, 653 (1980).
[18] D. L. Huffaker, O. Baklenov, L. A. Graham, B. G. Streetman, and D. G. Deppe, Appl. Phys. Lett. **70**, 2356 (1997).
[19] A. Hariz, P. Daniel Dapkus, H. C. Lee, E. P. Menu, and S. P. Den-Baars, Appl. Phys. Lett. **54**, 635 (1989).

Translated by D. H. McNeill

## AMORPHOUS, GLASSY, AND POROUS SEMICONDUCTORS

# Effect of $\gamma$ irradiation on the photoluminescence kinetics of porous silicon

V. F. Agekyan and Yu. A. Stepanov

*Institute of Physics, St. Petersburg State University, 199034 St. Petersburg, Russia*

V. V. Emtsev, A. A. Lebedev, D. S. Poloskin, and A. D. Remenyuk

*A. F. Ioffe Physicotechnical Institute, Russian Academy of Sciences, 194021 St. Petersburg, Russia*
(Submitted June 11, 1999; accepted for publication June 15, 1999)
Fiz. Tekh. Poluprovodn. **33**, 1462–1464 (December 1999)

The effect of $\gamma$ irradiation on the photoluminescence decay dynamics in porous silicon is investigated. Growth of the photoluminescence intensity and decrease of the decay time in irradiated porous silicon are explained by a lowering of the barriers to recombination of spatially separated electrons and holes via tunneling. The $\gamma$ irradiation of porous silicon leads to a greater dispersion of the decay time. © *1999 American Institute of Physics.* [S1063-7826(99)01312-5]

### INTRODUCTION

Interest in porous silicon and in other porous semiconductors was initiated by the discovery of visible luminescence in porous silicon[1] and the concomitant potential of creating emitting devices for silicon-based optoelectronics. However, due to the extremely high resistivity of porous silicon and the instability of its properties, the path to the fabrication of light-emitting elements based on porous silicon has been longer and more arduous than expected initially. In the course of studies of porous silicon it was found that this material is of interest for other device applications.[2–6] For this reason the problem of the radiation stability of porous silicon and the dependence of its optical properties on irradiation have acquired increased importance. In earlier studies we investigated the influence of $\gamma$ and $\alpha$ radiation on the luminescence properties of porous silicon.[7–9] In this paper we report the results of an experimental study of the effect of $\gamma$ irradiation on the photoluminescence (PL) kinetics of porous silicon.

### SAMPLES AND EXPERIMENTAL TECHNIQUE

Samples of porous silicon were prepared by electrochemical etching of polished wafers of *p* silicon with {100} orientation and resistivity 2 $\Omega\cdot$cm under ultraviolet illumination in a regime providing high brightness of photoluminescence. Hydrofluoric acid buffered with an aqueous solution of $NaNO_2$ served as the electrolyte. The investigated samples remained on the silicon substrate.

The $^{60}$Co isotope with an intensity of $10^{13}\,\mathrm{cm}^{-2}\cdot\mathrm{s}^{-1}$ was used as the $\gamma$-radiation source. Irradiation of the samples took place at room temperature up to a dose of $\Phi\simeq 5\times10^{18}\,\mathrm{cm}^{-2}$, at which a roughly twofold increase in photoluminescence intensity of was achieved.[7] Photoluminescence kinetics were measured on pairs of samples—twins, one of which was subjected to $\gamma$ irradiation, and the other was simply stored in air and at the time the irradiated sample was studied, the photoluminescence intensity and its decay characteristics on this sample remained unchanged.

Photoluminescence was excited by radiation pulses from a molecular-nitrogen laser (wavelength $\lambda=337.1$ nm) with 5-ns duration and a pulse repetition rate of 100 Hz. The peak intensity of excitation on the surface of the sample was on the order of $10\,\mathrm{kW/cm}^2$, the mean power of the laser radiation on the surface did not exceed a few $\mathrm{mW/cm}^2$. To record the spectra we used a DFS-12 spectrometer. The spectra were recorded either in the constant-current regime or with temporal resolution using a Boxcar-162 stroboscopic integrator in the interval $10^{-9}-10^{-3}$ s.

### MEASUREMENT RESULTS AND THEIR ANALYSIS

As is well known, the decay of photoluminescence in porous silicon after excitation has been switched off has three characteristic segments: a nanosecond segment, which is attributable to recombination of free photocarriers near their place of origin; an intermediate segment, which is associated with relaxation of the carriers; and a microsecond segment, which is due to tunneling recombination of spatially separated carriers.[10–15] Our studies deal with photoluminescence kinetics in the microsecond range of photoluminescence decay.

Characteristic curves of the dependence of the photoluminescence intensity $I_{\mathrm{PL}}$ on time reckoned from the maximum of the laser pulse ($t$) at 77 K for the irradiated and non-irradiated samples are shown in Fig. 1. As can be seen from the figure, the kinetics of photoluminescence decay for the irradiated sample are faster.

Figure 2 compares experimental data on photoluminescence decay for the irradiated sample with results of calculation using a broadened exponential, which usually gives a good description of photoluminescence kinetics with allow-

 

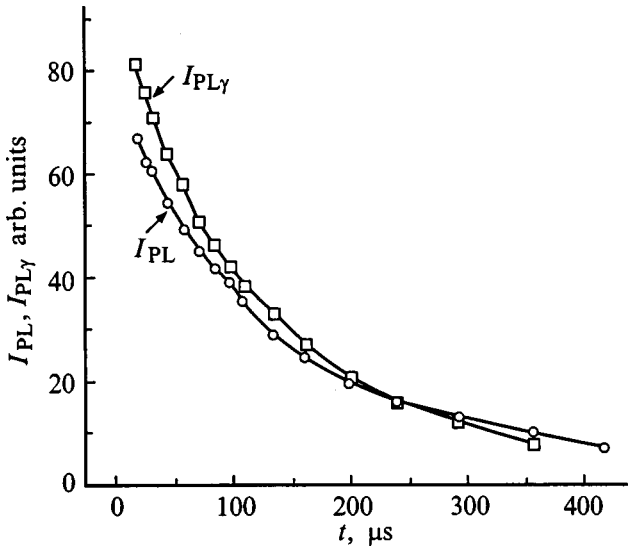


FIG. 1. Dependence of the photoluminescence intensity at the band maximum at λ=720 nm on the time $t$ for an irradiated ($I_{PL\gamma}$) and an unirradiated ($I_{PL}$) sample. $\Phi=5\times10^{18}$ cm$^{-2}$, $T=77$ K.

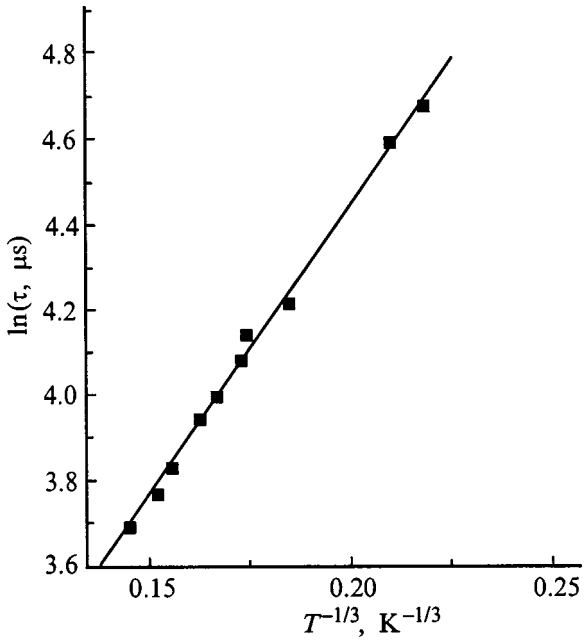


FIG. 3. Temperature dependence of the characteristic decay time of the photoluminescence $\tau$ at the wavelength λ=0.716 μm for an unirradiated sample of porous silicon.

ance for migration of excited carriers in disordered and inhomogeneous media,[11–15]

$$I_{PL}\sim f(x)=(t/\tau)^{1-\beta}\exp[-(t/\tau)^{\beta}]. \quad (1)$$

Here $x=t/\tau$, $\tau$ is the characteristic decay time of the photoluminescence, and $\beta$ is a parameter which varies in the limits from 1 to 0.

As can be seen from Fig. 2, the photoluminescence kinetics are well described by the function (1). For our samples $\beta$, obtained from the contour of the photoluminescence band, is found in the limits 0.5−0.8 and on the long-wavelength tail of the photoluminescence band the dependence of the photoluminescence intensity on time approaches an exponential. The value of $\tau$ was determined from the points at which $d[\ln f(x)]/dx=-1$, where $x=1$ and $\tau=t$. The values of $\tau$ obtained in this way were 150±50 μs for the $\gamma$-irradiated samples and 250±50 μs for the unirradiated samples. Consequently, irradiation shortens the decay time of photoluminescence over the entire spectrum.

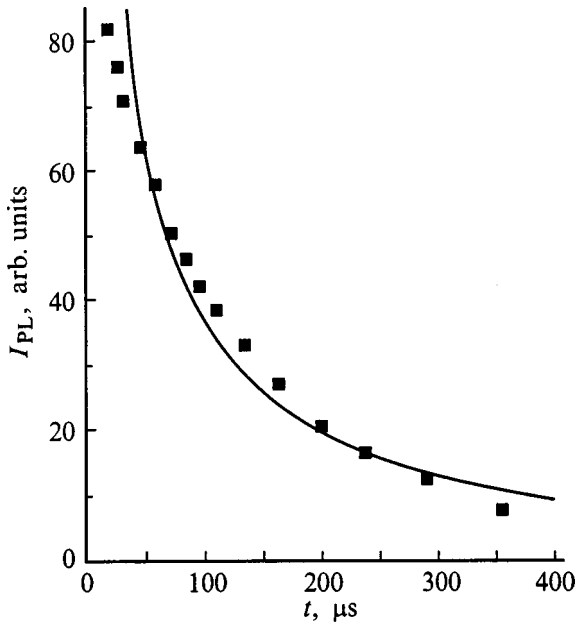


FIG. 2. Comparison of experimental and calculated dependence of the decay of photoluminescence for a $\gamma$-irradiated sample at the photoluminescence band maximum. $T=77$ K. $\beta=0.45$; $\tau=128$ μs.

The mechanism of tunneling recombination of spatially separated carriers is also confirmed by the results of temperature measurements of the decay time $\tau(T)$, which were performed at the band maximum. The dependence $\tau(T)$ was determined in the temperature interval 77−400 K (Fig. 3). The points closely satisfy the dependence $\tau^{-1}\sim\exp(-T_0/T)^{1/3}$, which is characteristic of recombination with tunneling through barriers of different height which separate regions of generation and regions of recombination of charge carriers (a partially disordered medium).[12,15]

The variation of $\tau$ over the contour of the photoluminescence band for the irradiated and unirradiated samples is shown in Fig. 4. Since the experimental dependence on a logarithmic scale is nearly linear, we infer an exponential dependence of the probability of radiative recombination on the energy $E$: $W\sim1/\tau\sim\exp(E/E_0)$, where $E_0=\Delta E/\Delta(\ln\tau)$. This is also evidence that photoluminescence is due to recombination of spatially separated charge carriers tunneling through barriers that separate regions of carrier generation under optical excitation. The mean barrier height $E_0$, obtained from experimental dependence of the type shown in Fig. 3, is ~0.3−0.4 eV, in good agreement with the values obtained by other authors.[12,14,15] For irradiated samples $E_0$ is approximately two times smaller than for unirradiated samples. This means that as a result of $\gamma$ irradiation of porous silicon, the barrier height for carrier tunneling is lowered and the probability of radiative recombination grows. The slower growth of the photoluminescence intensity as a

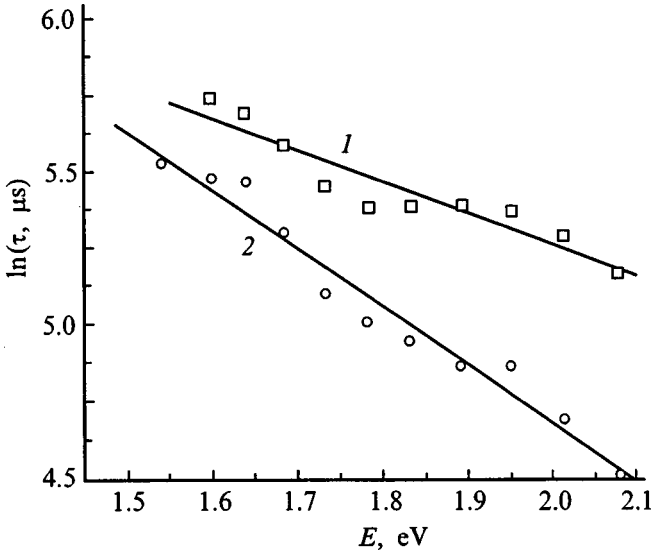


FIG. 4. Dependence of the decay time of the photoluminescence intensity on photon energy. *1* — unirradiated sample, *2* — irradiated sample ($\Phi = 5\times10^{18}\,\mathrm{cm}^{-2}$). Points — experiment, lines — least-squares fit. $T = 300$ K.

result of irradiation clearly shows that irradiation increases the probability of nonradiative recombination.

## CONCLUSIONS

We have investigated relaxation of photoluminescence of $\gamma$-irradiated and unirradiated porous silicon in the microsecond range. Photoluminescence decay is nonexponential and is described by a broadened exponential both for $\gamma$-irradiated and unirradiated samples. The photoluminescence decay time, which is determined using the above-indicated procedure, lies in the range $100-300$ $\mu$s. The decay time depends on the energy of a photon. Analysis of the measured dependences apparently points to an important role for tunneling processes in radiative recombination of charge carriers in porous silicon. The increase in the photoluminescence intensity upon irradiation is accompanied by a decrease in the decay time for the irradiated samples, which indicates a lowering of the barrier to tunneling of spatially separated carriers. Irradiation leads to a narrower dispersion of the decay time.

We wish to thank E. V. Astrov for making samples available for study and for useful discussions.

This work was carried out with the support of the programs ''Physics of Solid-State Nanostructures'' (Projects No. 97-1039 and No. 99-1107) and ''Promising Directions in Micro- and Nano-Electronics.''

[1] L. T. Canham, Appl. Phys. Lett. **57**, 1046 (1990).
[2] G. Maiello, S. L. Monica, A. Ferrari, G. Masini, V. P. Bondarenko, A. M. Dorofeev, and N. M. Kzuchits, Thin Solid Films **297**, 296 (1997).
[3] L. Charrier, T. L. Gorju, L. Haji, and M. Guendouz, in *Porous Semiconductors. Science and Technology* (Int'l. Conf., Mallorca, 1998), Abstract P1-05.
[4] M. J. Berger, R. Arens-Fischer, M. Thonissen, M. Kruger, S. Billat, H. Luth, S. Hibrich, W. Theiß, and P. Grosse, Thin Solid Films **297**, 237 (1997).
[5] S. Frohnhoff and M. G. Berger, Adv. Mater. **6**, 963 (1994).
[6] L. Schirone, G. Sotigiu, and F. P. Califano, Thin Solid Films **297**, 296 (1997).
[7] E. V. Astrova, R. F. Vitman, V. V. Emtsev, A. A. Lebedev, D. S. Poloskin, A. D. Remenyuk, and Yu. V. Rud', Fiz. Tekh. Poluprovodn. **30**, 507 (1996) [Semiconductors **30**, 279 (1996)].
[8] E. V. Astrova, V. V. Emtsev, A. A. Lebedev, D. S. Poloskin, A. D. Remenyuk, Yu. V. Rud', and R. F. Vitman, MRS Fall Meeting Proc. **405**, 185 (1996).
[9] A. M. Ivanov, A. A. Lebedev, A. D. Remenyuk, and Yu. V. Rud', Fiz. Tekh. Poluprovodn. **30**, 188 (1996) [Semiconductors **30**, 107 (1996)].
[10] M. S. Bresler and I. N. Yassievich, Fiz. Tekh. Poluprovodn. **27**, 871 (1993) [Semiconductors **27**, 805 (1993)].
[11] Y. Kanemitsu, S. Okamoto, M. Otobe, and S. Oda, Phys. Rev. B **55**, R7375 (1997).
[12] Y. Kanemitsu, Phys. Rev. B **48**, 12 357 (1993).
[13] L. L. Fedorenko, A. D. Serdarly, É. B. Kaganovich, S. V. Svechnikov, S. P. Dikiĭ, and S. V. Baranets, Fiz. Tekh. Poluprovodn. **31**, 6 (1997) [Semiconductors **31**, 4 (1997)].
[14] Y. H. Xie, W. L. Wilson, F. M. Ross, J. A. Mucha, E. A. Fitzgerald, J. M. Macaulay, and T. D. Harris, J. Appl. Phys. **71**, 2403 (1992).
[15] L. Pavesi, J. Appl. Phys. **80**, 216 (1996).

Translated by Paul F. Schippnick

## PHYSICS OF SEMICONDUCTOR DEVICES

# Photodetectors based on osmium-doped silicon

M. S. Yunusov, R. A. Muminov, G. Nurkuziev, N. Gapparov, and A. Kholboev

*S. V. Starodubtsev Physicotechnical Institute, 700084 Tashkent, Uzbekistan*
(Submitted August 6, 1998; accepted for publication April 10, 1999)
Fiz. Tekh. Poluprovodn. **33**, 1465–1466 (December 1999)

Osmium-doped silicon photodetectors with a low control voltage have been constructed. The *n*-type Si was chosen as the initial material. The silicon was doped with osmium using a diffusion method. The characteristics of these structures are studied at 300 K. © *1999 American Institute of Physics.* [S1063-7826(99)01412-X]

As helium materials science develops, the measurement of the luminous flux at the focus of solar furnaces is becoming important. Controlling the energy parameters of solar radiation fluxes requires photodetectors capable of measuring the light flux in different spectral intervals, in some cases with a good response time. Photodetectors of this type are needed for measuring highly concentrated fluxes of solar radiation.

The photodetectors intended for these purposes must be highly sensitive within the operating wavelength range and have a fast response and a low noise level. In addition, they must be small, use low control voltages, and have a high operational reliability.

The extension of the operating spectral range of coherent and incoherent light sources into the far infrared, on one hand, and into the ultraviolet, on the other, has led to a demand for fast, sensitive photodetectors which operate over a wide spectral range.

The purpose of this paper is to report the construction of osmium doped silicon photodetectors with a low control voltage and a low current, as well as high reliability at high concentrations of solar radiation. Samples of *n*-type Si with resistivities in the range $\rho = 5.5-75\ \Omega\cdot$cm, oxygen contents of $5\times10^{16}-7\times10^{17}\ \mathrm{cm}^{-3}$, and dislocation densities of $10^2-10^4\ \mathrm{cm}^{-2}$ were used as a starting material. The silicon was doped with osmium using a diffusion method.[1] After diffusion annealing, the resistivity of the samples rose to $7\times10^4\ \Omega\cdot$cm and the conductivity underwent a $n\rightarrow p$ transition. After the silicon was doped with osmium, a quasiperiodic inhomogeneity developed in the sample.[2] Fused contacts of Au+Sb alloy and Al with an area $S=(1.5-3.5)\times10^{-2}\ \mathrm{cm}^2$ were made in vacuum with a residual pressure $P=5\times10^{-5}$ Torr for the measurements. The sample thickness was varied in the range 0.3–1 mm. The $p^+-p-n^+$ structures studied here are structurally similar to those examined in Ref. 3. The photocurrent $I_{\mathrm{ph}}$ was measured as a function of voltage (Fig. 1) using an Al-107A light-emitting diode with a wavelength of 0.95 $\mu$m (which coincides with the peak spectral sensitivity of the photodetector) as a light source. It is evident from Fig. 1 that, while gallium arsenide

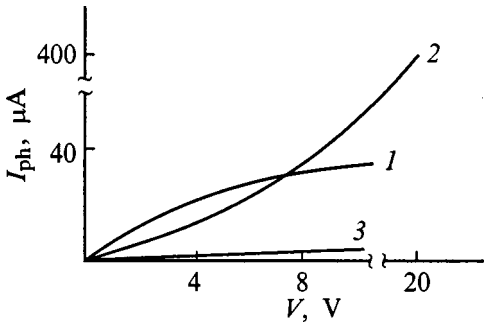


FIG. 1. Photocurrent as a function of bias voltage at 300 K with an Al- 107A light-emitting diode as the source (current 16 $\mu$A) for *1* — an Si⟨Os⟩ $p^+-p-n^+$ structure, *2* — a GaAs $p-n$ structure, and *3* — a GaAs metal-semiconductor-metal structure.

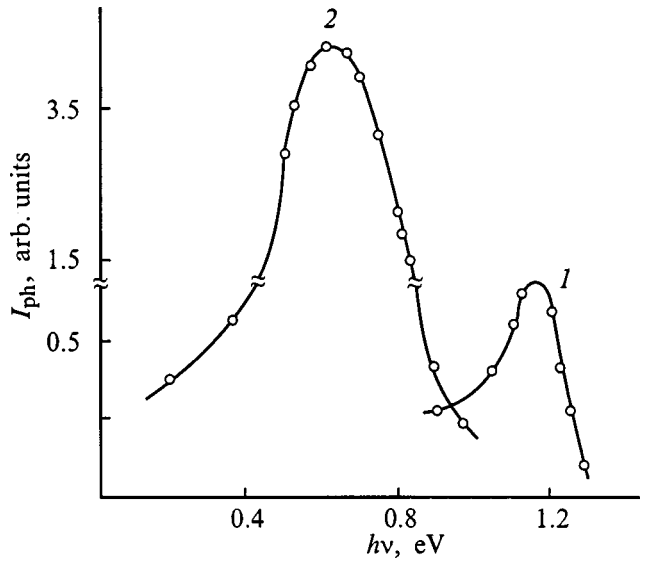


FIG. 2. Spectral characteristics of the photocurrent of an Si⟨Os⟩ $p^+-p-n^+$ structure with a forward bias of 3 V (*1*) and a reverse bias of 3 V (*2*). The measurement temperature was 300 K.

 

structures (curve *2*) have a superlinear rise in the photocurrent as the voltage is raised, the silicon structures have a slower rise in the photocurrent. At $V=6$ V, for example, the photocurrent in the Si⟨Os⟩ $p^+-p-n^+$-structure reaches 27 $\mu$A (Fig. 1, curve *1*). Note that this is more than three orders of magnitude higher than for metal-semiconductor-metal structures based on GaAs (0.009 $\mu$A) (Fig. 1, curve *3*). The comparatively high photocurrent in the Si⟨Os⟩ structures at these voltages is a consequence of the closeness of the charge separation region to the illuminated surface. In this case the optical losses are low. The photocurrent saturates because of a more rapid rise in the dark current of the silicon structure compared to that for an epitaxial GaAs $p-n$-junction. The silicon $p^+-p-n^+$-structures examined here are optically well matched to commercial Al-10A light-emitting diodes and could operate as photodetectors in optoelectronic devices.

Figure 2 shows the spectral characteristics of the Si⟨Os⟩ $p^+-p-n^+$ structures at room temperature. The structures were illuminated with an irradiance of $10^{-4}$ W/cm$^2$ from an IKS-21 spectrometer. It is evident that the osmium-doped silicon photodetector operates over a wide wavelength range. A study of the spectral characteristics showed that the long wavelength photosensitivity edge is shifted when a reverse bias is applied (Fig. 2, curve *2*). This effect is evidently caused by the formation of a dielectric layer

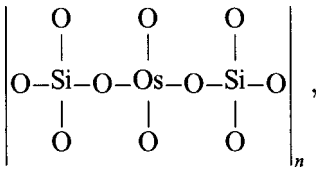

under the contact, which causes a drop in the bias voltage. There was enough oxygen in the silicon to form a layer of this sort.

These experiments have therefore shown that when silicon is doped with osmium, it is possible to create photodiodes with a low reverse voltage and a broad spectral range.

These photodetectors are suitable for use in tomography, fiber optics technology, solid state detector systems, and other devices.[4–8]

[1] S. A. Azimov, M. S. Yunusov, G. Nurkuziev, and F. R. Karimov, Fiz. Tekh. Poluprovodn. **12**, 1655 (1978) [Sov. Phys. Solid State **12**, 1592 (1978)].
[2] A. V. Karimov and G. Nurkuziev, DAN RUz, No. 6 (1993).
[3] M. Balkanski and P. Laleman, *Photonics* (Mir, Moscow, 1978).
[4] W. Tsang (ed.), *Optical Communications Technology–Photodetectors* (Mir, Moscow, 1988).
[5] S. A. Azimov, R. A. Muminov, S. Kh. Shamirzaev, and A. Ya. Yafasov, *Silicon-lithium Nuclear Radiation Detectors* [in Russian], Fan, Tashkent (1981).
[6] P. Jespers, F. Vande, and M. Haight, *Semiconductor Image Signal Shapers* (Mir, Moscow, 1979).
[7] G. K. Poltorapavlova and N. P. Udalov, *Phototransistors*, Energiya, Moscow (1971).
[8] S. Sze, *The Physics of Semiconductor Devices* (Mir, Moscow, 1984).

Translated by D. H. McNeill

# Effect of liquid dielectrics on the efficiency of silicon solar cells

Yu. A. Abramyan, G. G. Karamyan, and A. A. Murodyan

*Institute of Radio Physics and Electronics, National Academy of Sciences of Armenia*

V. I. Stafeev and V. I. Serago

*Institute of Sensor Electronics, Academy of Technological Sciences of the Russian Federation, 117049 Moscow, Russia*

(Submitted August 3, 1998; accepted for publication May 19, 1999)
Fiz. Tekh. Poluprovodn. **33**, 1467–1468 (December 1999)

The results of experimental studies of the change in the photoelectric characteristics of silicon solar cells produced as a result of depositing thin, liquid dielectric layers (glycerine, acetone, isopropyl alcohol, butanol, dioxane, deionized water) are presented. It is shown that the presence of these liquids reduces the forward and reverse currents, substantially raises the short-circuit currents and open-circuit voltage, and significantly increases the efficiency (by up to 40–60%). Possible physical models are proposed for this effect. © *1999 American Institute of Physics.* [S1063-7826(99)01512-4]

The effect of adsorbed water vapor on the photocurrent from silicon photodiodes was apparently described for the first time by Litovchenko and Lyashchenko.[1] Later they described[2] the effect of adsorbed water and acetone molecules on the quantum yield and photocurrent relaxation time. They explained this effect by a change in band bending in the skin layer of the semiconductor.

Molecules adsorbed on silicon and germanium surfaces create an additional positive charge. A negative charge develops on the mobile carriers under the influence of this charge in the surface layer of the semiconductor. In *n*-type silicon this change leads to a rise in the surface conductivity and in *p*-type silicon it causes the development of an inverse conductivity layer. In addition to band bending, adsorbed molecules can also cause changes in the parameters of the adhesion levels.[3] New surface states may also be formed. All of these effects will affect the rate of surface recombination and, therefore, the photoelectric characteristics. This effect shows up especially strongly in solar cells, since the $p-n$ junction lies very close to the surface in them.

## SAMPLES AND EXPERIMENTAL TECHNIQUES

In these studies we used silicon solar cells with a conventional configuration of the contact grid and with sensitive areas of 2, 4, and 20 $cm^2$. The exposed surface was not illuminated prior to deposition of the insulating layer. The efficiency in the initial state was 10–13%. The test samples were placed on the bottom of a vessel (Fig. 1). First, the surface of the solar cells was carefully cleaned by wiping with a wad of cloth dipped in isopropyl alcohol, degreased in boiling toluene and its vapor, and then washed initially with cold water, and then in hot deionized water. After this procedure, the samples were dried in a thermostat for 1–2 h at a temperature of $150-200\,^{\circ}C$.

The load characteristics (the short-circuit current $I$ and open-circuit voltage $U$) were measured for different densities of solar irradiation: diffuse scattered daylight and direct sunlight ($W=70-80\,mW/cm^2$). After these control measurements, the vessel was filled with a test liquid and the measurements were done again at the same solar irradiation intensities.

Liquids with low electrical conductivities ($10^{-7}-10^{-8}\,\Omega^{-1}\cdot cm^{-1}$) were chosen for these studies: glycerine, acetone, isopropyl alcohol, deionized water, butanol, and dioxane. Qualitatively, these liquids all had the same effect. The largest changes in the photosensitivity were observed in acetone and glycerine. We therefore present only the results for glycerine.

## EXPERIMENTAL RESULTS

Figure 2 shows current-voltage characteristics measured in the dark, with and without a layer of glycerine on the surface. The glycerine causes a significant drop in the forward and reverse currents.

Figure 3 shows the load characteristics of a solar cell ($n-p$ type) with and without a layer of glycerine under direct sunlight (sun at the zenith, power level $\sim 70\,W/cm^2$) and in scattered room light. The efficiency under direct sunlight increases by 40–60%, reaching 18–20%. The duty cycle of the load characteristic changes little when the illu-

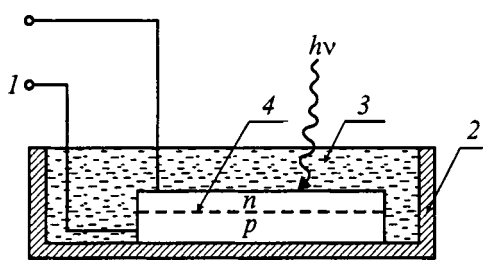


FIG. 1. The location of the solar cell in the vessel: *1* — contact leads, *2* — vessel, *3* — glycerine, *4* — solar cell.

 

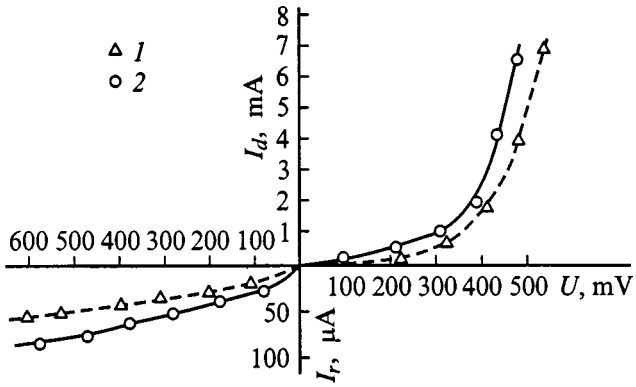


FIG. 2. Dark current-voltage characteristics of the solar cells: *1* — without glycerine, *2* — in glycerine.

mination intensity is varied. The relative change in the short-circuit current and open-circuit voltage depends sublinearly on the illumination level.

As a rule, increasing the thickness of the liquid to 5–6 mm raises the efficiency. Placing a piece of K8 or F1 optical glass with a thickness of 0.5–2 cm on the layer of glycerine has similar effect. Placing the glass on the cell without a layer of glycerine produces the opposite effect because of reflection. The increase in the efficiency depends strongly on the quality of the surface processing. Removing the liquid in the customary way does not return the current-voltage characteristic to its initial state. The adsorbed molecules remaining on the surface continue to have a positive effect.

Measurements of the nonequilibrium carrier lifetime showed that it also increases by almost as much as the photocurrent.

## CONCLUSIONS

These studies show that the main reason for the changes in the current-voltage characteristics and the rise in the photosensitivity and, therefore, in the efficiency, when molecules are adsorbed is a reduction in surface recombination and a change in band bending at the surface. Most likely, this happens because of increased band bending at the surface of the semiconductor. Certainly, the brightening effect of the layer of liquid also contributes. This is suggested by the dependence of the effect on the thickness of the layer of liquid or of the glass covering it. This method for improving the properties of solar cells has been protected by a patent of the Armenian Republic.

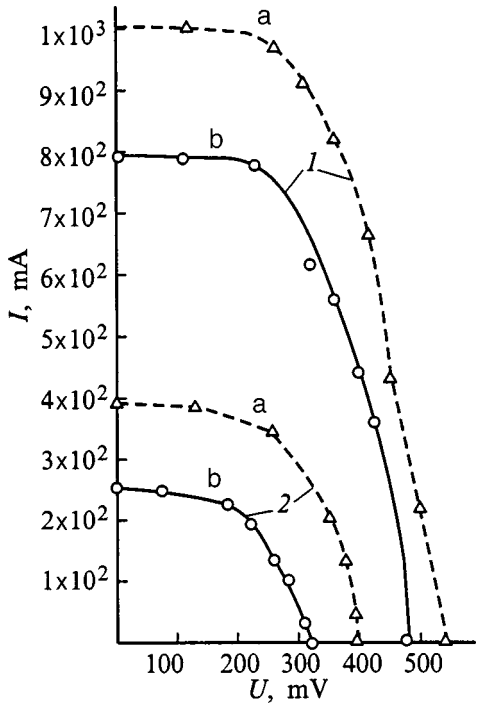


FIG. 3. Current-voltage characteristics of solar cells under load: a — in glycerine, b — without glycerine, *1* — with direct solar irradiation, *2* — with diffuse solar irradiation.

[1] V. G. Litovchenko and V. I. Lyaschenko, Fiz. Tverd. Tela (Leningrad) **5** (II), 3207 (1963) [Sov. Phys. Solid State **5**, 2021 (1963)].
[2] V. I. Lyaschenko, V. G. Litovchenko, I. I. Stepko, V. I. Strikha, and L. V. Lyaschenko, *Electronic Phenomena at Semiconductor Surfaces* [in Russian], Naukova Dumka, Kiev (1968).
[3] V. F. Kiselev, *Surface Phenomena in Semiconductors and Dielectrics* [in Russian], Nauka, Moscow (1970).

Translated by D. H. McNeill

# Two-mode diode-laser spectroscopy with a InAsSb/InAsSbP laser near 3.6 $\mu$m

A. P. Danilova, A. N. Imenkov, N. M. Kolchanova, V. V. Sherstnev, and Yu. P. Yakovlev*)

*A.F. Ioffe Physicotechnical Institute, Russian Academy of Sciences, 194021 St. Petersburg, Russia*

S. Civis

*J. Heyrovsky Institute of Physical Chemistry, CAS, 18223 Prague 8, Czech Republic*
(Submitted June 8, 1999; accepted for publication June 9, 1999)
Fiz. Tekh. Poluprovodn. **33**, 1469–1474 (December 1999)

The current dependence of the output frequency of InAsSb/InAsSbP diode lasers at wavelengths near 3.6 $\mu$m is studied. It is found that in these lasers the number of lasing modes can be reduced without introducing crystallographic defects. It is shown that the photon momentum aids in suppressing the spectral modes closest to the dominant mode. Two-mode laser spectroscopy is done over an interval of 2 $cm^{-1}$ for two gases, $N_2O$ and $CH_3Cl$. © *1999 American Institute of Physics.* [S1063-7826(99)01612-9]

## 1. INTRODUCTION

Single-mode lasers are usually employed in laser spectroscopy.[1–3] However, a laser always generates several modes, since the intervals between the cavity normal frequencies are substantially smaller than the width of the gain spectrum for the active medium. Single-mode lasing is assumed to be random and is thought to occur because there are fewer crystal defects in the antinode of the emission in one mode than in those of the other modes. The monochromator which forms part of a laser spectrometer[4,5] can be tuned to any mode and the medium under study can be scanned with just that mode. In lasers with a controlled injection density over the width of the cavity,[6,7] one may expect small levels of noise from other modes because a continuous waveguide has been introduced into the cavity. The radiation flux is able to oscillate over the width of the cavity in this waveguide,[8] so that buildup of energy in isolated parts of the cavity is prevented, along with the emission of this energy in the form of radiation over a wide mode spectrum.

The purpose of this paper is to study the dependence of the emission intensity and frequency in different modes as a function of current and to examine the feasibility of using these modes for observing absorption lines in gaseous media. This article is a continuation of our previous work on constructing and studying frequency tuneable diode lasers based on double InAsSb/InAsSbP heterostructures.

## 2. LASER DIODES

The main part of the laser diode is a double InAsSb/InAsSbP heterostructure grown by liquid-phase epitaxy on a *p*-InAs (100) substrate with a hole concentration of $(6-8)\times10^{18}\,cm^{-3}$, similar to the structures discussed in Refs. 9 and 10. The structure contains an active layer of InAsSb with a thickness of $\sim1$ $\mu$m and a band gap $E_g=355$ meV at $T=77$ K, which forms a type-I heterojunction with the adjacent clipper layers of InAsSbP with thicknesses of $\sim2$ $\mu$m each and a band gap $E_g=590$ meV at $T=77$ K. The structure is coated with a distributing layer of *n*-InAs with a thickness of 0.5 $\mu$m and doped with Sn to an electron concentration of $\sim10^{19}\,cm^{-3}$. In an active layer not doped intentionally, the electron concentration is $(2-4)\times10^{16}\,cm^{-3}$. The clipper layer adjacent to the substrate was doped with Zn to a hole concentration of $(1-2)\times10^{18}\,cm^{-3}$. The second clipper layer was doped with Sn to an electron concentration of $(5-8)\times10^{18}\,cm^{-3}$. After epitaxial growth of the layers, the substrate was ground to a thickness of 100 $\mu$m. Photolithography was used to fabricate chips with a step of 500 $\mu$m and a mesa width of 16 $\mu$m. Cavities with a length of 300–350 $\mu$m were obtained by cleavage. The chips were mounted by the substrate on a special copper frame[11] which makes it possible to place the laser in a thermostat with a closed helium cycle.

## 3. TECHNIQUE

In order to study the emission spectrum at $T=77$ K, the laser was placed in a nitrogen-cooled evacuable thermostat and powered by 20-$\mu$s square pulses with an off-duty factor of 100. Laser spectrometry on gaseous media was done in a spectrometer with the thermostat (Laser Photonics, model L5731) for holding the laser, a power supply and temperature controller (Laser Photonics, model 5820), a monochromator, and a liquid-nitrogen-cooled InSb photodiode detector. When the laser was powered by sawtooth current pulses, a signal proportional to the intensity of the laser light passing through the gas was scanned on an oscilloscope. As the current was varied smoothly, after about 20 s the second derivative of the signal with respect to the current was recorded using a computer and an SP530. Laser spectroscopy was done on the gases $N_2O$ and $CH_3Cl$. The gases were contained in cells with a length of 21 cm at a pressure of 2 Torr.

 

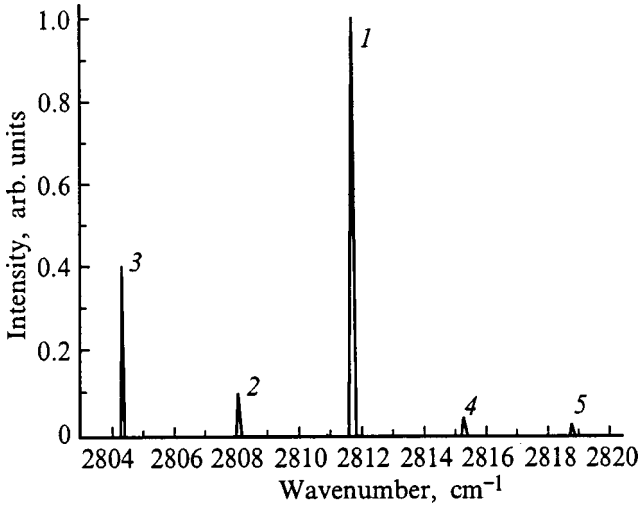


FIG. 1. Emission spectrum of a VII49-1–12 laser for a current of 150 mA and a temperature of 77 K. The mode numbers are indicated.

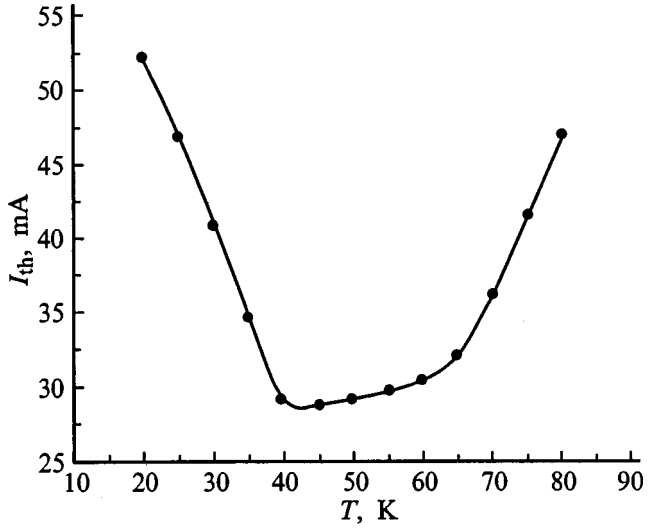


FIG. 3. Threshold current of a V1149-1-12 laser as a function of temperature.

## 4. EXPERIMENTAL RESULTS

### 4.1. Emission characteristics of the laser

The luminescence spectrum of the laser contained several modes (Fig. 1) separated by roughly 3.6 cm$^{-1}$ (50 Å). The frequencies of the different modes increased in almost the same way with the current (Fig. 2a). The change in the wave number for modes 1 and 3 is as high as 2.6–2.8 cm$^{-1}$, which is comparable to the intermode separation. The dependences of the emission intensity of the spectral modes on the current $I$ were different (Fig. 2b). At currents slightly above the threshold $I_{th}=70$ mA, mode *1* predominates with an intensity that initially increases with current (for $I<170$ mA) and then decreases. The next, longer-wavelength mode *2* begins to weaken at a current of $I=120$ mA. The intensity of the longer-wavelength mode *3* increases throughout the entire range of currents for which measurements were made. It becomes the predominant mode for $I>180$ mA. Mode *2* is evidently suppressed by the neighboring modes. The shorter-wavelength modes *4* and *5* (Fig. 1) show up as the current rises ($I>100$ mA) but remain weak over the entire range of currents.

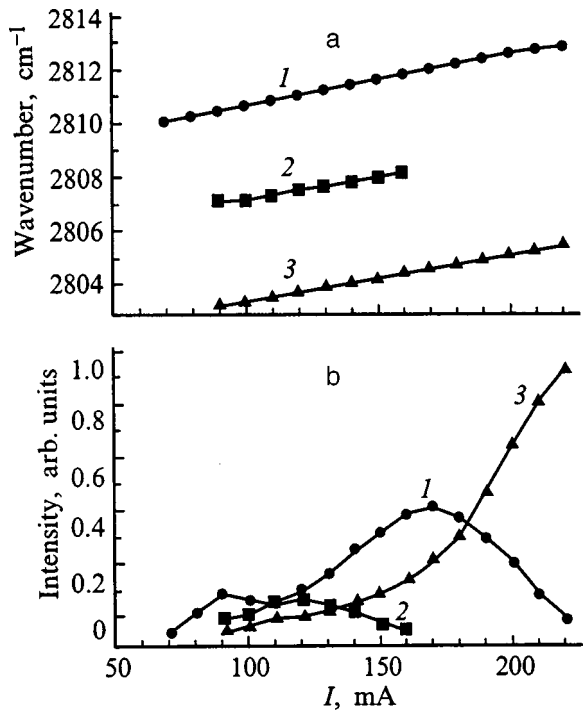


FIG. 2. The current dependences of the lasing frequencies of the major modes (a) and their intensities (b) at 77 K for a V1149-1– 12 laser. The labels on the curves correspond to the mode numbers.

The threshold current $I_{th}$ of the sample represented here has a minimum of ~30 mA at $T=60$ K and increases supralinearly as the temperature varies from that value (Fig. 3) in a manner similar to that described elsewhere.[11,12] The increase in the threshold current as the temperature is lowered is always accompanied by an increase in the series resistance. In these cases, it is difficult to power the laser at temperatures below 20 K.

### 4.2. Scanning gaseous media

The largest intervals for scanning gaseous media (~2 cm$^{-1}$) were obtained at a temperature of 68 K (Figs. 4 and 5). To scan mode 1 the monochromator was tuned to a wave number of 2815 cm$^{-1}$ or to an even higher frequency, if this did not cause a reduction in the signal, and the current was varied from 70 to 170 mA. During scans of mode 3, the monochromator was tuned to a frequency of 2805 cm$^{-1}$ or below, and the current was varied in the range 150−250 mA. The resolution of the monochromator was ~10 cm$^{-1}$. Mode 2 was not scanned.

The objects scanned included a reference Fabry-Perot resonator with a free spectral range of 0.0262 cm$^{-1}$ and the gases $N_2O$ and $CH_3Cl$.

When the reference resonator was scanned with mode 1, a strictly sinusoidal signal was obtained (Fig. 4). The oscillations in the amplitude of the sine wave can be explained by interference of the radiation in the KBr windows enclosing the air-filled resonator volume. The signal from the resonator

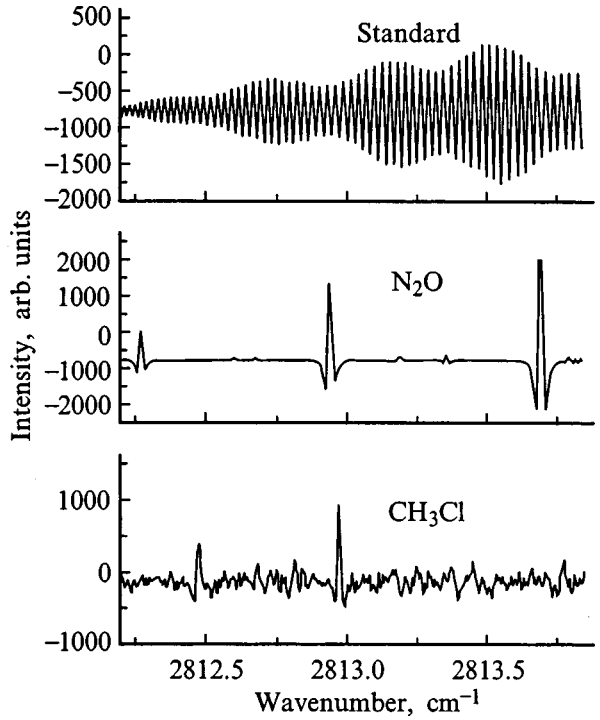


FIG. 4. Transmission spectra of a reference Fabry-Perot cavity, of $N_2O$ gas, and of $CH_3Cl$ gas, obtained by scanning mode *1*.

was also close to sinusoidal during a scan with mode *3* (Fig. 5). The noise in the initial portion of this scan was caused by random switchoff of mode *2*. The scan of $N_2O$ yields the standard absorption lines,[13] which we have used to calibrate the frequency scale of the laser spectrometer. When mode *1* is scanned, the lines lie in the frequency range

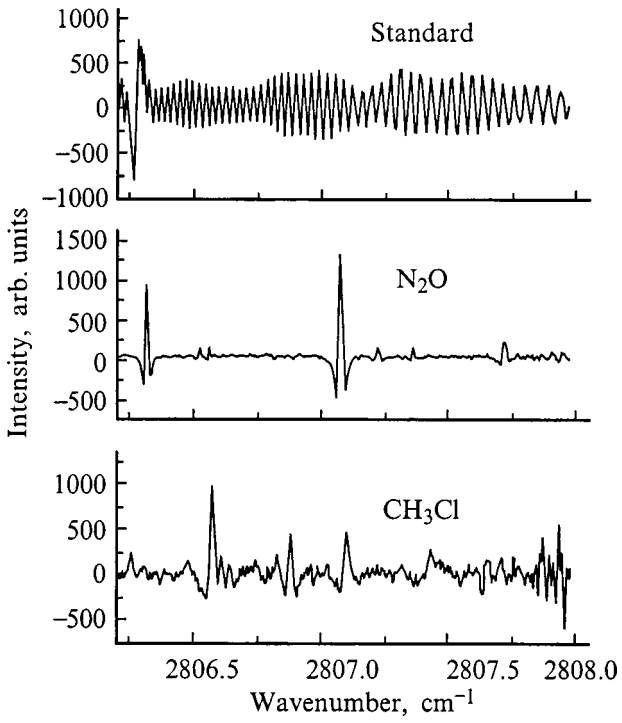


FIG. 5. Transmission spectra of a reference Fabry-Perot cavity, $N_2O$ gas, and $CH_3Cl$ gas obtained by scanning mode *3*.

$2812-2814\,\mathrm{cm}^{-1}$ (Fig. 4) and when mode *3* is scanned, they lie in the range $2806-2808\,\mathrm{cm}^{-1}$ (Fig. 5). No mixing of lines due to lasing at other lines within the chosen scan ranges was observed. Methyl chloride gas ($CH_3Cl$) has many interesting absorption lines in the frequency ranges that we studied (Figs. 4 and 5). It has apparently been studied inadequately in these ranges.

## 5. DISCUSSION OF RESULTS

The generation of several equidistant modes is evidence of a high crystallographic perfection of the main part of the laser. That these modes are equidistant indicates that there are no transverse spatial modes. This may be a consequence of the development of a smooth waveguide over the width of the resonator and of oscillations in the radiation flux within the resonator.[8] The absence of transverse modes greatly reduces the number of spectral modes and makes it easier to use the laser for scanning gaseous media. In addition, many longitudinal modes are partially suppressed by strong neighboring modes. As a result, mode *2* is weak and this makes it easier to use modes *1* and *3* for scanning.

The increase in the lasing mode frequencies with rising current indicates that the injection density increases over the width of the resonator from the middle to the edges owing to the collection of current from the edges of the substrate.[7] However, the ranges over which the lasing frequency varies are a factor of 2 smaller than in Refs. 7 and 10, where the increase in the injection density in the direction along the width of the substrate from the middle to the edges has a stronger effect. This may happen because of poorly perceived differences in the doping of the substrate and the layers, as well as other factors.

The slight reduction in the lasing mode frequencies as the temperature is lowered can be explained by a drop in the charge carrier concentration at the lasing threshold and a consequent increase in the refractive index within the narrow gap active region. The contribution from the temperature-dependent change in the band gap is of opposite sign and is smaller than the observations for temperatures above 80 K.

The growth in the differential resistance of the laser and in the threshold current as the temperature is reduced below 60 K is apparently caused by freezing of holes in the clipping *p*-InAsSbP layer due to their high effective mass. The statistical nonuniformity in doping leads to a spatial nonuniformity in the release of holes and to the appearance of absorbing sections in the laser which require additional gain in the amplifying sections. This causes an increase in both the threshold current and the series resistance of the laser. Using the laser at temperatures below 60 K is undesirable because of the high electric power consumption and the small range over which the output frequency varies with current.

These scans of gases by two laser modes illustrate the promise of using defect-free diode lasers in laser spectroscopy. Absorption lines of nitrous oxide were identified and the laser was calibrated with these lines. Interesting lines of $CH_3Cl$ have been detected within a little studied region of the spectrum.

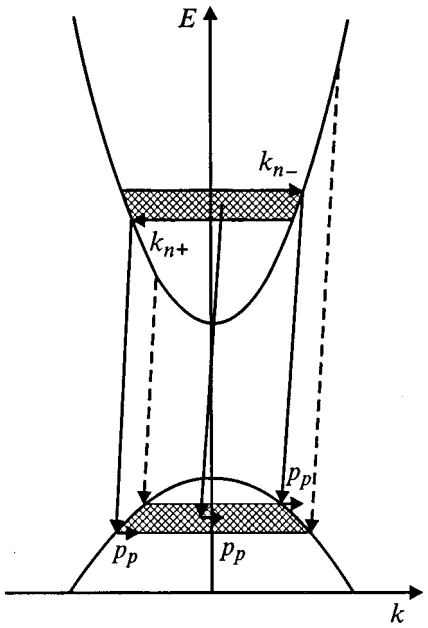


FIG. 6. Illustrating the effect of the momentum of a photon on the suppression of neighboring modes.

The closeness of the intervals over which the lasing mode frequencies can be varied and the intermode separation does create some difficulties in the use of multimode lasers because of the need to separate the scanning modes. However, these intervals can be extended by a factor of 2 or 3 by reducing the resonator length.

## 6. SUPPRESSION OF NEIGHBORING MODES

The suppression of stimulated emission by electron density waves[14] takes place within a substantially narrower range of photon energies than the intermode intervals, so it may not be the main cause. We shall show that the photon momentum provides a much larger interval over which suppression can occur.

The momentum of a photon makes radiative transitions indirect (Fig. 6). The energies of the charge carriers that participate in the transitions are different for different angles between the directions of the momenta of the photon and carrier. Elastic scattering reorients the carriers over a time ($10^{-13}$ s) much shorter than the energy scattering time ($10^{-10}$ s) and the radiative recombination time ($10^{-8}$ s). As a result, one laser mode reduces the carrier concentration within fairly wide energy ranges. The modes in which carriers from these energy intervals could participate are attenuated.

Let us calculate the energy intervals over which neighboring modes are suppressed. The transition energies $h\nu$ for the three different directions of the carrier momenta relative to that of the photon momentum (Fig. 6) are given by

$$h\nu = E_g + \frac{k_{n-}^2}{2m_n} + \frac{(k_{n-}-p_p)^2}{2m_p} \tag{1}$$

for the same directions,

$$h\nu = E_g + \frac{k_{n+}^2}{2m_n} + \frac{(k_{n+}+p_p)^2}{2m_p} \tag{2}$$

for the opposite directions, and

$$h\nu = E_g + \frac{k_{n0}^2}{2m_n} + \frac{k_{n0}^2}{2m_p} \tag{3}$$

for almost perpendicular directions, when the amplitude of the carrier momentum does not change during the transition. Here $E_g$ is the band gap; $m_n$ and $m_p$ are the effective masses of the electrons and holes, respectively, with $m_n \ll m_p$; $k_{n+}$, $k_{n-}$, and $k_{n0}$ are the amplitudes of the momenta of the electron moving in the above directions; and $p_p$ is the amplitude of the photon momentum.

The depletion interval in the conduction band, $\Delta E_n$, determined from Eqs. (1) and (2) is

$$\Delta E_n = \frac{k_{n-}^2 - k_{n+}^2}{2m_n} = \frac{(k_{n-}+k_{n+})p_p}{m_p(1+m_n/m_p)} \approx \frac{2k_{n0}p_p}{m_n+m_p}. \tag{4}$$

The width of the depletion band in the valence band is almost the same as in the conduction band, since the shape of the allowed bands is close to spherical at these energies. The suppression band in the valence band gives a limit on the suppression frequency band because $m_n \ll m_p$. The red boundary (left dashed line in Fig. 6) is connected with a transition of an electron with momentum $k_{n-}$ (Fig. 6) from the conduction band into the valance band with transfer of part of its momentum $p_p$ to the photon. Subsequently, this electron changes its direction of motion until it moves in the opposite direction and inhibits amplification of the radiation through transitions of electrons with momentum of absolute magnitude $k_{n-}-2p_p$ from the conduction band into the valence band. The energy of the photons in these transitions is given by

$$h\nu_{p-} = E_g + \frac{(k_{n-}-p_p)^2}{2m_p} + \frac{(k_{n-}-2p_p)^2}{2m_n} = h\nu - \frac{2k_{n-}p_p}{m_n} + \frac{2p_p^2}{m_n} \approx h\nu - \frac{2k_{n0}p_p}{m_n} + \frac{2p_p^2}{m_n}\frac{m_p}{m_n+m_p}. \tag{5}$$

Electrons with momentum $k_{n+}$ are involved in forming the blue suppression boundary (the dashed line on the right of Fig. 6). This boundary corresponds to a photon energy

$$h\nu_{p+} = h\nu + \frac{2k_{n+}p_p}{m_n} + \frac{2p_p^2}{m_n} \approx h\nu + \frac{2k_{n0}p_0}{m_n} + \frac{2p_p^2}{m_n}\frac{m_p}{m_n+m_p}. \tag{6}$$

Equations (5) and (6) imply that $h\nu_{p+} - h\nu > h\nu - h\nu_{p-}$; i.e., the suppression range on the blue side of the mode is wider than on the red.

The depletion band in the conduction band yields a very narrow suppression band. On the red side of the laser mode, it is

$$h\nu_{n-} - h\nu \approx -\frac{2k_{n0}p_p}{m_p} + \frac{2p_p^2 m_n}{m_p^2}. \tag{7}$$

On the blue side it is

$$h\nu_{n+} - h\nu \simeq \frac{2k_{n0}p_p}{m_p} + \frac{2p_p^2 m_n}{m_p^2}. \quad (8)$$

From Eq. (3) we find

$$k_{n0} = \sqrt{(h\nu - E_g)2m_n\left(1 + \frac{m_n}{m_p}\right)^{-1}}. \quad (9)$$

For quantitative estimates we determine $h\nu - E_g$ from the condition for sufficient gain. We shall start with a power law dependence for the interband absorption coefficient as a function of the photon energy, which is typical of straight band semiconductors,

$$\alpha = A\sqrt{T}\sqrt{\frac{h\nu - E_g}{kT}}, \quad (10)$$

where $A$ is a coefficient that is $\sim 200\,\mathrm{cm}^{-1}\cdot\mathrm{K}^{-1/2}$ for III–V semiconductors, $T$ is the absolute temperature, and $k$ is the Boltzmann constant. We take a simplified form of the gain coefficient,

$$g_L = \alpha\frac{2(h\nu - E_g)}{kT}(2 + e^{F_i/kT})^{-1}, \quad (11)$$

where $F_i$ is the depth of the Fermi level in the conduction band at the lasing threshold. If we consider only the optical losses at the radiation exit, then

$$g_L = \frac{1}{L}\ln\frac{1}{R}, \quad (12)$$

where $L$ is the length of the laser cavity, and $R$ is the reflectivity of the mirrors. From Eqs. (9) and (10) we obtain

$$h\nu - E_g = kT\left(\frac{g_L(2 + e^{F_i/kT})}{A\cdot 2\sqrt{kT}}\right)^{2/3}. \quad (13)$$

For calculating $F_i$ we shall use the transcendental equation[15]

$$\frac{m_p}{m_n} = \left(\frac{4}{3\sqrt{\pi}}\right)^{2/3}\frac{F_i}{kT}\,e^{2F_i/3kT}. \quad (14)$$

We shall calculate the photon momentum $p_p$ using the formula[16]

$$p_p = \frac{E_g n}{c}, \quad (15)$$

where $n$ is the refractive index, and $c$ is the speed of light.

Let us use the following laser parameters for $T = 77\,\mathrm{K}$: $E_g = 0.35\,\mathrm{eV}$, $n = 3.6$, $m_n = 0.025\,m_e$, $m_p/m_n = 20$, $L = 0.035\,\mathrm{cm}$, $R = 0.3$, and $A = 187\,\mathrm{cm}^{-1}\cdot\mathrm{K}^{-1/2}$. This yields the following: $g_L = 34.4\,\mathrm{cm}^{-1}$, $h\nu - E_g = 0.377\,kT$, $F_i = 3kT$, $p_p = 0.67\times 10^{-22}\,\mathrm{g\cdot cm/s}$, $k_{n0} = 4.18\times 10^{-22}\,\mathrm{g\cdot cm/s}$, $\Delta E_n = 0.07\,\mathrm{meV}$, $h\nu_{p+} - h\nu = 1.77\,\mathrm{meV}$, and $h\nu - h\nu_{p-} = 1.26\,\mathrm{meV}$. At the same time, the intermode interval for these lasers is $\Delta h\nu_L = 0.5\,\mathrm{meV}$. Thus, the suppression of neighboring modes by the photon momentum extends over three intermode distances to the blue and over two intermode distances to the red from the laser mode.

The modes closest to the fundamental mode are most strongly suppressed, since the depletion band in the valence band is more involved in generating them than in generating the distant modes. The depletion band in the conduction band produces a suppression interval that is smaller than the intermode separation, and therefore it does not participate in the suppression of the neighboring modes. It, on the other hand, facilitates multimode lasing. In real lasers, the distribution of defects over the resonator length also affects the suppression of neighboring modes, as it promotes the selection of some mode.

## 7. CONCLUSIONS

A study of the emission spectra of InAsSb/InAsSbP lasers operating near 3.6 $\mu$m has shown that the number of lasing modes can be reduced without introducing crystallographic defects. Dominant lasing in two longitudinal modes separated by two intermode intervals has been obtained.

The effect of photon momentum on the suppression of spectral modes has been evaluated. It was found that the modes closest to the dominant mode are most strongly suppressed.

Laser spectroscopy has been carried out on the gases $N_2O$ and $CH_3Cl$ using the two modes of the diode laser studied here. The absorption lines of nitrous oxide were identified and used to calibrate the frequency scale of the laser spectrometer.

These studies demonstrate the prospects for constructing defect-free lasers for high-resolution spectroscopy in which transverse spatial modes and part of the spectral modes are suppressed.

This work was supported by a grant from the Czech Academy of Sciences (No. A4040708) and a grant from the European INCO-Copernicus consortium (No. IC15-CT97-0802(DG12-COPE)), as well as a grant from the Russian Fund for Fundamental Research (No. 99-02-18019).

We thank T. N. Danilova for a rich and useful discussion on the results of this work.

*)E-mail: yak@iroptl.ioffe.rssi.ru; Fax: (812)2470006

[1] J. C. Comparo, Contemp. Phys. **26**, 443 (1985).
[2] A. I. Nadezhdinskii, in *Proceedings Freiburg Symposium* (1991), R. Grisar, Schmidtke, M. Tacke, and G. Restelli (eds.), Kluwer, Dordrecht, (1992), p. 155.
[3] R. V. Martinelli, Laser Focus World **3**, 77 (1996).
[4] V. G. Avetisov, Yu. V. Kosichkin, V. I. Malakova, A. V. Merkulov, A. I. Nadezhdenskiĭ, S. L. Paleĭ *et al.*, Kvant. Elektron. (Moscow) **20**, 839 (1993).
[5] Z. Zelinger, S. Civis, P. Kubat, and P. Engst, Infrared Phys. Technol. **36**, 537 (1995).
[6] A. P. Danilova, T. N. Danilova, A. N. Imenkov, N. M. Kolchanova, M. V. Stepanov, V. V. Sherstnev, and Yu. P. Yakovlev, IEE Proc.: Optoelectron. **145**, 261 (1998).
[7] T. N. Danilova, A. P. Danilova, A. N. Imenkov, N. M. Kolchanova, M. V. Stepanov, V. V. Sherstnev, and Yu. P. Yakovlev, in *Proceedings of the Conference on Physics at the Threshold of the 21st Century*, St. Petersburg (1998).
[8] T. N. Danilova, A. P. Danilova, A. N. Imenkov, N. M. Kolchanova, M. V. Stepanov, V. V. Sherstnev, and Yu. P. Yakovlev, Fiz. Tekh. Poluprovodn. (1999) [in press].

[9] A. N. Baranov, T. N. Danilova, O. G. Ershov, A. N. Imenkov, V. V. Sherstnev, and Yu. P. Yakovlev, Pis'ma Zh. Tekh. Fiz. **18**, 6 (1992) [Sov. Tech. Phys. Lett. **18**, 8 (1992)].

[10] T. N. Danilova, A. P. Danilova, O. G. Ershov, A. N. Imenkov, M. V. Stepanov, and Yu. P. Yakovlev, Fiz. Tekh. Poluprovodn. **31**, 1392 (1997) [Semiconductors **31**, 1325 (1997)].

[11] A. Popov, V. Sherstnev, Yu. Yakovlev, S. Civis, and Z. Zelinger, Spectrochim. Acta A **54**, 821 (1998).

[12] A. A. Popov, V. V. Sherstnev, Yu. P. Yakovlev, S. Civis, and Z. Zelinger, Pis'ma Zh. Tekh. Fiz. **23**(21), 72 (1997) [Tech. Phys. Lett. **23**, 890 (1997)].

[13] A. G. Maki and J. S. Wells, *Wavenumber Calibration Table from Heterodyne Frequency Measurements*, NIST Special Publication 821 (Washington, 1991).

[14] P. G. Eliseev and A. P. Bogatov, Kvant. Elektron. (Moscow) **10**, 826 (1983).

[15] A. A. Andaspaeva, A. N. Baranov, B. L. Gel'mont, B. E. Dzhurtanov, G. G. Zegrya, A. N. Imenkov, Yu. P. Yakovlev, and S. G. Yastrebov, Fiz. Tekh. Poluprovodn. **25**, 394 (1991) [Sov. Phys. Semicond. **25**, 321 (1991)].

[16] V. L. Bonch-Bruevich and S. G. Kalashnikov, *Semiconductor Physics* [in Russian], Nauka, Moscow (1977), p. 592.

Translated by D. H. McNeill

# Nonpolarizing radiation detectors based on wide-gap semiconductor crystals

P. G. Kasherininov and A. N. Lodygin

*A. F. Ioffe Physicotechnical Institute, Russian Academy of Sciences, 194021 St. Petersburg, Russia*

S. S. Martynov and V. S. Khrunov

*Institute of Physicotechnical Problems, Dubna, Russia*

(Submitted March 15, 1999; accepted for publication June 11, 1999)
Fiz. Tekh. Poluprovodn. **33**, 1475–1478 (December 1999)

Wide gap, insulating semiconductor crystals offer great promise in photoelectric devices, especially as detectors of electromagnetic and nuclear radiation, but are not widely used because they become polarized during operation. During operation of detectors using these crystals with a high concentration of deep impurity levels, electrical charges build up and produce a change, over time, in the electric field within the crystal and in the magnitude of the detector photoresponse. Since it is impossible to avoid impurity centers in these crystals at this time, we propose new approaches to creating radiation detectors-dosimeters which do not become polarized over time, but rely on productive use of the polarization charges that accumulate in them. © *1999 American Institute of Physics.* [S1063-7826(99)01712-3]

## RADIATION DOSIMETRY

We propose constructing detectors in which the polarization charge is limited to a certain fixed value. When this value is reached, the polarization charge leaves the crystal and new charge begins to develop in its place, etc. The flow of polarization charge out of the crystal will be accompanied by short, periodic current (standard) pulses in the external circuit of the detector. The specified, fixed electric charge accumulates in the detector crystal between successive pulses when a strictly determined dose of radiation falls on the detector surface. This kind of detector can be used as a radiation dosimeter.[1,2]

The proposed dosimeter can be constructed using metal–gaseous dielectric–single-crystal wide-gap insulating semiconductor–metal structures, i.e., M(GD)IM structures. Depending on the electric field strength in the gas layer in these structures, the gas layer will be in one of two bistable states: low conductivity, when the field is low, or high conductivity (gas discharge due to collisional ionization and photoionization processes), when the electric field in the gas layer is high. The resistance of the gas layer differs by many orders of magnitude in these two states and the transition from one of the bistable states into the other takes place at a certain breakdown voltage that depends on many external parameters (the thickness of the gas layer, its pressure, temperature, etc.[3]). It has been shown that, when an external voltage ($V_{00}=1-2$ kV) is applied to this structure, the electric field strengths in the semiconducting crystal and gas layer turn out to be quite different because of differences in their dielectric permittivities. The field strength in the gas layer is much higher than in the crystal and is close to the breakdown value.[2]

When there is no radiation, this field distribution in the structure remains unchanged for a long time. When the structure is illuminated by light that is photoactively absorbed in the crystal material, the electric field distribution between the layers of the structure changes significantly. The free photocarriers created in the crystal by the light will be drawn to the corresponding electrodes by the electric field in the crystal and create a dc or pulsed (with pulsed illumination of the structure) photocurrent in the external circuit of the structure. Since the gaseous dielectric is impermeable to the photocarriers, an electrical charge begins to accumulate at the boundary with the gas layer. Because of the charge buildup, the electric field strength in the crystal begins to decrease with time and that in the gas layer increases.[2] The photocurrent pulses in the external circuit of the detector begin to decrease in amplitude with time when the structure is subjected to constant pulsed illumination. When a certain, fixed amount of charge at the boundary with the gas layer is reached, the electric field in the gas layer attains the breakdown level. Breakdown of the gas layer is accompanied by an avalanche of ionized carriers: electrons and positively charged ions.[3] The charge on these carriers reduces the polarization charge at the boundary of the gas capacitor to a level such that the electric field in the gas-filled gap falls below the critical value. The gas discharge stops and the gas layer returns to the low-conductivity state. A short current pulse flows in the external circuit during the time of the gas discharge. After the gas discharge ends, the field strength in the crystal increases in accordance with the magnitude of the residual polarization charge at the boundary with the gas layer. When the structure is subjected to constant illumination, gas breakdown will be cyclical. Here the photoresponse pulses in the circuit of the structure are not directly related to the gas breakdown. It has been shown[1,4] that in structures of this type with a stable solid dielectric (mica), when the structure is illuminated by light that is photoactively absorbed in the crystal, the photocurrent flowing in the external circuit of the structure decreases with time to zero as the polarization charge develops at the boundary with the mica because the

 

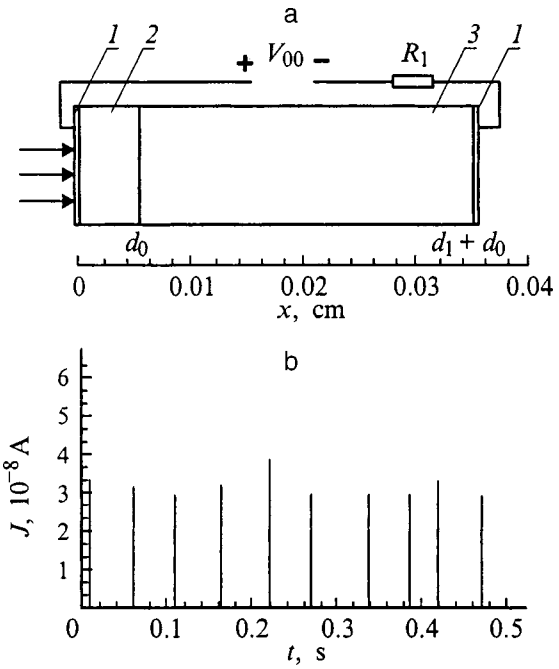


FIG. 1. Photoresponse of a metal–gas discharge–insulator–metal diamond dosimeter exposed to a steady ultraviolet light. a — Schematic diagram of the experiment: *1* — optical transparent electrodes, *2* — gaseous dielectric layer of thickness $d_0 = 6 \times 10^{-5}$ m, *3* — insulating crystal of natural diamond of thickness $d_1 = 3 \times 10^{-4}$ m, and $R_1$ — load resistance. b — Pulses of current from the gas discharge ($J$) in the external circuit of the dosimeter under steady illumination; $V_{00} = 1300$ V.

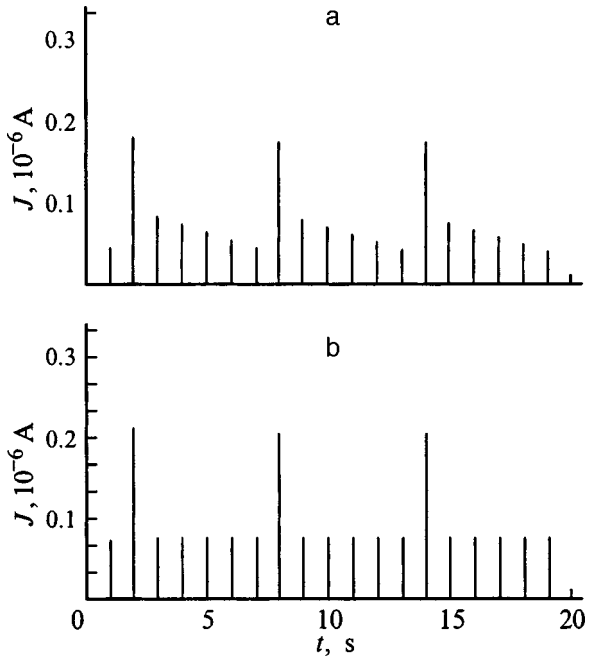


FIG. 2. Photoresponse of a metal–gas discharge–insulator–metal diamond dosimeter exposed to a pulsed ultraviolet light: current pulses ($J$) in the external circuit of the detector. The wavelength is $\lambda = 0.337 \times 10^{-6}$ m, the area of the illuminated detector surface is $S = 10^{-6}$ m$^2$, the energy of the laser light incident on the surface of the structure during a single pulse (without attenuating filters) is $2.2 \times 10^{-6}$ J, the pulse duration is $10^{-8}$ s, and the frequency is 10 Hz. Voltage $V_{00}$ (V): a — 1000, b — 1200.

electric field in the crystal goes to zero. Using a bistable gaseous insulator in the structure makes it possible to return the structure periodically to the initial electric field distribution between its layers when it is subjected to constant irradiation and, thereby, to employ these structures in a radiation detector-dosimeter that does not become polarized with time.

When the structure is subjected to steady irradiation, periodic current pulses flow in the external circuit which measure the energy (dose) of the incident radiation. The dose of radiation incident on the detector surface over the time between two successive current (standard) pulses from the gas discharge is determined by the voltage applied to the structure and does not depend on the intensity of the radiation or the size of the irradiated detector surface. The radiation dose over a fixed interval of time is determined by the number of current pulses within that time interval.[1,2] Figure 1 shows the photoresponse of this kind of dosimeter under steady illumination. A sequence of pulses in the gas discharge current ($J$) in the external circuit can be seen over time ($t$). The energy of the radiation incident on the surface of the structure over the time between two successive current pulses is $2.2 \times 10^{-6}$ J for this voltage. This type of dosimeter is original and is suitable for operational monitoring of the energy of electromagnetic[1] and nuclear[2] radiation.

## DETECTOR-DOSIMETER FOR PULSED RADIATION

When the structure is irradiated by a periodic radiation pulse, two types of current pulses flow in its external circuit: high, infrequent pulses and lower-amplitude pulses at the repetition rate of the radiation pulses (Fig. 2).

The first type of current pulse is caused by the gas discharge and determines the energy (dose) of the incident pulsed radiation between two successive discharge pulses. The other type of current pulse is caused by the photoresponse to the pulses of detected light and measures their shape and intensity (Fig. 2).

Each pulse of the detected radiation creates a certain polarization charge in the crystal at the boundary of the gas layer, which lowers the electric field strength in the crystal. As a result, the response in the external circuit of the detector from each of a succession of light pulses will generally be lower than the previous one, until the total polarization charge in the crystal reaches the critical value which causes breakdown of the gas layer. After a regular gas breakdown, the electric field distribution in the structure returns to the original dark value for the previous cycle. Thus, the train of photoresponse pulses produced by periodic light pulses of equal amplitude will, in general, decrease from one discharge current pulse to the next (Fig. 2a). In nonpolarizing detectors, the amplitudes of the photoresponse pulses produced by all the light pulses should be identical. Detectors of this sort based on metal–gas discharge–insulator–metal structures can be made in several ways.

One way of creating a nonpolarizing detector based on metal–gas discharge–insulator–metal structures on small-area crystals is to increase the applied voltage (Fig. 2). As shown in Ref. 2, during the time between two successive gas discharge pulses, the critical polarization charge at the

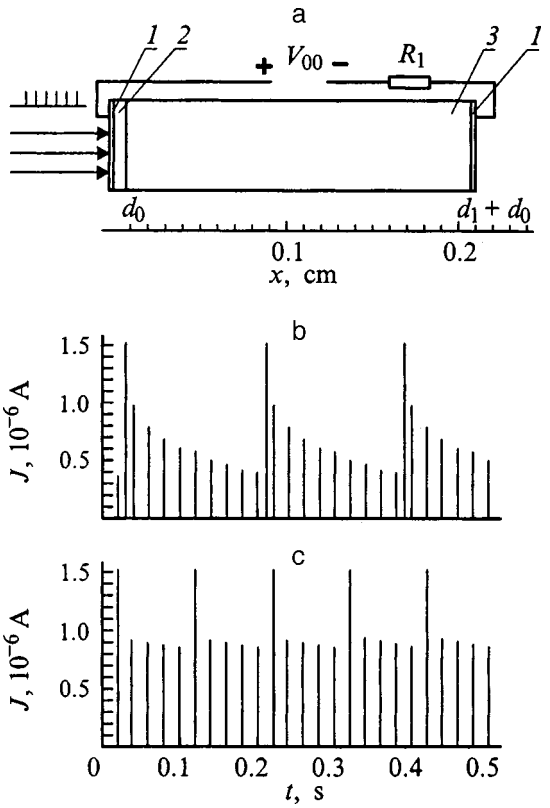


FIG. 3. Photoresponse of a metal–gas discharge–insulator–metal diamond dosimeter on an insulating crystal of bismuth silicate subjected to pulsed ultraviolet irradiation on parts of its surface (wavelength $\lambda = 0.54 \times 10^{-6}$ m, pulse repetition rate 50 Hz, $V_{00} = 1500$ V). a — Schematic diagram of the experiment: *1* — optically transparent electrodes, *2* — gaseous dielectric layer of thickness $d_0 = 60 \times 10^{-6}$ m, *3* — bismuth silicate ($Bi_{12}SiO_{20}$) crystal with a thickness of $d_1 = 2 \times 10^{-3}$ m. $R_1$ is the load resistance. b, c — are the photoresponses of the metal–gas discharge–insulator–metal structure when areas $S = 3 \times 10^{-7}$ cm$^2$ (b) and $S = 1.25 \times 10^{-5}$ cm$^2$ (c) of the gas layer are irradiated. The high, infrequent pulses are the gas discharge current ($J$) pulses and the lower amplitude pulses with a repetition rate of 50 Hz are the photoresponse pulses ($J$) from the light pulses.

boundary of the gas layer decreases (and there are changes in the electric field in the crystal and in the magnitude of the photoresponse of the structure). Figure 2b shows that when a voltage $V_{00} = 1200$ V is applied, the detector does not polarize, so that it becomes possible to make simultaneous measurements of the shape and intensity of the radiation pulses, as well as of the energy per pulse of the radiation from the number of response pulses between two successive gas discharge pulses (for a known energy of the radiation incident on the surface of the structure during the time between these discharge pulses).

Another way of making a nonpolarizing detector is to increase the illuminated detector area. It has been found experimentally that breakdown of the gas layer of the structure takes place over an area of its surface $S_0 < 10^{-6}$ m$^2$, regardless of the surface area that is illuminated. Each successive breakdown takes place at a new portion of the area of this layer. The change in the electric field strength in the crystal during detection of the radiation occurs only in this breakdown segment of the surface of the structure ($S_0$). The change in the electric field strength in this segment causes the observed change in the amplitude of the chain of successive photoresponse pulses when the structure is illuminated by light pulses of equal amplitude. If the illuminated area of the detector surface is substantially (by an order of magnitude) greater than the area $S_0$, then the contribution to the photoresponse of the structure from this segment of the illuminated surface ($S_0$) will be negligible and the train of photoresponse pulses between two successive gas discharge pulses will have the same amplitude. We see in Fig. 3 that as the area of the illuminated surface is increased, the amplitude of the photoresponse pulses becomes approximately the same in magnitude. The detector is essentially unpolarized when the illuminated area of its surface is $S > 1.5 \times 10^{-5}$ m$^2$. This type of device can be made from crystals with low values of the parameter $\mu\tau$, such that $\mu\tau < 10^{-6}$ cm$^2 \cdot$ V$^{-1}$, where $\mu$ is the carrier mobility, and $\tau$ is their lifetime. The high sensitivity of devices using these crystals to the detected radiation is determined by the high electric field strength in the crystal, $10^5 - 10^6$ V/m (Ref. 2).

We have therefore demonstrated the possibility of creating a new type of device based on wide-gap insulating crystals: nonpolarizing radiation detector-dosimeters which permit simultaneous measurement of the shape and intensity of pulsed radiation and of the energy per pulse of the radiation.

This work was supported by the International Scientific-Technical Center (Project 447).

[1] P. G. Kasherininov and A. N. Lodygin, Pis'ma Zh. Tekh. Fiz. **23** (4), 23 (1997) [Tech. Phys. Lett. **23**, 91 (1997)].
[2] P. G. Kasherininov and A. N. Lodygin, Pis'ma Zh. Tekh. Fiz. **24** (22), 64 (1998) [Tech. Phys. Lett. **24**, 110 (1998)].
[3] N. P. Bogoroditskiĭ and V. V. Pasynkov, *Electronic Materials* [in Russian], Gosenergoizdat, Moscow (1961).
[4] I. A. Zelenin, P. G. Kasherininov, and V. E. Khartsiev, Pis'ma Zh. Tekh. Fiz. **22** (5), 86 (1996) [Tech. Phys. Lett. **22**, 132 (1996)].

Translated by D. H. McNeill